Characterization of the phosphomimetic mutant Y39E of α-Synuclein

Dissertation

for the award of the degree

"Doctor rerum naturalium" (Dr.rer.nat.)

of the Georg-August-Universität Göttingen

within the doctoral program of Biology

of the Georg-August University School of Science (GAUSS)

participating in the International PhD Program in

Molecular Biosciences and Biomedicine

of the Universidad Nacional de Rosario in Argentina

and the Georg-August-Universität Göttingen

submitted by

Nicola Martina Böffinger

from Bad Nauheim, Germany

Göttingen, 2024

Thesis Committee

Christian Griesinger
Department of NMR-based Structural Biology, Max Planck Institute for Multidisciplinary Sciences, Göttingen (Germany)

Claudio Fernández
Max-Planck Laboratory for Structural Biology, Chemistry and Molecular Biophysics of Rosario (MPLbioR), Centro de Estudios Interdisciplinarios (CEI), Universidad Nacional de Rosario (UNR), Rosario (Argentina)

Nils Brose
Department of Molecular Neurobiology, Max Planck Institute for Multidisciplinary Sciences, Göttingen (Germany)

Members of the Examination Board

Reviewer: Kai Tittmann
Department of Molecular Enzymology, Georg-August University, Göttingen (Germany)
Second Reviewer: Claudio Fernández
Max-Planck Laboratory for Structural Biology, Chemistry and Molecular Biophysics of Rosario (MPLbioR), Centro de Estudios Interdisciplinarios (CEI), Universidad Nacional de Rosario (UNR), Rosario (Argentina)

Further members of the Examination Board:

Christian Griesinger
Department of NMR-based Structural Biology, Max Planck Institute for Multidisciplinary Sciences, Göttingen (Germany)

Nils Brose
Department of Molecular Neurobiology, Max Planck Institute for Multidisciplinary Sciences, Göttingen (Germany)

Eduardo Ceccarelli
Research group: Protein structure, folding and function, Instituto de Biología Molecular y Celular de Rosario (IBR), Rosario (Argentina)

Nicolás Rey
Department of Chemistry, Pontifical Catholic University of Rio de Janeiro, Rio de Janeiro (Brasil)

Date of the oral examination: 10.04.2024

Affidavit

I hereby declare that the doctoral thesis entitled “Characterization of the phosphomimetic mutant Y39E of α-Synuclein” has been written independently, with no other sources and aids than quoted.

……..

Nicola Martina Böffinger

Göttingen, February 2024

Table of Content

List of Figures

List of Tables

List of Abbreviations

Table 1: List of abbreviations

Abbreviation	Expression
6OHDA	6-hydroxydopamine
AD	Alzheimer's disease
ADEs	Anterior deirid neurons
AFM	Atomic force microscopy
AMP	Ampicillin
APS	Ammonium persulfate
aSyn	α-Synuclein
Aβ	Amyloid beta
BSA	Bovine serum albumin
C. elegans	*Caenorhabditis elegans*
CAM	Complementary and alternative medicine
CD	Circular dichroism
CEPs	Cephalic sensilla neurons
CES	Capillary Electrophoresis Sequencing
CHL	Chloramphenicol
CNS	Central nervous system
cryoEM	Cryo-electron microscopy
DBS	Deep brain stimulation
DLS	Dynamic light scattering
DMEM	Dulbecco's Modified Eagle Medium
DMPS	1,2-dimyristoyl-sn-glycero-3-phospho-L-serine
DMSO	Dimethyl sulfoxide
dNTP	Deoxynucleotide triphosphate
DOPC	1,2-di-(9Z-octadecenoyl)-sn-glycero-3-phosphocholine
DOPE	1,2-di-(9Z-octadecenoyl)-sn-glycero-3-phosphoethanolamine
DOPS	1,2-di-(9Z-octadecenoyl)-sn-glycero-3-phospho-L-serine
DOSY	Diffusion-ordered spectroscopy
DTT	Dithiothreitol
E. coli	*Escherichia coli*

Abbreviation	Expression
EDTA	Ethylenediaminetetraacetic acid
FBS	Fetal bovine serum
GFP	Green fluorescent protein
HPLC	High pressure liquid chromatography
HSQC	Heteronuclear single quantum coherence
IDP	Intrinsically disordered proteins
INEPT	Insensitive nuclei enhanced polarization transfer
IPM	Inner presynaptic membrane
IPTG	Isopropyl-1-thio-β-D-galactopyranoside
L:P	Lipid:protein ratio
LBa	Luria-Bertani agar
LBD	Lewy body disease
LBm	Luria-Bertani medium
LBs	Lewy bodies
L-DOPA	Levodopa
LRRK2	Leucin-rich repeat kinase 2
M	mol/l
MAO-B	Monoamine oxidase B
MTSL	1-Acetoxy-2,2,5,5-tetramethyl-δ-3-pyrroline-3-methyl
MTT	Thiazolyl Blue Tetrazolium Bromide
NAC	Non-amyloid-β component
ND	Neurodegenerative diseases
NGM	Nematode Growth Medium
NMR	Nuclear Magnet Resonance
OPM	Outer presynaptic membrane
PBS	Phosphate buffered saline
PCR	Polymerase-chain reaction
PcTS	Phthalocyanine tetrasulfonate
PD	Parkinson’s disease
PDEs	Posterior deirid neurons
PFFs	Preformed fibril seeds
PMSF	Phenylmethylsulfonyl fluoride
ppm	Parts per million
PRE	Paramagnetic relaxation enhancement

Abbreviation	Expression
PTMs	Post-translational modifications
R_H	Hydrodynamic radius
RIPA	Radioimmunoprecipitation assay
rpm	Rounds per minute
SDS-PAGE	Sodium dodecyl-sulfate polyacrylamide gel electrophoresis
SEC	Size exclusion chromatography
SNAP-25	Synaptosomal-associated protein 25
SNARE	Soluble N-ethylmaleimide sensitive factor activating protein receptor
SUMOylation	Addition of small ubiquitin-like modifiers
SUV	Small unilamellar vesicle
SV	Synaptic vesicle
TCM	Traditional Chinese medicine
TDP-43	TAR DNA binding protein
TEMED	Tetramethylethylenediamine
ThT	Thioflavin-T
VAMPs	Vesicle-associated membrane proteins
WT	Wild-type
YFP	Yellow fluorescent protein

Abstract

α-Synuclein (aSyn) has long been identified as a key factor in the pathogenesis of Parkinson's Disease (PD), with familial mutations in the SNCA gene contributing to the aberrant aggregation of aSyn. Its aggregation results in the formation of Lewy Bodies, a characteristic hallmark of PD, ultimately leading to neurodegeneration and cell loss. While mutations have been extensively studied, post-translational modifications (PTMs), particularly phosphorylation, have emerged as crucial players in aSyn's physiological function and pathological aggregation. The kinase c-abl is known to phosphorylate aSyn predominantly at Tyrosine 39 (Y39), a modification often observed in advanced PD stages associated with elevated c-abl levels. Given the challenges in purifying phosphorylated proteins, phosphomimetic mutants, in this case Y39E, serves to simulate phosphorylation effects.

This study extensively characterizes the Y39E aSyn mutant across various aspects, including monomeric structure and dynamics, membrane binding*, in vitro* and *in vivo* aggregation properties, dopaminergic neurodegeneration, and toxicity. Employing a multidisciplinary approach, biophysical methods such as nuclear magnet resonance (NMR), circular dichroism (CD) spectroscopy, Thioflavin-T (ThT) fluorescence measurements, and size exclusion chromatography (SEC) were combined with biological methods including molecular cloning, protein expression, and *in vivo* investigations using cell-based assays and the animal model *C. elegans*.

Structural analysis revealed that the Y39E monomer closely resembled the wild-type (WT) monomeric structure, with no significant differences in backbone dynamics nor in the hydrodynamic radius. However, slightly higher R_2 relaxation rates and minor changes in transient long-range interactions were observed in the Y39E variant. The overall membrane affinity remained equal between WT and Y39E, although the NAC region of Y39E exhibited reduced interaction. Notably, during the aggregation process, Y39E incorporated fewer monomers and displayed a prolonged lag phase with concentration-dependent kinetics. In cellular and animal models, the Y39E mutant demonstrated fewer cellular inclusions and smaller aggregates, respectively. Compared to the WT species, dopaminergic neurodegeneration was significantly elevated when expressing Y39E aSyn in *C. elegans*, impacting the nematode's behavior, while mitochondrial pathways were ruled out as a cause of toxicity.

Additionally, data acquired on pY39 aSyn by other research groups aligned closely with results obtained in this study, indicating the Y39E mutant as a valuable tool for probing phosphorylation at this specific site, and confirming that pY39 can be mimicked by the Y39E mutant. Furthermore, the significance of pY39 is underscored by evidence of various research groups, showing that inhibiting phosphorylation effectively hinders disease progression and diminishes pathology in animal models.

In summary, this work characterizes de Y39E mutant of aSyn. The structure and dynamics of the Y39E aSyn monomer closely resembled those of the WT species. However, differences were observed in the aggregation profiles between WT and Y39E aSyn, and dopaminergic neurodegeneration was found to be elevated for the Y39E mutant. Furthermore, this work highlights the crucial role of PTMs in aSyn pathology, showing that mutations, such as Y39E emerge as valuable instruments for mimicking PTMs, thereby simplifying the research process.

Zusammenfassung

α-Synuclein (aSyn) wurde schon lange als Schlüsselfaktor in der Pathogenese von Parkinson-Krankheit (PD) identifiziert. Es ist bekannt, dass familiäre Mutationen im SNCA-Gen zur pathologischen Aggregation von aSyn beitragen. Diese Aggregation führt zur Bildung von Lewy-Körpern, einem charakteristischen Merkmal von PD, welches wesentlich zu Neurodegeneration und Zellverlust beiträgt. Während Mutationen seit langem umfassend untersucht wurden, haben sich posttranslationale Modifikationen (PTMs), insbesondere Phosphorylierung, erst in jüngerer Zeit als entscheidende Akteure in der physiologischen Funktion und pathologischen Aggregation von aSyn erwiesen. Die Kinase c-abl phosphoryliert aSyn vorwiegend an Tyrosin 39 (Y39), eine Modifikation, die häufig in fortgeschrittenen PD-Stadien mit erhöhten c-abl-Levels beobachtet wird. Aufgrund der Herausforderungen bei der Herstellung phosphorylierter Proteine dienen phosphomimetische Mutanten, in diesem Fall Y39E, dazu, Phosphorylationseffekte zu simulieren.

Diese Arbeit charakterisiert die Y39E aSyn Mutante hinsichtlich verschiedener Aspekte, einschließlich der Struktur und Dynamik des Monomers, Membranbindung, der Aggregation *in vitro* und *in vivo*, dopaminerge Neurodegeneration und Toxizität. In einem multidisziplinären Ansatz wurden biophysikalische Methoden wie Kernmagnetresonanz (NMR), zirkuläre Dichroismus (CD) Spektroskopie, Thioflavin-T (ThT) Fluoreszenzmessungen und Größenausschlusschromatographie (SEC) mit biologischen Methoden wie molekularer Klonierung, Proteinexpression und Aufreinigung, zellbasierten Assays und *in vivo* Experimenten in *C. elegans* kombiniert.

Es konnte festgestellt werden, dass die Struktur des Y39E Monomers der des Wildtyp (WT) stark ähnelt. Es wurden keine signifikanten Unterschiede in der Dynamik des Peptidrückgrats oder des hydrodynamischen Radius gefunden. Allerdings wurden erhöhte R_2 Relaxationsraten und geringfügige Änderungen in kurzweiligen, langreichweitigen Interaktionen beobachtet. Die allgemeine Affinität zur Membran blieb zwischen WT und Y39E gleich, allerdings zeigte die NAC-Region von Y39E eine verringerte Wechselwirkung mit der Membran. Während des Aggregationsprozesses inkorporierte Y39E aSyn weniger Monomere und zeigte eine verlängerte lag-Phase, mit konzentrationsabhängigen kinetischen Parametern. In

zell-basierten und tierischen Modellen führte eine Expression von Y39E zu weniger zellulären Einschlüssen und kleineren Aggregaten. Die dopaminerge Neurodegeneration war signifikant erhöht, wenn Y39E aSyn in *C. elegans* exprimiert wurde, was sich im Verhalten der Nematoden spiegelte. Mitochondriale Signalwege konnten als Ursache der erhöhten Toxizität ausgeschlossen werden.

Zusätzlich wurde gezeigt, dass Daten, die von anderen Forschungsgruppen zu pY39 aSyn erhoben wurden, eng mit den in dieser Studie erhaltenen Ergebnissen übereinstimmen, was die Y39E Mutante als wertvolles Instrument zur Untersuchung der Phosphorylierung an dieser spezifischen Stelle bestätigt und zeigt, dass pY39 durch die Y39E Mutante imitiert werden kann. Darüber hinaus wird die Bedeutung von pY39 durch Resultate verschiedener Forschungsgruppen unterstrichen, die zeigen, dass die Hemmung der Phosphorylierung den Krankheitsfortschritt effektiv behindert und die Pathologie in Tiermodellen verringert.

Zusammenfassend charakterisiert diese Arbeit die Y39E Mutante von aSyn. Es konnte gezeigt werden, dass sich Struktur und Dynamik des Y39E aSyn Monomers und des WT Monomers stark ähneln. Unterschiede wurden im Aggregationsverhalten zwischen WT und Y39E aSyn beobachtet. Die Expression von Y39E aSyn führte außerdem zu erhöhter dopaminerger Neurodegeneration. Darüber hinaus hebt diese Studie die entscheidende Rolle von PTMs in der aSyn-Pathologie hervor, indem sie zeigt, dass Mutationen wie Y39E wertvolle Instrumente zur Nachahmung von PTMs darstellen und damit den Forschungsprozess vereinfachen und beschleunigen können.

1 Introduction

1.1 Neurodegenerative Disorders

Neurodegenerative diseases (ND) manifest through progressive neuronal dysfunction, eventually leading to neurological cell loss[1,2]. Common ND, including Alzheimer's disease (AD), Parkinson's disease (PD), prion disease, and Huntington's disease, share this feature[1]. Notably, patients diagnosed with multiple ND have been documented, underscoring the intricate challenges associated with their treatment[3,4]. The complexity of treating ND arises from their development in the human brain, rising challenges such as the blood-brain barrier and intricate surgeries in the head region[5].

One of the key characteristics of most ND is the involvement of intrinsically disordered proteins (IDP) and their mal-functioning, altering their physiological properties and often preceding clinical manifestations[6–8]. IDP can be entirely unstructured or contain intrinsically disordered regions[9]. They are usually composed of many charged and polar amino acids, while their lack of hydrophobicity hinders the cooperative folding of proteins[9]. IDP are involved in many cellular processes, including cell cycle control, cell signaling, and the regulation of transcription and translation of various cellular proteins[10–12].

Under physiological conditions, IDP exist in a dynamic equilibrium of multiple conformational states, ranging from complete disorder to varying degrees of folding[13,14]. Changes in the cellular environment or mutations within these proteins can lead to misfolding and aggregation, which ultimately affects their physiological functions[15,16]. Misfolded IDP can self-propagate, induce cellular stress and damage, and exhibit prion-like spreading to neighboring cells[17–19].

Noteworthy examples of IDP linked to prevalent neurodegenerative conditions include amyloid beta (Aβ) and tau in AD, α-Synuclein (αSyn) in PD, and TAR DNA binding protein (TDP-43) in amyotrophic lateral sclerosis[20]. Within affected brains, these proteins undergo a misfolding process, transitioning from native conformations

to β-sheet-rich structures, ranging from small oligomers to extensive fibrillar aggregates[21]. Aβ, a peptide spanning 39-43 amino acids, forms neocortical plaques, a pathological hallmark of AD[22]. The microtubule-associated protein tau, prevalent not only in AD but in various tauopathies, constitutes the main component of neurofibrillary tangles[23,24]. Furthermore, 90% of amyotrophic lateral sclerosis cases are associated with the IDP TDP-43[25]. Therapeutic strategies aimed at modifying ND include interventions targeting the reduction of synthesis, prevention of aggregation, and enhancement of pathological IDP clearance[26].

1.1.1 Parkinson's Disease

The pathological attributes of the IDP aSyn lead to the development of synucleinopathies. One class of syncleinopathies is termed Lewy body disease, characterized by the detection of pathological aggregates of aSyn in Lewy bodies (LBs)[27]. Various manifestations of Lewy body disease, categorized by distinct symptoms and medical features, such as the presence of dementia, have been classified. They include dementia with LBs, PD dementia and PD[28].

PD is the second most prevalent neurodegenerative disorder after Alzheimer's disease, affecting 0.2% of the global population, which equates to over 10 million cases worldwide. Its prevalence rises with age, affecting 1% of individuals over 60 and up to 4% of those aged 80 and older. The incidence of PD increases exponentially, especially among men, who are 1.5 times more prone to develop PD[29–31]. Projections indicate that the global number of PD cases might range between 12 and 17 million by 2040[32]. By 2050, the number of cases is expected to double to a total of 20 million, partly due to an aging society[33]. Beyond its high prevalence, PD exerts a substantial economic impact. In the U.S., where nearly one million people live with PD and 90 000 new cases are diagnosed annually, the estimated total costs, encompassing direct and indirect expenses for treatment, social security payments, and lost income, approach nearly 52 billion dollars annually[34].

Clinically, PD is characterized by the degeneration of dopaminergic neurons in the substantia nigra pars compacta (depicted as dark regions in Figure 1) and the

presence of LBs (Figure 2)[35,36]. LBs consist predominantly of fibrillar aggregates of aSyn; however, they also incorporate organelles and membranes[37–40].

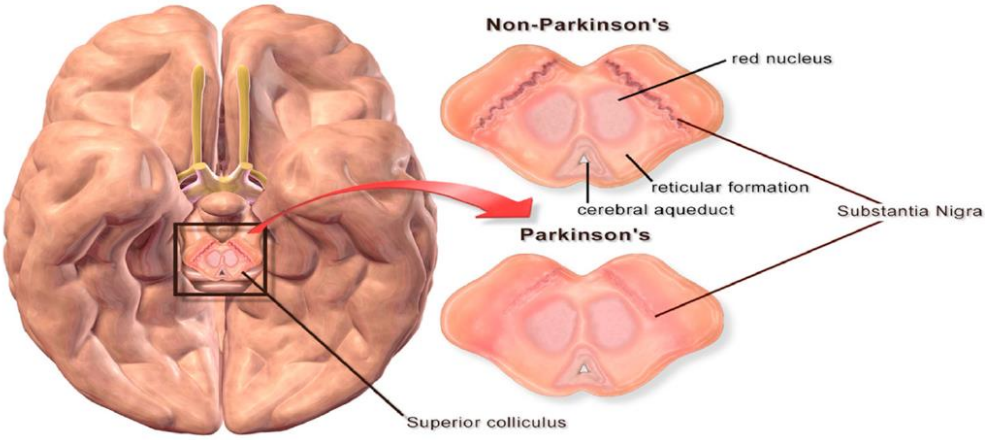

Figure 1: Substantia nigra pars compacta. Location of the substantia nigra in the brain (left) and comparison of the substantia nigra in healthy (top right) and PD patients (bottom right). Adopted from Gottapu *et al.* (2018)[41].

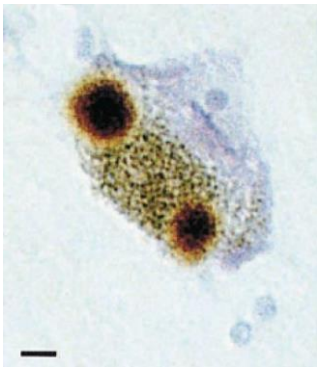

Figure 2: Lewy body. Substantia nigra pars compacta from PD patients (from the Cambridge Brain Bank), immunostained for aSyn. A cell with two aSyn positive LBs is displayed. Scale bar: 8 µm. Adopted from Spillantini *et al.* (1997)[39].

1.1.1.1 Symptoms

The degeneration of dopaminergic neurons in PD manifests in a spectrum of characteristic motor symptoms, including resting tremor, rigidity, bradykinesia, facial stiffness, shuffling gait, difficulty walking, inability to initiate voluntary movements, and postural instability[42,43]. These motor symptoms contribute to a distinct posture characterized by flexed legs and arms, along with a forward tilt of the upper body (Figure 3)[44].

Additionally, PD is marked by a constellation of non-motor symptoms, often inducing a passive and withdrawn demeanor in affected individuals. These neuropsychiatric symptoms include furthermore disturbed sleep, cognitive impairment, mood disorders, sensory disturbances, autonomic dysfunction, pain, and gastrointestinal problems[42,43].

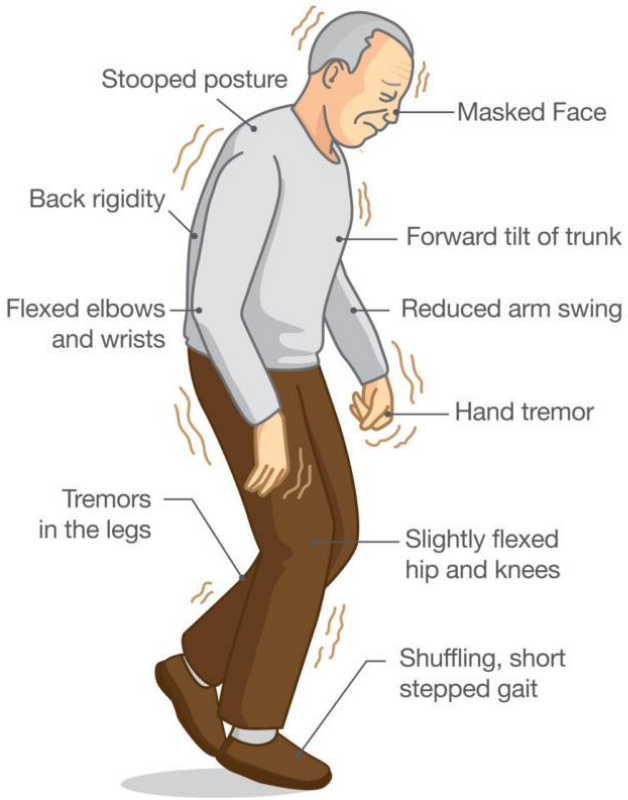

Figure 3: Symptoms of PD. Illustration of the typical PD posture, adopted from Signature Health Services (2022)[44].

The onset of PD symptoms typically occurs in the late 50s, with the age gradually increasing, approaching 60, due to the rising average age of the population[45]. Frequently, the initial symptoms manifest as non-motor symptoms associated with the gastrointestinal tract. Patients commonly seek medical attention due to issues such as constipation. These first symptoms originate from neurological defects of cells that regulate the movements of smooth gut muscles, leading to increased stiffness of these muscles, which are necessary for digestion and highly susceptible to rigidity[46]. Notably, during this initial phase, only non-motor symptoms such as sleep disturbances and loss of the sense of smell are evident, and there is yet no substantial loss of dopaminergic neurons in the substantia nigra[47,48]. The absence of typical motor symptoms in the early stages of the disease presents a challenge for

diagnosis, with a preclinical phase that can last up to 15 years before patients seek medical advice[49].

As neurodegeneration progresses and LBs begin to appear in the substantia nigra and subsequently spread to the midbrain, forebrain, and neocortex, more severe motor symptoms become evident in PD patients[50,51]. The characteristic resting tremor in the extremities arises from the neurodegeneration of dopaminergic neurons in the substantia nigra, disrupting signaling pathways and impairing the execution of voluntary movements, leading to involuntary movements while at rest[52]. Interestingly, this most typical symptom often surfaces long after the disease onset, with reports indicating that 30-40% of cases do not exhibit tremors at all, potentially contributing to a significant number of undiagnosed PD cases[49,53]. In the advanced stages of PD, a substantial loss of neuronal cells often leads to the onset of dementia, affecting up to 80% of PD patients. Compared to age-matched individuals without PD, those with PD face a 6-8 times higher risk of developing dementia[54]. Interestingly, 15% of all dementia cases are attributed to PD[55].

1.1.1.2 Risk Factors

In addition to aging, various factors have been identified as potential contributors to the development of PD. Exposure to agricultural substances, including pesticides, herbicides, insecticides, fertilizers, and solvents, has been linked to an elevated risk of PD[56,57]. Furthermore, air pollution has emerged as another factor associated with an increased risk of PD[58]. Conversely, specific lifestyle choices appear to correlate with a reduced risk of PD, such as regular consumption of caffeine or alcohol, adequate hydration, and residence in rural areas[59,60]. Interestingly, smokers, who often face higher risks of other diseases such as cancer, have a 40% lower risk of developing PD[61,62].

Genetic factors also play a role in the development of PD. Approximately 85% of PD cases are sporadic, lacking an identifiable genetic cause, while the remaining 15% are linked to familial mutations, indicating a genetic predisposition to the disease[63]. To date, researchers have identified 23 chromosomal regions associated with hereditary forms of PD. These regions are sequentially numbered based on the time point of their discovery and are denoted as PARK, indicating their link to PD[64]. The

first identified region was PARK1, located within the SNCA gene, responsible for encoding α-synuclein[65]. Mutations in PARK1 follow an autosomal-dominant pattern. Other autosomal-dominant mutations have been found in the regions PARK4 (SNCA) and PARK8 (Leucin-rich repeat kinase 2 (LRRK2))[64]. Mutations in the LRRK2 gene account for 4% of PD cases[66]. Autosomal-recessive forms of the disease result from mutations in genes such as PARK2 (PRKN), PARK6 (PINK1), PARK7 (DJ-1), and PARK9 (ATP13A2)[67–70].

1.1.1.3 Treatment

As of now, PD lacks a cure or a treatment capable of halting its progression. Both standard and alternative therapeutic approaches are focused on alleviating symptoms and slowing disease progression.

PD is characterized by a deficiency of dopamine, making dopamine replacement the standard pharmacological therapy[71–73]. Dopamine, a neurotransmitter also known as 3,4-dihydroxyphenethylamine, belongs to the molecular family of catechol- and phenethylamine[74,75]. Since dopamine cannot cross the blood-brain barrier, the precursor levodopa (L-DOPA) is administered to patients. L-DOPA can penetrate the blood-brain barrier and subsequently converts into dopamine, replenishing depleted dopamine levels and thus reducing patients' symptoms[76]. Typically administered orally on a daily basis, L-DOPA and dopamine agonists, which mimic dopamine by binding to receptors in the central nervous system (CNS), are often prescribed in conjunction at the beginning of the therapeutic intervention[72,73,77]. Inhibitors of the dopamine degradation pathway, such as monoamine oxidase B (MAO-B), are also employed to stabilize dopamine levels in the CNS[78].

Key molecules involved in autophagy, such as the ubiquitin-like modifier-activating enzyme ATG7 and the serine-threonine-protein kinase mTOR, have been observed to be dysregulated in PD patients. Consequently, autophagy-modifying drugs are utilized in PD treatment[79]. Furthermore, mediated by aSyn, increased neuroinflammation has been detected, resulting in decreased microglial or astroglial activation. To prevent this neuroinflammation from exacerbating the disease progression and symptoms, non-steroidal anti-inflammatory drugs are prescribed[80]. In approximately 50% of all PD cases, depression and anxiety occur as non-motor

symptoms, often in the early stages of the disease. Standard depression and anxiety medications are administered to address these symptoms[81].

Another pharmaceutical intervention is the administration of Vitamin D3, as patients with PD often exhibit a deficiency in this vitamin, which is associated with impaired motor functions and increased disease severity[82]. Vitamin D3 therapy has demonstrated cognitive performance enhancement and potential improvement in verbal fluency and memory[83].

The most common non-pharmaceutical therapy is deep brain stimulation (DBS)[84]. This involves the implantation of electrodes into affected brain regions. These electrodes stimulate brain activity through electrical impulses, adjustable according to disease progression, and are controlled by a pacemaker-like device implanted under the patient's skin (Figure 4). Despite the preservation of brain tissue integrity and the reversibility of the surgical intervention, as with all brain surgeries, DBS carries inherent risks and is typically performed in patients who have experienced long-term complications from dopamine or dopamine agonist therapy[85].

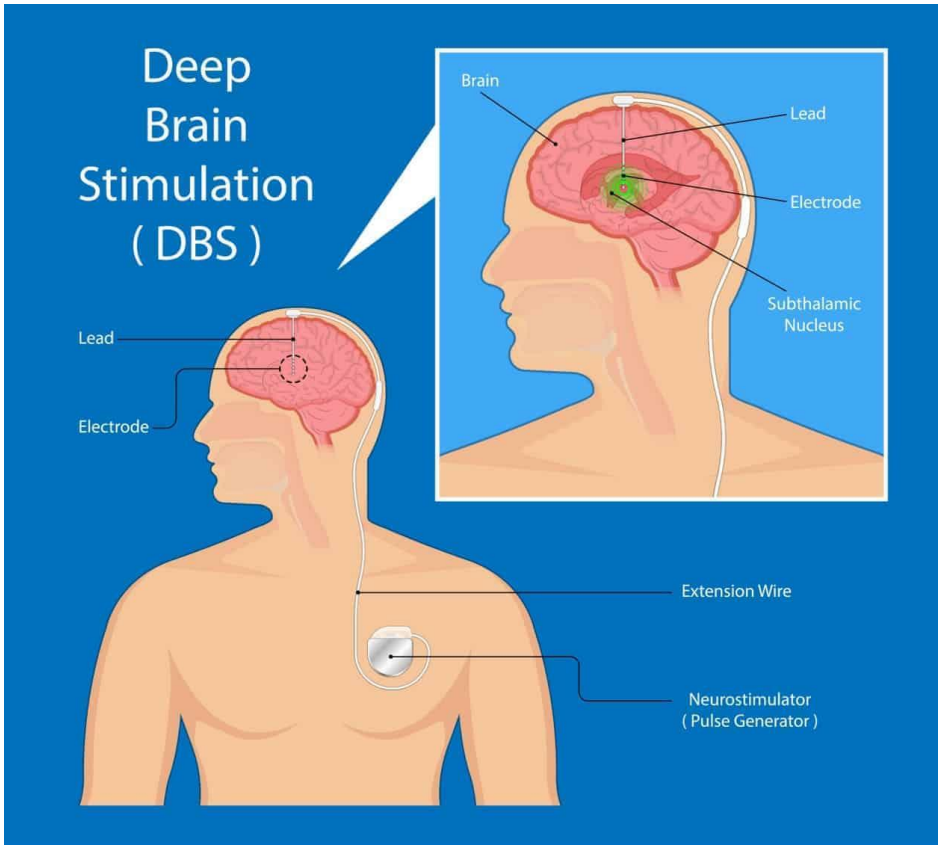

Figure 4: Deep brain stimulation. Electrodes inserted into affected brain regions are stimulated by electric impulses controlled by a pulse generator under the patient's skin. Adopted from Clancy Medial Group (2023)[86].

Other non-pharmaceutical therapies often include physical activity[87]. Regular aerobic exercises not only enhance patients' overall quality of life but also exhibit neuroprotective effects, requiring consistent engagement[88]. Furthermore, specialized programs tailored to the unique needs of PD patients are available to improve symptoms that hinder social interaction, such as speech difficulties and mobility issues[89,90].

Given the reduced quality of life and the fact that conventional therapy or surgery only partially alleviates symptoms, complementary and alternative medicine (CAM) plays a growing role in PD treatment. These CAM therapies encompass mind-body interventions such as Tai Chi, music therapy, yoga, and stress reduction programs[91]. In particular, stress reduction courses have shown to reduce disease progression and mitigate symptoms[92]. Traditional Chinese medicine (TCM) has also shown positive effects on PD symptoms and disease progression, although the molecular mechanisms underlying these techniques are not fully understood. Traditional Chinese acupuncture and Chinese herbal treatments, often used in Asia in conjunction with conventional therapeutic approaches, have found to exhibit a positive impact on PD symptoms and progression[93,94]. Furthermore, an extract of the Ayurvedic plant, HP-200, has been identified as an effective treatment for PD patients[95].

Given that pathological aggregation of aSyn has been strongly linked to PD, modifiers of aggregation have been explored as potential pharmaceutical therapies. SynuClean-D has shown promising results in reducing inclusions formed by aSyn, decreasing aggregation, and attenuating dopaminergic neurodegeneration in animal models[96]. Another modulator of aSyn, Anle138b, modifying pathological aggregates in a structure-dependent manner, reduces the concentration of pathological oligomers. Anle138b has shown the ability to reduce neuronal degeneration and slow disease progression *in vivo*. With good oral bioavailability and effective blood-brain barrier penetration, Anle138b inhibits disease progression even when administered after the disease onset and is presently tested clinically[97,98].

1.2 α-Synuclein

The synuclein family comprises three proteins: αSyn, β-Synuclein, and γ-Synuclein. α- and β-Synuclein are predominantly expressed in the brain, while γ-Synuclein is found primarily in the peripheral nervous system and the retina[99].

aSyn is encoded by the SNCA gene, located on chromosome 4q21.3-q22[100,101]. The gene consists of 7 exons, 5 of which are protein-coding[102]. Although aSyn can be detected in various tissues, it is expressed primarily in the brain, particularly in the neocortex, hippocampus, striatum, thalamus, and cerebellum[103,104]. Within neurons, aSyn is located mainly in presynaptic terminals and close to the nucleus, a characteristic reflected in its name, derived from its synaptic and nuclear cellular localization[105,106].

Under physiological conditions, aSyn functions as an intracellular synaptic protein[103]. However, in patients with PD, aggregates of aSyn have been identified in biological fluids such as cerebrospinal fluid and plasma[107,108]. These aggregates can be detected before the clinical onset of PD symptoms, suggesting aSyn levels in body fluids as a potential biomarker of the disease. Techniques such as protein misfolding cyclic amplification have been utilized to determine the quantity and type of aggregates. This method involves extracting fibrillar aggregates from patient fluids and amplifying them through cycles of incubation with monomeric aSyn, followed by sonication to break down fibrillar structures and initiate a new amplification cycle[109].

The concentration of aSyn monomers in the CNS depends on the balance between synthesis rates, aggregation, and clearance mechanisms[110]. Various pathways, including autophagic-lysosomal and proteasomal pathways, facilitate aSyn clearance[111–114]. Clearance can be mediated by direct proteolysis or by binding to molecular chaperones such as the heat shock protein Hsp70[115,116]. Under pathological conditions, unconventional secretory mechanisms have been observed that allow potentially toxic aggregates to be eliminated from neurons[117,118]. Cell-to-cell propagation can occur through exosomal pathways in clear vesicles, exocytosis and endocytosis, tunneling nanotubes or direct membrane penetration, resulting in extracellular aSyn, which can enter the recipient cell by membrane penetration or receptor-mediated internalization (Figure 5)[119–125]. Extracellular aSyn aggregates, either oligomers or seeds of aSyn fibrils, have been observed to propagate from

neuron to neuron or from neuron to glial cells[120,126]. *In vivo* experiments using grafts have demonstrated this phenomenon, primarily for seeds of aSyn fibrils and to a lesser extent for oligomeric species[126–128]. Upon entering the recipient cell, aggregates of aSyn have the potential to induce intracellular aggregation, initiate neuroinflammation, and accelerate neurodegenerative processes[127,129].

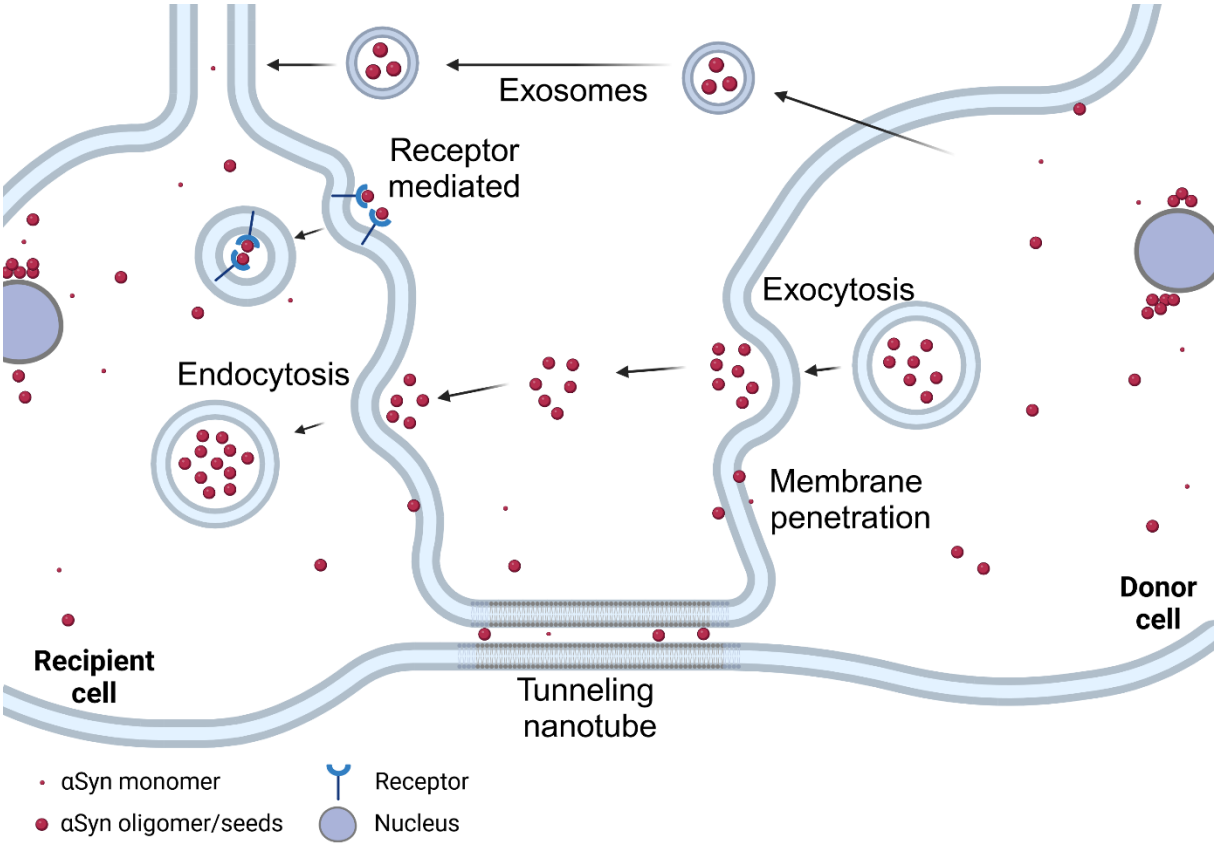

Figure 5: Cell-to-cell propagation of aSyn. aSyn propagation from cell to cell can occur via exosomes, exocytosis and endocytosis, or direct membrane penetration. Furthermore, transmission is possible through tunneling nanotubes or by receptor-mediated internalization.

Furthermore, studies have unveiled the presence of aSyn aggregates in the gastrointestinal tract of PD patients[130,131]. These aggregates can spread through the vagal nerve from the gut to the brain, inducing further cellular damage and contributing to the disease progression[132,133].

1.2.1 Structural Properties of aSyn

aSyn is characterized as a predominantly unstructured protein, existing primarily in its monomeric state[134–137]. To a lesser extent, aSyn tetramers have been identified in the cytosol. However, the existence of this tetrameric structure is controversial but might be favored by imperfect KTKEGV repeats in the primary sequence of aSyn and lack the propensity to further aggregate (Figure 6C and Figure 11)[136,138,139]. However, when aSyn interacts with lipidic membranes or undergoes aggregation, it can adopt distinct secondary and tertiary structures.

The primary sequence of aSyn comprises 140 amino acids, characterized by a low overall hydrophobicity and opposing charges at its termini. It can be divided into three regions: the positively charged N-terminus (residues 1-60, overall charge +4), the hydrophobic non-amyloid-β component (NAC, residues 61-95, overall charge -1) and the negatively charged C-terminus (residues 96-140, overall charge -12; Figure 6A, B). The N-terminus, the primary site of interaction with membranes, can adopt a helical formation. Familial mutations are predominantly located in this region. The NAC component derives its name from its first discovery in the context of AD[104]. It is highly hydrophobic and forms the aggregation-prone core[140]. Deleting this region results in aggregation-deficient aSyn[141]. Under physiological conditions, NAC can form amyloid-like fibrils[140].

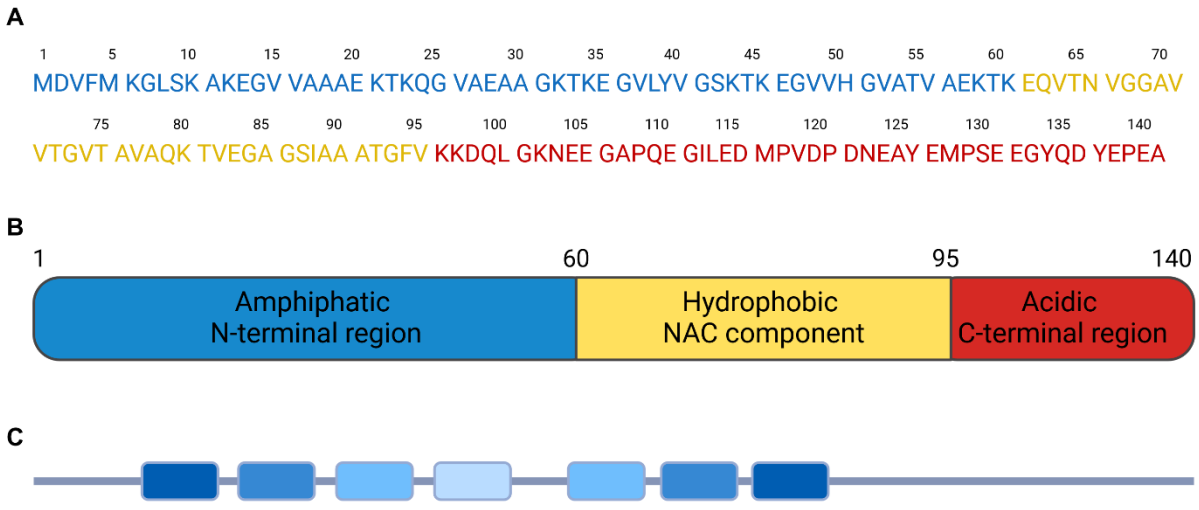

Figure 6: aSyn primary structure. (A) The primary sequence of aSyn is shown in the upper panel. (B) The middle panel shows the N-terminal, NAC, and C-terminal regions. (C) The lower part highlights the position of the seven imperfect KTKEGV repeats within the primary sequence.

Upon binding to membranes and favored by the seven imperfect KTKEGV repeats in its primary sequence, aSyn partly adopts α-helical structures[142]. This α-helical structure can be an extended helix spanning over residues 1-90, or a broken helix formation, that involves a helix from residues 1-37, a linker from residues 38-45, and a second helix formed by residues 46 to 97 (Figure 7)[143–145]. The adopted conformation depends on the number and curvature of the membranes, with aSyn taking the extended helix form when binding to a single membrane and the broken helix form when binding to multiple or highly curved membranes[142,146,147].

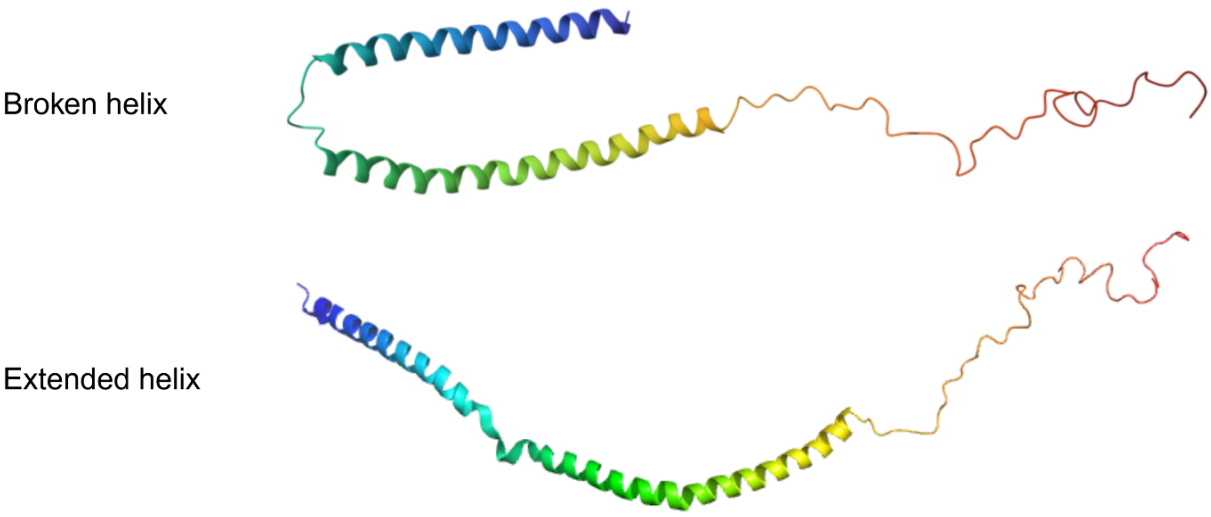

Figure 7: aSyn secondary structures upon membrane interaction. aSyn can adopt a broken or extended helix formation when interacting with membranes (PDB ID: 1XQ8, secondary structure modified using PyMol).

In its aggregated state, aSyn can adopt various conformations, leading to different polymorphs. Techniques like cryo-electron microscopy (cryoEM) and nanoparticles have revealed numerous polymorphs of oligomeric and fibrillar aSyn[148]. The aggregation process involves multiple conformational stages, forming oligomeric intermediates that evolve into distinct fibrillar structures. These oligomeric intermediates are highly heterogeneous and often metastable, making a detailed characterization challenging[149]. The fibrillar product of aggregation includes a variety of polymorphs. Fibrils derived from patients with different synucleinopathies display different structural and biochemical characteristics[150]. Fibril polymorphs can be distinguished by their fibril diameter, the presence of twists, the number and packaging of protofilaments, the side-chain interactions, and the secondary and tertiary structures, among other factors[151].

For wild-type (WT) aSyn, various polymorphs have been described, depending amongst other factors on the N-terminal acetylation of the protein[152,153]. WT polymorphs have been classified as ‘rod’ or ‘twister’. They display a common protofilament kernel structure but differ in their inter-protofilament interfaces caused by differences in the packing of the kernel structure. While rod polymorphs exhibit a Greek-key motif, the twister polymorph is characterized by an ordered bent-β-arch motif. Furthermore, polymorphs 2A and 2B of WT aSyn have been characterized. These polymorphs are also composed of 2 protofilaments each, interacting via salt bridges, while the NAC region shows interactions with the N-terminal region (Figure 8)[152,154].

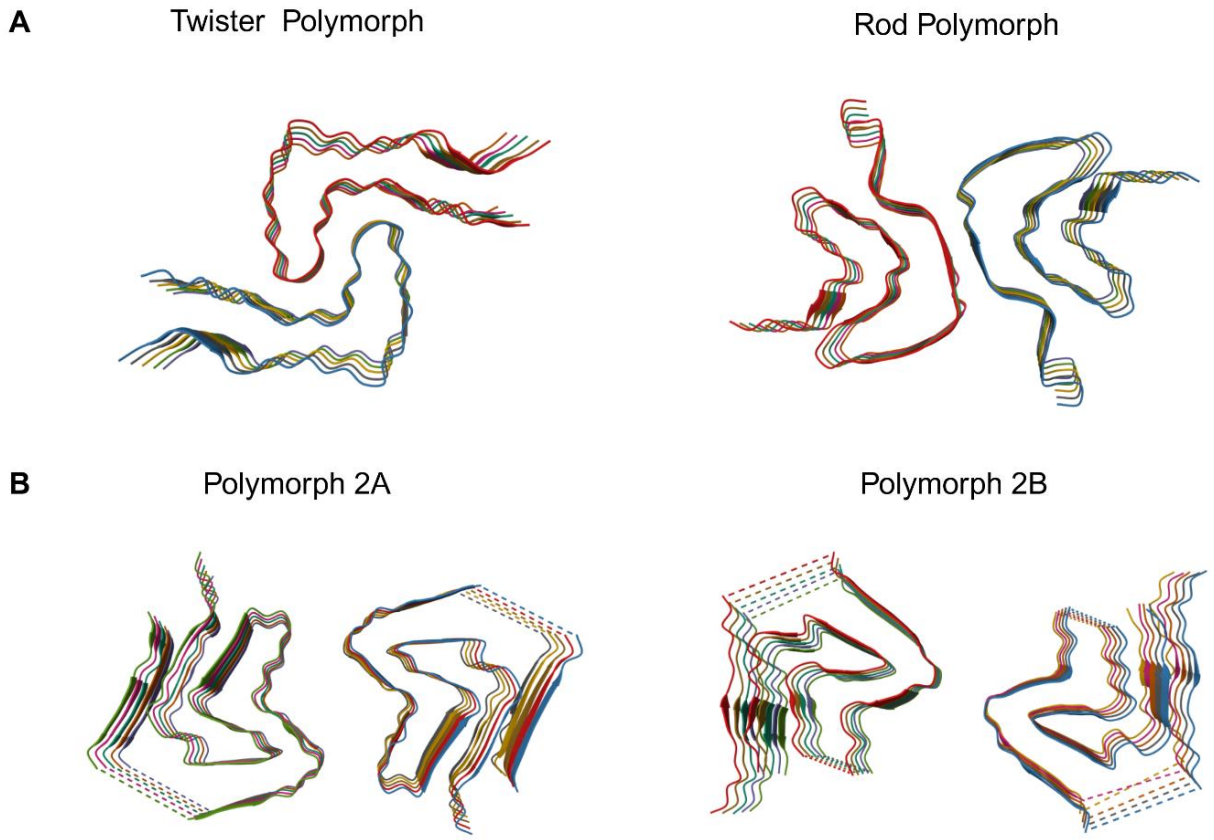

Figure 8: aSyn fibril polymorphs. (A) The upper panel displays the structure of the twister (PDB ID: 6CU8) and rod (PDB ID: 6CU7) polymorphs of aSyn. (B) Polymorphs 2A (PDB ID: 6RT0) and 2B (PDB ID: 6RTB) are shown below.

The relative toxicity of different polymorphs of fibrils and oligomers and their impact on disease progression remain unclear due to the wide variety of aSyn aggregates. Various theories on the origin of toxicity, whether derived from fibrils, toxic oligomers, the aggregation process itself, or a combination, have been discussed. Evidence

supporting either theory has been presented[155,156]. Moreover, a link between the structure of aggregates and their toxicity has been suggested. However, due to the transient character of intermediate oligomers, the origin of the toxicity of aSyn aggregates is difficult to access and to link to a particular structure present in oligomers[156]. Nonetheless, it has been demonstrated that oligomers formed under different conditions not only have distinct morphologies but also different impacts on intracellular calcium levels, seeding abilities of the resulting fibrils, and membrane permeabilities[155].

1.2.1.1 aSyn and Lipid Membranes

The ability of aSyn to interact with lipid membranes not only modulates its physiological function, but also plays a crucial role in its clearance and aggregation tendencies. The affinity of aSyn for synaptic membranes is subject to various factors, including membrane composition, charge, fatty acid content, aSyn acetylation, and specific aSyn mutations. The aggregation process is predominantly influenced by the lipid:protein ratio (L:P), further discussed in section 1.2.3 “Pathological Aggregation”.

Upon binding to membranes, the initial 25 amino acids serve as an anchoring segment, adopting an α-helical conformation, tightly associating with the membrane[157]. Amino acids 26 to 97 can adopt a helical structure during membrane interactions but exhibit greater flexibility, constituting the membrane sensing region. On the contrary, the highly unstructured, negatively charged and extremely flexible C-terminal region shows minimal interactions with membranes[158].

To facilitate the clearance of aSyn from the cell through the autophagic-lysosomal pathway, aSyn must first bind to vesicle membranes for internalization. Subsequently, it reaches the lysosomal compartments, where it undergoes degradation[114].

1.2.2 Physiological Role of aSyn

During the process of cellular signal transduction, neurotransmitters must be released into the synaptic cleft to effectively transmit signals. This crucial task involves the trafficking of small presynaptic vesicles from their stabilized pool to the

synaptic cleft, where they subsequently fuse with the presynaptic membrane, releasing their contents. Mediating this process are membrane-binding proteins that assemble in the soluble N-ethylmaleimide sensitive factor activating protein receptor (SNARE) complex, overcoming repulsive forces between negatively charged opposing membranes[159].

SNARE proteins, including vesicle-associated membrane proteins (VAMPs), synaptosomal-associated protein 25 (SNAP-25), and syntaxins, play a crucial role in this process[160–162]. SNARE proteins located on synaptic vesicles, such as VAMP2, are known as v-SNARES, while those associated with the target membrane, such as SNAP-25 and syntaxin1A, are termed t-SNARES. SNARE proteins interact with each other by forming four-stranded coiled-coil core complexes. These complexes are composed of one α-helix of each VAMP2 and syntaxin1A and two α-helices from SNAP-25, facilitating membrane approximation and inducing membrane curvature[163]. The fusion process involves hemifusion, followed by the opening and expansion of a fusion pore, ultimately leading to complete membrane fusion. After neurotransmitter release, vesicles are recycled back into the pool of synaptic vesicles (SVs)[164,165]. Recent findings indicate that aSyn interacts indirectly with the SNARE complex through VAMP2 (Figure 9)[166–168].

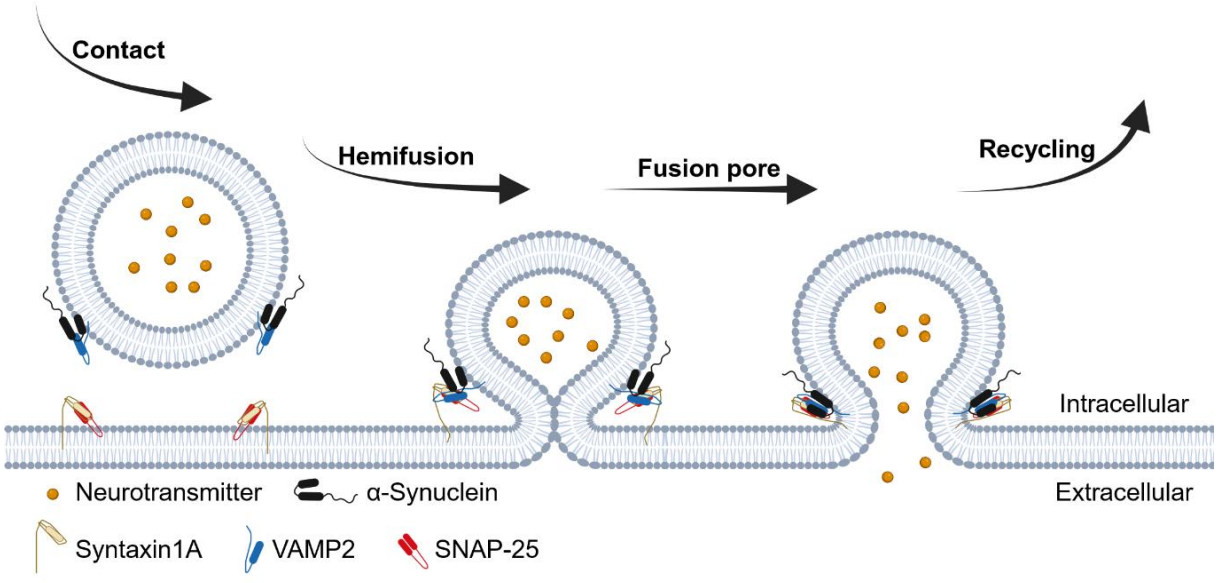

Figure 9: SNARE-mediated neurotransmitter release. VAMP2, located on the synaptic vesicles' (SV) membrane, forms a complex of four helices with syntaxin1A and SNAP-25, located on the target membrane, to mediate neurotransmitter release. Upon interaction of these membrane proteins, the SV and the target membrane come in contact. After a hemifusion, a fusion pore opens, and the neurotransmitter is released. The SV is recycled into the SV pool. aSyn is involved by interacting with VAMP2.

During the 2000s, *in vivo* studies established a link between aSyn and its synaptic function. aSyn knockout mice exhibited increased dopamine release upon electrical stimuli, suggesting a role for aSyn as an activity-dependent negative regulator of dopamine neurotransmission[169]. Furthermore, depletion of aSyn from cultured primary hippocampal neurons reduced the distal pool of presynaptic vesicles, which implies a contribution of aSyn to sustain the SV pool[170]. Mechanistically, aSyn is involved in maintaining the SV pool by clustering the vesicles and restricting their mobility. To fulfill this role, aSyn adopts a broken helix formation, enabling it to bind to multiple membranes simultaneously[171]. aSyn is also involved in promoting membrane curvature, SV docking and recycling[167,172,173].

Given that aSyn is predominantly located within presynaptic terminals with a minor extracellular presence, its interaction with inner and outer presynaptic membranes (IPM and OPM, respectively) has been investigated. Notably, aSyn exhibits a higher affinity for IMPs; however, its affinity to the OPM increases with the increase in negatively charged gangliosides (Figure 10)[174].

In summary, aSyn, primarily located within presynaptic terminals, can adopt various conformations, existing either as an unstructured, soluble protein or adopting helical conformations upon membrane binding. In its structured conformation, aSyn can bind to multiple membranes simultaneously, supporting the maintenance of the SV pool, their trafficking toward the synaptic cleft, their docking and release of neurotransmitters through the interaction with the SNARE complex, and their recycling for subsequent signal transmission cycles (Figure 10).

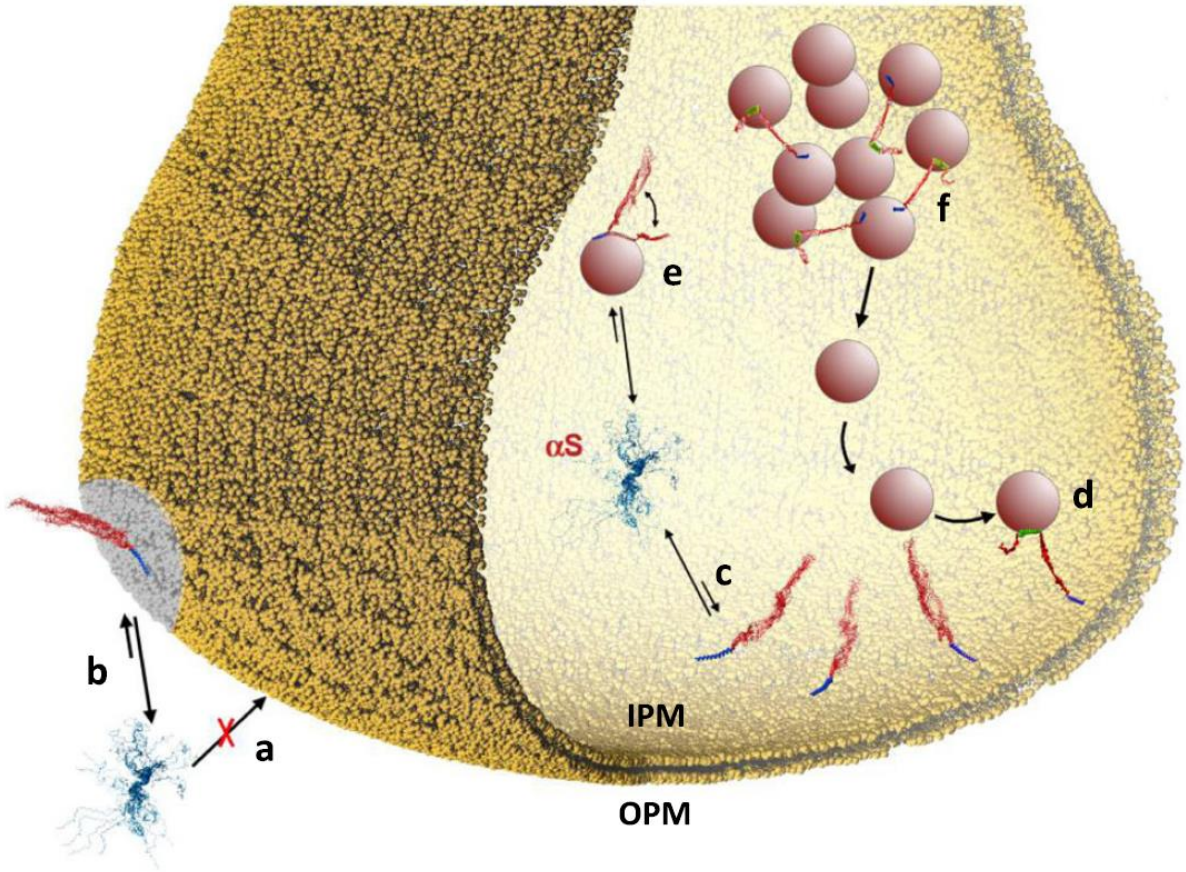

Figure 10: Physiological role of aSyn. Extracellular aSyn does not interact with the outer presynaptic membrane (OPM, a). However, with an increase in the content of gangliosides in the OPM, some aSyn monomers adopt an α-helical structure and interact with the OPM (b). Intracellular aSyn exists in an equilibrium between its unstructured and membrane-bound state (c). It can bind to synaptic vesicles (SVs, e) and mediate the contact between SVs and the inner presynaptic membrane (IPM, d). It is also involved in maintaining the SV pool by binding more than one vesicle at a time and thus connecting them in a network structure (f). Adopted from Man *et al.* (2021)[174].

The identification of non-aggregating multimers of aSyn within the cell has led to discussions about how aSyn fulfils its physiological role not only in its monomeric state but also as a multimer[175]. Evidence suggests that aSyn multimers, more so than monomers, are involved in clustering the SV pool[172]. Additionally, the promotion of SNARE complex assembly has been associated with multimeric, membrane-bound aSyn, rather than its monomeric cytosolic state[176]. This duality in the nature of aSyn, existing both as monomers and multimers, introduces a layer of complexity to its engagement in synaptic function and regulation.

1.2.3 Pathological Aggregation of aSyn

Unstructured or partially structured monomers of aSyn can undergo conformational changes, leading to an aggregation-prone monomer that interacts with neighboring aSyn molecules, forming aggregation prone nuclei. The nuclei attract more monomeric aSyn, leading to the formation of oligomers. These oligomers, stabilized by β-sheet interactions, have the potential to further aggregate, resulting in insoluble protofibrils that ultimately polymerize. The resulting cross-β-sheet-rich amyloidogenic fibrils are deposited in LBs (Figure 11)[177].

The primary nucleation step, in which monomers cluster to form aggregation-prone nuclei, is crucial for aSyn aggregation. This step can be enhanced by the presence of membranes, as aSyn becomes partially structured and can interact with neighboring aSyn molecules on the membrane surface[178,179]. As discussed in section 1.2.1 various oligomeric structures of aSyn have been identified, with some lacking the ability to progress into fibrils, known as ‘off-pathway’ oligomers[180]. ‘On-pathway’ oligomers in contrast continue to aggregate, evolving into protofibrils. These protofibrils can interact with each other to form the end product of aggregation, the amyloidogenic fibrils.

A secondary nucleation process can occur on the surface of protofibrils and fibrils, involving the formation of new fibrils facilitated by pre-existing fibrils[181]. aSyn monomers interacting with the (proto-)fibrils convert into aggregation-prone nuclei, further aggregating into oligomers and fibrils[182]. Additionally, fragmentation can break fibrils into smaller structures, referred to as seeds[183]. These seeds accelerate fibril growth by bypassing the primary nucleation process, acting as a template for fibril elongation and recruiting aSyn monomers to their ends (Figure 11)[184]. Notably, the aggregation process and resulting structures are sensitive to environmental factors such as buffer and salt concentrations, pH, temperature, and lipid composition[185].

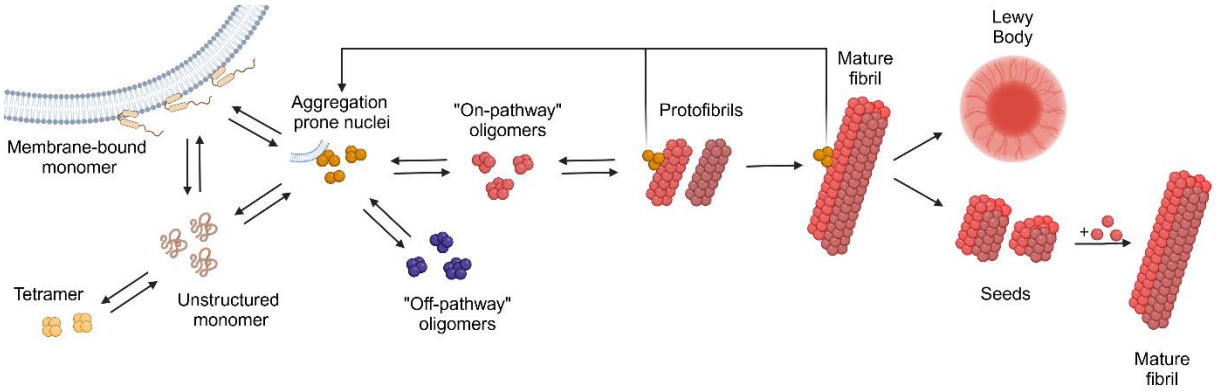

Figure 11: Aggregation of aSyn. aSyn mainly exists in the cell as an unstructured monomer, which can assemble to tetramers or adopt a membrane-bound formation with helices as a secondary structure element. The monomer can form nuclei that are prone to aggregation, which can attract other monomers and become 'off-pathway' oligomers, lacking the ability to further aggregate. The nuclei can also aggregate into 'on-pathway' oligomers, which can further aggregate to protofibrils and mature fibrils. Fibrils are deposited in LBs, or fragment into seeds. The seeds attract soluble aSyn monomers to get prolonged into mature fibrils. On the surface of protofibrils and mature fibrils, aggregation prone nuclei can form, which accelerates the aggregation process by skipping the first step of aggregate prone nuclei formation.

1.2.3.1 Kinetics

The aggregation process is often monitored by Thioflavin-T (ThT) fluorescence. Upon binding to cross-β-sheet structures of amyloid fibrils, ThT shifts its emission spectrum[186]. Amyloid fibrils are characterized by a long, ribbon-like morphology. The laminated β-sheet strands run perpendicular to the fibril axis and produce characteristic surface side-chain grooves, where ThT binds to[187]. Even though ThT is commonly used in the many research areas, it is crucial to note that ThT's reliability for fibril quantification is compromised due to differential binding to distinct polymorphs, even when they share a similar β-sheet content[188,189]. Moreover, the presence of ThT throughout the aggregation process can alter fibril structure and fibrillization rates by binding to primary nuclei or aSyn monomers, stabilizing structures prone to aggregation. This stabilization of intermediates and an interaction of ThT with the C-terminus of aSyn lead to an increased fibrillization rate[190]. To overcome its limitations, ThT assays are often complemented with other methods to cross-verify results. Despite its challenges, ThT remains a widely employed tool for studying the kinetics of aSyn aggregation.

Kinetically, monitoring the aggregation of aSyn results in a sigmoidal curve and can be described in three phases[177]. The lag phase, marked by primary nucleation, lacks

ThT fluorescence due to the absence of amyloid fibrils. The elongation phase follows, characterized by exponential growth of fibrillar structures, reflected in increasing ThT fluorescence. The final phase reaches a plateau, indicating an equilibrium between free and aggregated aSyn, with a constant relative ratio of monomers to fibrils (Figure 12).

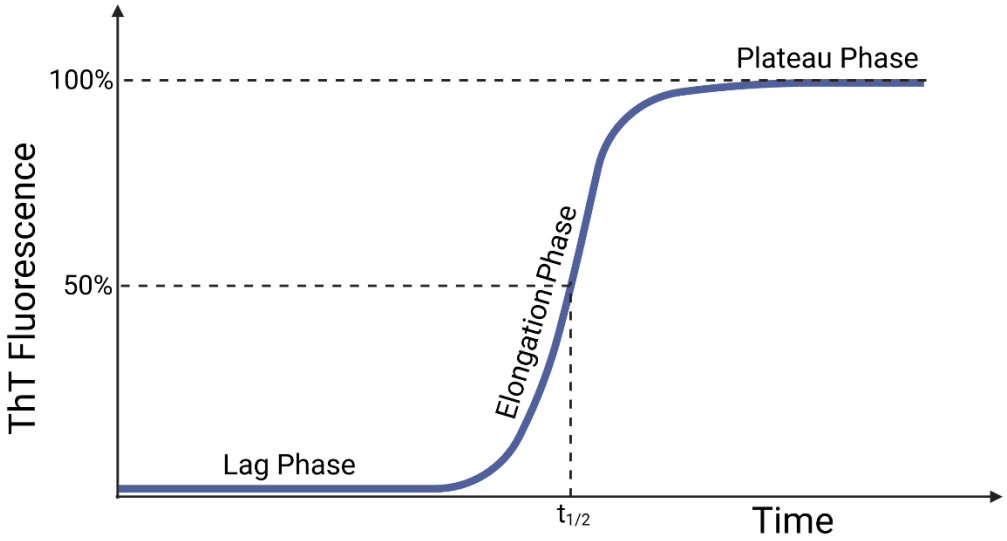

Figure 12: Time course of aSyn aggregation. The ThT fluorescence curve during aSyn aggregation demonstrates a sigmoidal pattern. During the lag phase, when first nuclei and oligomers are forming, no ThT fluorescence is detected. As fibril elongation dominates, fluorescence rapidly increases until reaching an equilibrium between free and aggregated aSyn (plateau phase). At 50% of the maximal emitted ThT fluorescence, the half time of the aggregation process ($t_{1/2}$) can be estimated.

The kinetics of aSyn aggregation involve various parameters. The half time of aggregation is defined as the time point at which 50% of the maximum fluorescence is reached. Furthermore, the velocity of elongation can be described considering the slope of the ThT fluorescence during the elongation phase. The lag time reveals the duration of primary nucleation, observable in the absence of fibrillar structures at the aggregation's onset. The addition of seeds shortens the lag phase, bypassing primary nucleation and providing a template for direct elongation[184].

The presence of membranes can have an ambivalent impact on aggregation depending on the ratio between lipids and protein L:P. If the L:P value is high, hence there is an excess of membranes, most aSyn monomers will be interacting with the membrane. Thus, free aSyn molecules in solution are sparse and are not sufficient to facilitate aggregation. At low L:P ratios close to the $L:P_{max}$ value, an equilibrium between free and membrane-bound aSyn accelerates aggregation. Partially

structured aSyn molecules interact with neighboring aSyn molecules bound to or in proximity to the membrane, shortening the lag phase by initiating primary nucleation events. In cases of very low L:P, the impact on primary nucleation is negligible due to the limited membrane surface, with most aSyn remaining in solution and only a few molecules binding to membranes[178] (Figure 13).

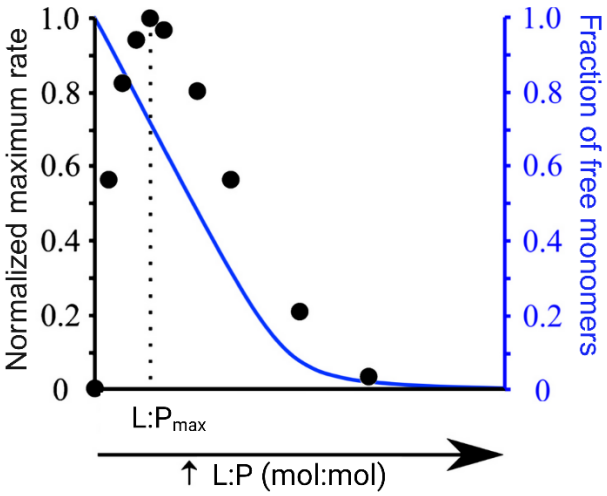

Figure 13: Influence of the L:P ratio on the kinetics of aSyn aggregation. The normalized maximum rate of aggregation (black) and the fraction of free monomers (blue) is plotted against the L:P ratio of DMPS:aSyn. The L:P ratio at the maximum aggregation rate is indicated as L:P$_{max.}$ Figure adopted from Galvagnion *et. Al* (2015, 2017)[178,191].

1.2.3.2 Toxicity

The precise cause of toxicity induced by pathological aggregation of aSyn remains elusive. Theories point in various directions: The aggregation process itself has been noted to cause toxicity, as have isolated fibrils and oligomers. Conversely, certain oligomeric and fibril polymorphs seem non-toxic. Moreover, LBs, initially considered as the cause of neurological cell death, are now speculated to play a neuroprotective role by enclosing toxic aggregates within cellular compartments. Toxicity might be generated by the interaction of toxic aggregates with organelles such as mitochondria, autophagosomes, lysosomes, etc.[192].

There is evidence pointing towards fibrils as the toxic aggregate species, since WT and A30P aSyn, which are able to form fibrils, but not the triple mutant A30P/A56P/A76P, lacking fibrillization capacities in solution, are leading to greater dopaminergic neurodegeneration[193]. Additionally, modifications like phosphorylation

at residue 129 (serine), inducing fibrillization, lead to increased toxicity and behavioral deficits in genetic rat models of PD[194].

On the other hand, mutations such as E57K, which enhance the formation of aSyn oligomers rather than driving fibrillization, prove highly toxic to dopaminergic neurons[195]. High molecular weight oligomers exhibit greater toxicity than their low molecular weight counterparts, disrupting calcium homeostasis, compromising membrane integrity, inducing reactive oxygen species production, and phospholipid peroxidation in the membrane[196]. Toxic aSyn oligomers interfere with the axonal transport of synaptic proteins, resulting in dysfunctional synapses and neurodegeneration, and have been shown to be able to disrupt the microtubular network[197,198]. Furthermore, it could be demonstrated that oligomers can cause toxicity by forming membrane pores[199]. Other mechanisms of generating toxicity are related to mitochondria[200]. Mitochondrial lipids can trigger oligomerization of aSyn, resulting in the accumulation of reactive oxygen species by permeabilizing the mitochondrial membrane leading to increased toxicity and ultimately cell death[201].

A promising mechanism of oligomer-mediated toxicity relates to the increased hydrophobic surface of oligomers in comparison to fibrils. This enlarged hydrophobic surface can lead to membrane disruption and efflux of ions[202]. The mechanism of fibril-mediated toxicity on the other hand seems to be related to the ability of spreading between neurons, which in turn depends on the fibril's conformation. Given the evidence of toxicity exhibited by certain oligomers and fibrils but not others, toxicity might not be generated by a certain species of aggregates but rather by the presence of particular secondary or tertiary structures within these aggregates. To date, the cause of toxicity remains under debate.

1.2.4 Mutations

Various mutations related to aSyn can cause familial forms of PD. Duplication or triplication of the SNCA gene, resulting in elevated aSyn levels within cells, is classified as a familial mutation and can be a causative factor for PD[203,204]. Additionally, mutations in the promoter region of the SNCA gene can enhance aSyn expression, resembling overexpression seen in gene multiplication[205].

Since 1997, an increasing number of point mutations within the SNCA gene have been identified as causal factors for familial PD, including A53T, A30P, E56K, H50Q, G51D, A53E, A53V and V15A[65,206–213]. Notably, these mutations are concentrated in the N-terminal region of aSyn, underlining its significance in disease development and progression (Figure 14). The mutations can be categorized into early and late onset mutations. Early onset mutations, such as A53E, A53T, and G51D, lead to PD development in younger individuals, with onset as early as 20-30 years of age. A30P and E46K are also considered early onset mutations, resulting in PD development around the age of 55. Late onset mutations, including H50Q and A53V, lead to disease manifestation later in life, typically above the age of 60[214]. Furthermore, certain mutations (A30P, G51D, A53E) are associated with a delay in aSyn aggregation, while others (E46K, H50Q, A53T, A53V) accelerate aggregation. Notably, the acceleration of aggregation does not coincide with early onset mutations. This lack of correlation between enhanced aggregation and disease onset highlights the need for investigations on the causes of toxicity (Figure 14)[215].

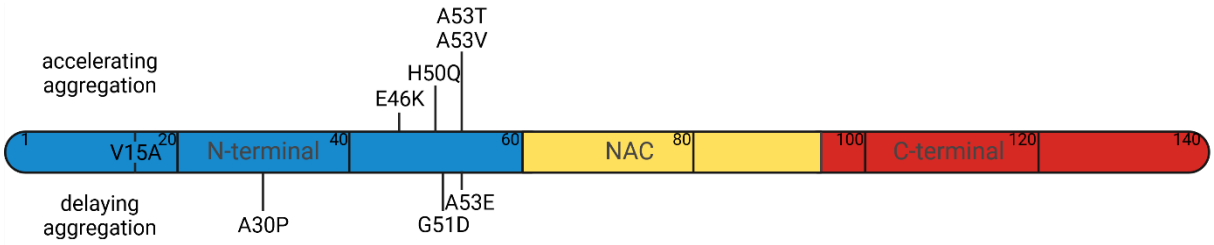

Figure 14: aSyn familial mutations. Displayed are the positions of the familial mutations of aSyn. The mutations shown above the aSyn representation accelerate aggregation (E46K, H50Q, A53T, A53V), while the ones depicted below delay the aggregation of aSyn (A30P, G51D, A53E).

In general, early onset mutations favorize oligomer formation, and do not drive fibrillization[216]. Mutations not only influence the aggregation kinetics of aSyn, driving oligomerization or fibrillization, but also result in different fibril polymorphs of aSyn[214]. Each new familial mutation discovery increases the diversity of polymorphs, while the link between toxic effects and these polymorphs remains a subject of investigation[217,218].

Mutations can also alter the interaction with membranes. The introduction of a negative charge, disruption of helical structures crucial for membrane binding, and the orientation of the mutation within the helical structures can modify affinity and aggregation of aSyn in the context of lipidic membranes[219,220].

1.2.5 Post-translational Modifications of aSyn

Post-translational modifications (PTMs) are prevalent in the aSyn protein, contributing to its functional and pathological aspects. In addition to C-terminal truncation and N-terminal acetylation, observed frequently in patients with PD, other PTMs are distributed throughout the length of the protein (Figure 15)[221,222].

In the human body, aSyn undergoes N-terminal acetylation, inducing α-helicity and increases membrane affinity[223]. In addition, this PTM has been shown to decrease the rate of aSyn aggregation[224]. Notably, the most common phosphorylation at position 129 (serine) is a crucial PTM, commonly associated with PD and considered a hallmark of LBs. It is found in 90% of aSyn within LBs, contrasting with its presence in only 4% of aSyn under physiological conditions[225,226].

Various other PTMs, such as N-acetylglucosamine modification of serine and threonine, the addition of small ubiquitin-like modifiers (SUMOylation) to lysine, tyrosine nitration, ubiquitination or glycation of lysine, serine, threonine and tyrosine, and methionine oxidation, occur at different residues (Figure 15)[227–233]. These modifications can have diverse effects on aSyn aggregation and toxicity. For instance, tyrosine nitration and lysine glycation could be associated with enhanced neurodegeneration, while methionine oxidation inhibits fibrillization *in vitro*[229,232,233].

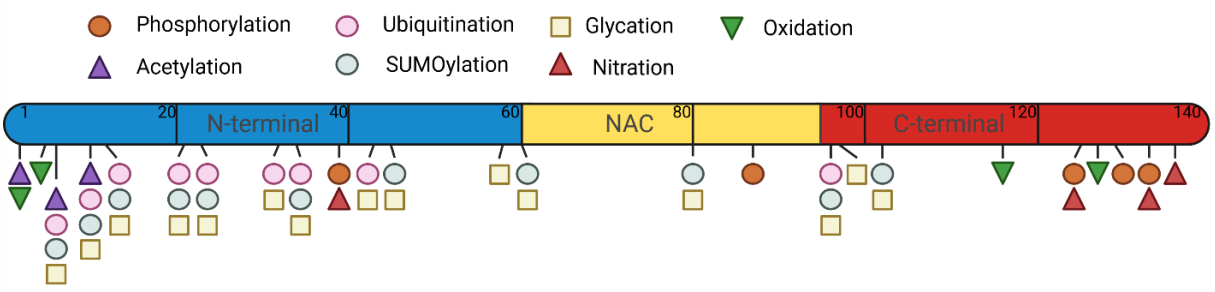

Figure 15: Post-translational modifications of aSyn. PTMs are found throughout the protein. The relative positions of phosphorylation, ubiquitination, glycation, oxidation, acetylation, small ubiquitin-like modifiers (SUMOylation) and nitration are displayed.

Beyond their impact on aggregation and toxicity, PTMs significantly influence the interaction of aSyn with membranes in terms of affinity, binding, and aggregation, highlighting their importance in the context of pathological aSyn aggregation[221,234].

Moreover, PTMs hold potential as biomarkers for detecting changes in aSyn, enabling early diagnosis before symptom onset[235].

Some PTMs can modify antibody binding sites. Truncation can entirely remove the binding site of antibodies, while other PTMs hinder antibody recognition by modifying the recognition site, resulting in decreased affinity. Consequently, when quantifying aSyn levels via antibodies, it is essential to consider the impact of PTMs[235].

1.2.6 The Position 39

The position 39 in aSyn is an important residue for various reasons. CryoEM visualizations of the two major polymorphs 2A and 2B of WT aSyn show that residue Y39 is able to interact with Y39 of the following aSyn, which can contribute to fibril stabilization. Furthermore, the visualization demonstrates that Y39 points towards the outside of the fibril, allowing the interaction with membranes (Figure 16)[153,236].

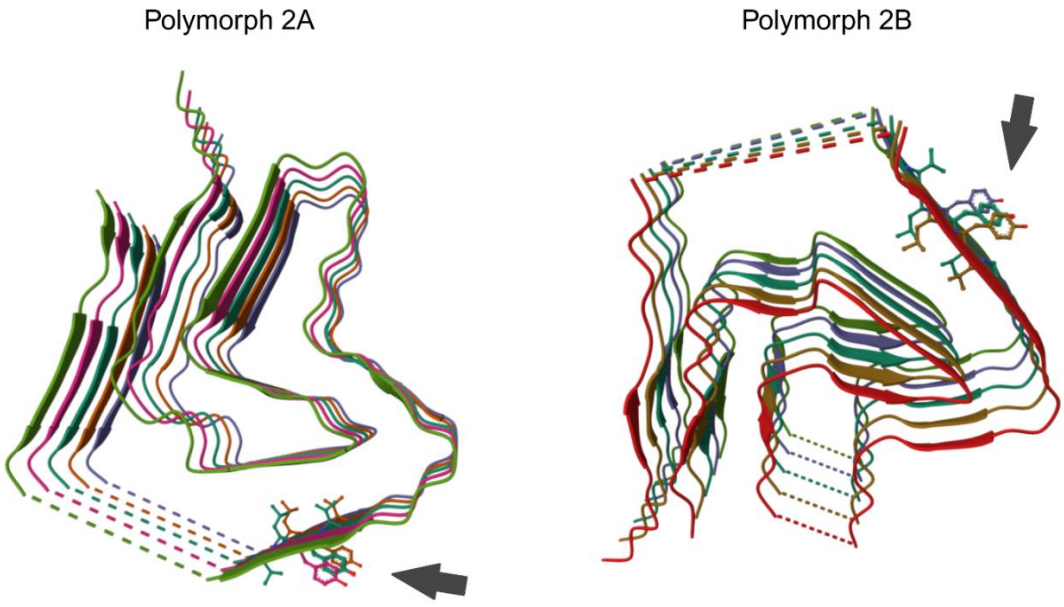

Figure 16: The Y39 residue in polymorphs of WT aSyn fibrils. Displayed are polymorphs 2A (PDB ID: 6RT0) and 2B (PDB ID: 6RTB). The residue Y39 and is indicated by black arrows.

Furthermore, Y39 is situated within the linker region connecting the two α-helices formed upon membrane interaction (Figure 17). Alterations to this linker have demonstrated to modify membrane interactions, particularly the docking of vesicles[144,179]. Aromaticity at position 39 is essential for aSyn binding to gangliosides.

The aromatic side chain embeds in the polar-apolar interface, stabilizing its apolar structure by interacting with sugar residues of gangliosides. This stabilization facilitates the insertion of aSyn into the membrane surface, making position 39 and its aromaticity a key determinant of membrane interaction[237].

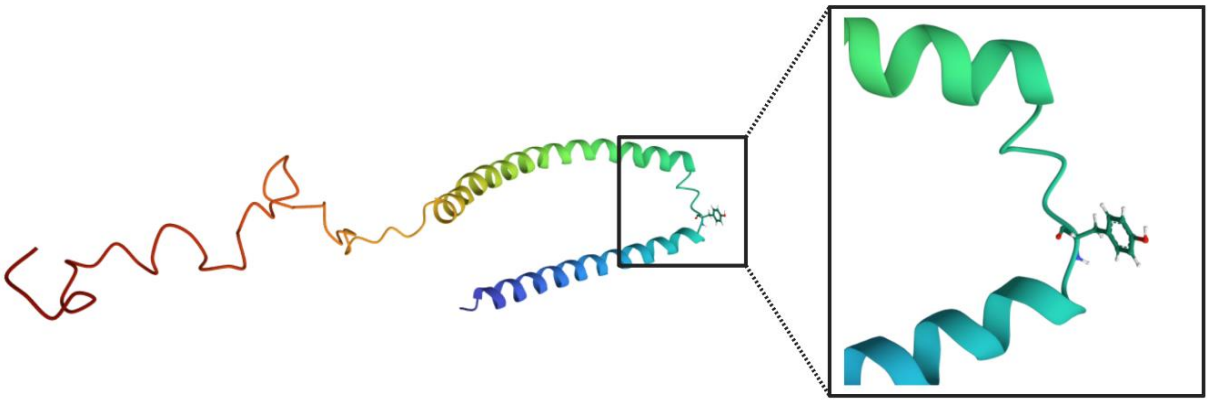

Figure 17: The Y39 residue in the membrane-bound state of WT aSyn. The membrane-bound aSyn (PDB ID: 1XQ8) forms two α-helices, connected by a linker. The tyrosine residue at position 39 is shown here, positioned within the linker between the helices.

Concerning aSyn aggregation, the segment containing amino acids 36-42 have been identified as crucial. Mutations in this region result in the abolition of aggregation *in vitro* and *in vivo*, accompanied by decreased membrane affinity[238]. Notably, within this region, positions L38, Y39 and S42 emerged as the most important residues. The mutation of leucine to isoleucine at position 38 increases the speed of fibril formation, while the mutation to methionine at the same position showed to lack fibril formation abilities and to protect from proteotoxicity[239]. S42, when mutated to alanine, prevented aggregation *in vitro* and in *C. elegans*[239,240]. Similar results have been seen for the mutation to alanine at position 39, which completely prevents the formation of fibrillar structures[239,241,242].

Additionally, the compound phthalocyanine tetrasulfonate (PcTS), known to inhibit amyloid fibril formation, interacts with aromatic residues F4, Y39, and F94, with Y39 serving as the main anchoring residue[243]. The removal of aromaticity at position 39, through mutations to alanine or leucine (but not phenylalanine, which preserves aromaticity), negated the inhibitory effect of PcTS[244].

Position Y39 is also a target for molecular chaperones, which often recognize a canonical motif comprising the N-terminus and a segment around Y39 of aSyn,

hindering its aggregation[245]. The position Y39 is also targeted by the protein kinase c-abl. This kinase has demonstrated to phosphorylate aSyn at positions Y125 and Y39, with Y39 identified as the primary phosphorylation site[246,247].

Taken together, position Y39 emerges as a key player in many aspects of aSyn function and dysfunction, encompassing membrane binding, aggregation, and interactions with other proteins and compounds.

1.3 *Caenorhabditis elegans* as an Animal Model

Caenorhabditis elegans (*C. elegans*), a globally distributed nematode ranging from 0.25 mm (hatched larvae) to 1 mm (adult) in length, has been an important model organism since the 1960s, initially in genetics later also in other research areas[248]. The advantages of employing *C. elegans* as a model organism are manifold: its compact size, high breeding capacity (up to 200 progeny), ease of cultivation with low maintenance costs, transparency, rapid generation time for mutant strains, long-term cryopreservation, and the ability to repress protein expression through RNA interference methods, where RNA is directly applied via the animal's food. Additionally, *C. elegans* is non-pathogenic to humans as it cannot thrive at body temperatures[249]. The transparency of the nematode facilitates researchers in visualizing proteins within specific cells throughout its lifespan within the living animal.

C. elegans exist predominantly as hermaphrodites, with only a small percentage developing into males to extend the genetic pool. The duration of the life cycle depends on the environmental temperature; the following time indications refer to 22 °C. The hermaphrodite undergoes embryogenesis, concluding in approximately 3 hours, leading to egg laying. After 9 hours of development, the larvae hatch, with newly hatched larvae referred to as L1. The nematode progresses through four larval stages (L1 to L4), with L1 lasting 12 hours and subsequent stages lasting between 8 to 10 hours. Between each larval stage, the larvae enter lethargus, a sleep-like period of inactivity, during which a new cuticle is formed, and the old one is molted[250]. Young adults lay eggs for 2-3 days, after which the nematodes live several more weeks before they die by senescence (Figure 18)[249].

In non-favorable conditions such as a lack of food, L1 larvae can enter L1 arrest, delaying development until conditions improve. Moreover, under severe conditions of crowding, starvation, or high temperatures, late L1 larvae can enter the Dauer state, characterized by enhanced resistance to chemicals, sealing of the mouth, and arrest of development, lasting up to 4 months until conditions become more favorable (Figure 18)[251].

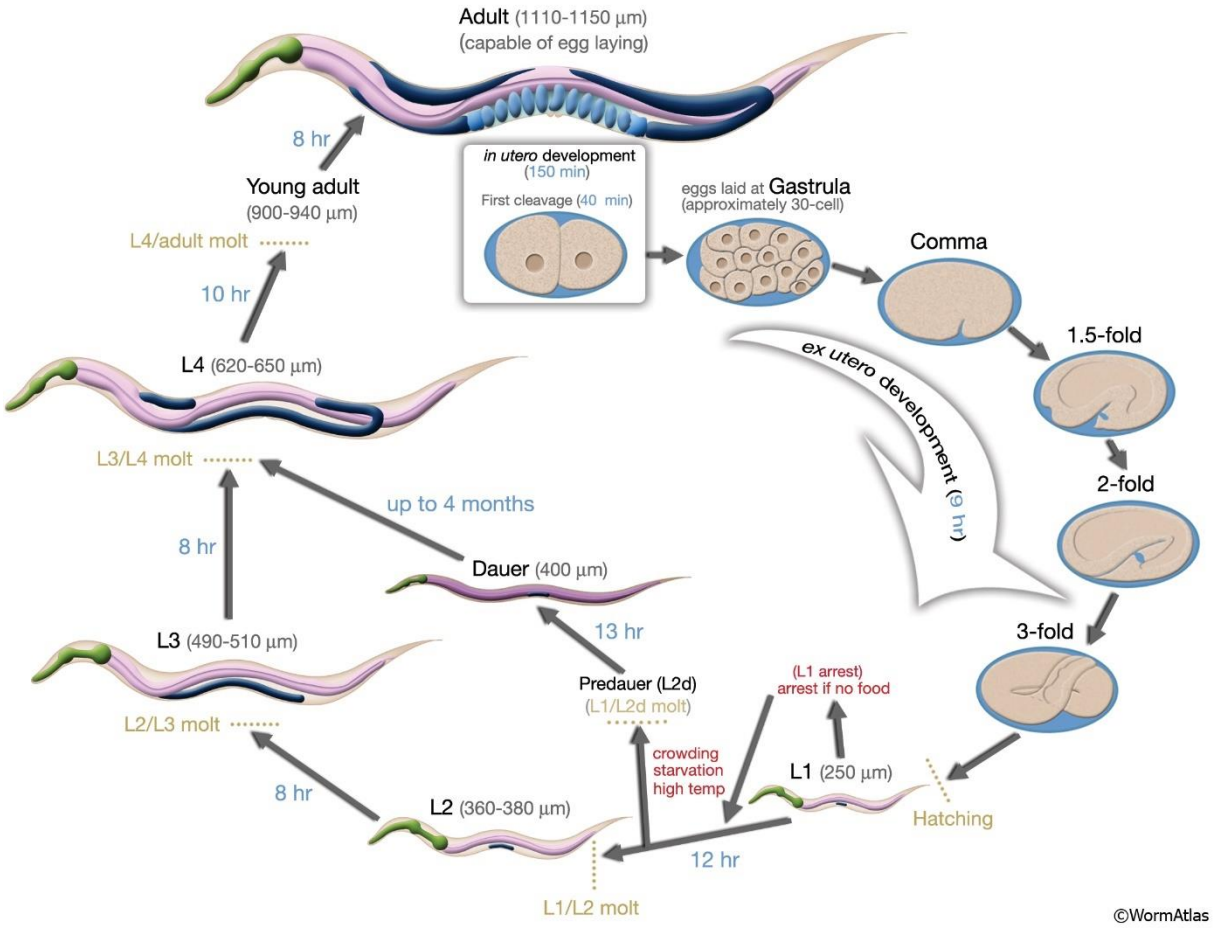

Figure 18: *C. elegans* life cycle at 22 °C. The life cycle of *C. elegans* begins with embryogenesis, lasting approximately 3 hours, followed by egg laying. After 9 hours, the larvae hatch and progress through four larval stages (L1 to L4), with each stage lasting between 8 to 12 hours, indicated by blue numbers. Young adults lay eggs for 2-3 days. The body length of the animal at each stage is shown next to the stage name. Adopted from Altun *et al.* (2006)[252].

C. elegans, the first multicellular organism with a fully sequenced genome, comprises 959 cells in the hermaphrodite, six chromosomes, and around 20 000 genes. Remarkably, 40-50% of protein-coding genes in *C. elegans* have orthologs in humans, and 60-80% of human disease-causing genes have orthologs in this nematode [253,254]. The ease of creating mutant strains within 1-2 weeks through

microinjection of plasmids into the nematode's gonads makes *C. elegans* a handy instrument in drug discovery for testing drug toxicity and efficacy[255].

In PD research, *C. elegans* serves as a widely used model organism. Since it lacks an ortholog for aSyn, expressing aSyn tagged to yellow fluorescent protein (YFP) enables the visualization of human aSyn within the living animal. This model replicates several PD features, including rigidity, neuronal degeneration, inclusion formation, and positive responses to dopamine treatment therapies [256].

1.3.1 Neuronal System of *C. elegans*

The neuronal system of an adult hermaphrodite comprises 302 neurons[257]. *C. elegans* is the only organism in which all neuronal cells could be connected and mapped, providing the most comprehensive nervous system connectome to date. Neurons are organized in several ganglia in the head, where they form a nerve ring, and in the tail. Other cell bodies are organized in a spinal cord-like ventral nerve cord, while the dorsal nerve cord is constituted by projections of the cell bodies (Figure 19)[258].

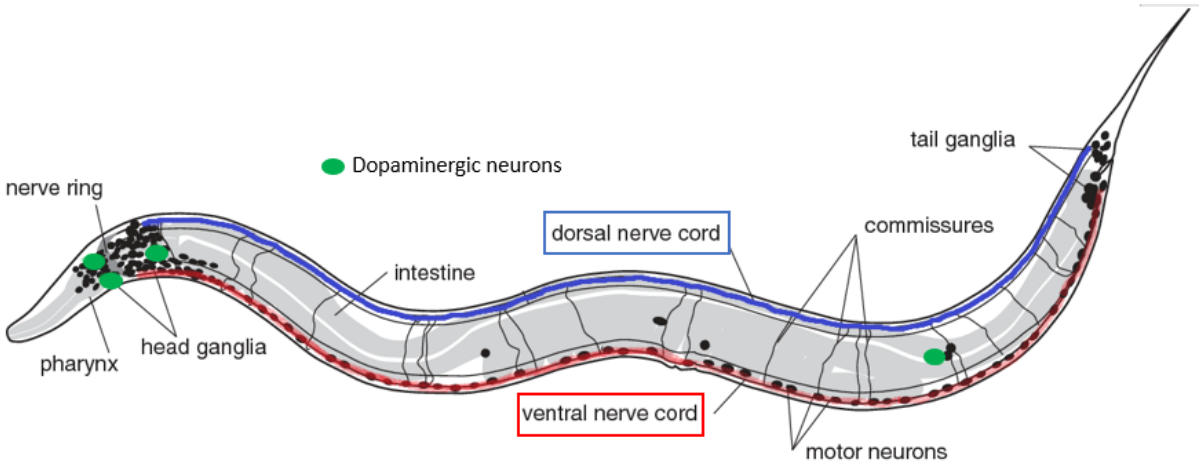

Figure 19: Neuronal system of *C. elegans*. Displayed in black are the neuronal cell bodies, clustered in the head, tail, and ventral cord (red). The dorsal cord (blue) is constituted by neuronal projections. The position of the 8 dopaminergic neurons is highlighted in green for one lateral side of the animal. Adopted from Jorgensen *et al.* (2016)[259]

C. elegans exhibits 8 dopaminergic neurons, with 6 located in the head region and 2 posterior neurons closer to the tail. The dopaminergic neurons in the head region consist of a pair of anterior deirid neurons (ADEs) and 4 cephalic sensilla neurons (CEPs), each with a dendritic projection extending to the mouth of the animal. The posterior dopaminergic neurons are termed posterior deirid neurons (PDEs, Figure 20). The dopaminergic neurons in *C. elegans* serve mechanosensory functions, distinguishing textures and detecting food sources. In response to changes in environmental food availability, the nematode exhibits a food-induced slowing response[260].

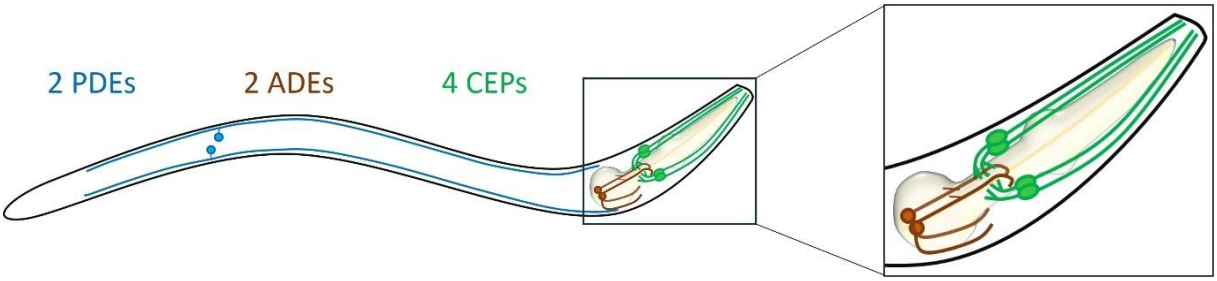

Figure 20: Dopaminergic system of *C. elegans*. The position of the eight dopaminergic neurons of *C. elegans* is displayed. They include 4 cephalic sensilla neurons (CEPs), 2 anterior deirid neurons (ADEs), and 2 posterior deirid neurons (PDEs).

Expression of aSyn in all neurons or specific populations leads to the loss of dopaminergic neurons, deficits in dopamine-dependent behaviors, and a reduction in dopamine levels[261]. This model enables the examination not only of the loss of neuronal dopaminergic cells but also more subtle phenotypes such as axonal and dendritic blebbing, broken dendrites, disappearance of axons, and retreat of dendritic terminals[262–264].

1.4 Aims of this Study

Despite more than two centuries of medical recognition since James Parkinson's initial description in 1817, PD remains a challenging condition to comprehend and treat effectively. Up to now, medical interventions primarily address symptom management rather than the fundamental causes of the disease. The multifactorial

nature of PD, possibly involving multiple causative factors, complicates its understanding and therapeutic development. To achieve a breakthrough in PD treatment by addressing its root causes, an imperative need exists for intensified basic research elucidating the mechanisms underlying neurodegeneration.

One significant contributing factor to PD is associated with the protein aSyn. Mutations or PTMs in aSyn contribute to aggregation, cell-to-cell propagation, neurodegeneration and subsequent neurological cell death. Understanding the mediated toxicity has been a focus of research, with recent attention directed toward PTMs due to their demonstrated impact on aSyn aggregation.

Moreover, the identification of residue 39 in aSyn as a pivotal site has emerged. Positioned centrally in the linker between two helices formed upon membrane interaction, alterations at this residue influence aggregation and membrane affinity. Notably, tyrosine at position 39 gets phosphorylated by c-abl, a modification prevalent in the brains of advanced-stage PD patients, coupled with elevated c-abl activation. Evidence suggests a positive feedback loop, as aSyn overexpression in the rat midbrain induces c-abl expression[247]. To facilitate investigations, phosphomimetic mutations such as aspartate or glutamate are commonly used in research[265]. In this study, in order to shine light on the phosphorylation at position 39 of aSyn, tyrosine was mutated to glutamate, a phosphomimetic mutation that has proven in various proteins to imitate many features of protein phosphorylation[266,267]. The phosphomimetic mutant Y39E aSyn was characterized including a biophysical understanding of Y39E aSyn regarding the following:

a. Understanding its structure and dynamics as a monomer,
b. Analyzing its interaction with membranes, and
c. Investigating its aggregation profile and kinetics.

Furthermore, the study extends its scope to cellular and *C. elegans* models, aiming to:

d. Compare the aggregation patterns *in vitro* and *in vivo*, and
e. Evaluate the neurodegeneration and toxicity induced by this mutant.

In a last step, the results of this study were compared to data on phosphorylated Y39 (pY39) aSyn to evaluate the use of Y39E as a phosphomimetic mutant.

This multifaceted approach aims to contribute essential insights into the pathogenesis of PD and potentially uncover new avenues for therapeutic intervention regarding aSyn phosphorylation at position 39.

2 Material and Methods

2.1 Molecular Biology

2.1.1 Site-directed Mutagenesis PCR

To introduce mutations within the aSyn protein, the QuikChange II Site-Directed Mutagenesis Kit (Agilent) was employed. The pT7-7 plasmid, which encodes WT aSyn, was generously provided by Claudio Fernández. Stefan Becker (Department of NMR-based Structural Biology, Max-Planck Institute for Multidisciplinary Science, Göttingen, Germany) kindly provided the pT7-7 plasmid containing Y39E aSyn. Mutagenesis primer (Table 2) were utilized in polymerase chain reactions (PCRs), using WT or Y39E aSyn as template to generate the (double) mutants A18C, A90C, A18C/Y39E, and Y39E/A90C.

Table 2. Mutagenesis primer for PCR reaction. The sequence of forward and reverse primer to introduce A18C or A90C mutations are stated.

Mutation	Primer	Sequence
A18C	Forward	5’-GAGGGAGTTGTGGCTTGTGCTGAGAAAACCAAA-3’
	Reverse	5’-TTTGGTTTTCTCAGCACAAGCCACAACTCCCTC-3’
A90C	Forward	5’-GCAGGGAGCATTGCATGTGCCACTGGCTTTGTC-3’
	Reverse	5’-GACAAAGCCAGTGGCACATGCAATGCTCCCTGC-3’

In a nutshell, 1 µl of template DNA was incubated with 5 µl of reaction buffer, 1 µl of deoxynucleotide triphosphate (dNTPs), 125 ng of each primer, and 1 µl of PfuUltra

High-Fidelity DNA Polymerase in a final volume of 50 µl. The PCR program (Table 3) was executed using a MyCycler Thermal Cycler (Bio-Rad).

Table 3: PCR program for amplifying aSyn. The temperature and time of each step of the mutagenesis PCR is displayed along with the number of repetitions.

Step	Temperature [°C]	Time [min]	Cycle repetition
Denaturation	95	1	
Denaturation	95	0.5	x 16
Primer annealing	55	1	
Extension	68	4	
Extension	68	5	
Hold	4	99	

To eliminate the dam-methylated template DNA, the PCR product was incubated 1 hour at 37 °C, 250 rpm with 1 µl of DpnI. Subsequently, the digested linear PCR products were transformed into JM109 *Escherichia coli* (*E. coli*). JM109 circulates the plasmid and achieves ampicillin resistance encoded on the pT7-7 plasmid. The circulated plasmids were extracted, sequenced, and transformed into BL21 (DE3) *E. coli* for subsequent protein expression and purification.

2.1.2 Transformation of *E. coli* and Preparation of Glycerol Stock

Competent *E. coli* JM109 or BL21 (DE3) strains were prepared for transformation through calcium and temperature treatment. BL21 (DE3) *E. coli* carried the NatB plasmid (pACYCduet-naa20-naa25, a gift from Markus Zweckstetter (Department of Translational Structural Biology, German Center for Neurodegenerative Diseases, Göttingen, Germany)) encoding the NatB acetylase complex of

Schizosaccharomyces pombe, ensuring N-terminal acetylation during aSyn expression. Additionally, the NatB plasmid conferred resistance to chloramphenicol, while the pT7-7 plasmid contained an ampicillin resistance gene, serving as selection markers for successful bacterial transformation.

To initiate from a single clone, JM109 or BL21 (DE3) cells were streaked from glycerol stocks onto Luria-Bertani agar (LBa, 10 g/l NaCl, 10 g/l tryptone, 5 g/l yeast extract, 15 g/l agar) plates without antibiotics (JM109) or supplemented with 25 µg/ml chloramphenicol (CHL, BL21 (DE3)), followed by an overnight incubation at 37 °C. Single colonies were inoculated into 2 ml of Luria-Bertani medium (LBm, 10 g/l NaCl, 10 g/l tryptone, 5 g/l yeast extract), without antibiotics or with CHL and grown overnight at 37 °C, 250 rpm.

The following day, 1 ml of the overnight culture was diluted in 99 ml LBm (without antibiotics or with CHL) and incubated at 37 °C for 1 hour, allowing the bacteria to enter the exponential growth phase. A 1 ml aliquot for each transformation reaction was centrifuged (4000 rpm, 2 min, 4 °C), and the resulting pellet was resuspended in 500 µl prechilled $CaCl_2$ (0.1 M). After a second centrifugation, the pellet was resuspended in 100 µl $CaCl_2$. 1 µl of plasmid (DpnI digested, linear PCR product for JM109, or pT7-7 circular plasmid for BL21 (DE3)) was added to the competent cells and incubated on ice for 1 hour. A heat shock at 45 °C for 90 sec facilitated DNA uptake. After incubating on ice for 2 min, 900 µl LBm was added. For plasmid circulation and antibiotic resistance expression, bacteria were incubated for 1 hour at 37 °C, 250 rpm. Following centrifugation (5000 rpm, 2 min), the cell pellet was resuspended in 100 µl LBm to reduce the total volume. The cell suspension was plated on LBa plates, supplemented with ampicillin (AMP, 0.1 mg/ml) and CHL for BL21 (DE3), and incubated overnight at 37 °C. Inoculations of 2-6 ml LBm, containing AMP (JM109, BL21 (DE3)) and CHL (BL21 (DE3)), were performed with single colonies and incubated overnight at 37 °C, 250 rpm. The next day, 500 µl of the cell suspension was diluted in 500 µl of a 50% glycerol solution diluted in H_2O and immediately frozen in cryopreservation vials at -80 °C.

2.1.2.1 Plasmid Isolation and Sequencing

For the isolation of circulated plasmids from JM109 bacterial cells, 5 ml of the overnight culture used to create a glycerol stock was utilized. The PureLink Quick Plasmid Miniprep Kit (Invitrogen) was employed following the manufacturer's instructions. In brief, cells were harvested by centrifugation and resuspended in 250 µl resuspension buffer. After a 5-min lysis to release cellular contents, DNA was precipitated for 10 min (250 µl lysis and 350 µl precipitation buffer). The resulting supernatant was applied to Miniprep columns placed in collection tubes. DNA bound to the membrane was washed with wash buffer (500 µl W10 and 700 µl W9) before drying the membrane by centrifugation. Plasmid DNA elution was performed in 50 µl H_2O, preheated at 60 °C. DNA concentration and quality were assessed by measuring absorbance at 230, 260, and 280 nm, using the spectrophotometer V-630 (JASCO). The A260/A280 ratio, indicating protein contamination, aimed to be between 1.7 and 2, while A260/A230, signaling potential ethanol or salt contamination, should be around 2. DNA concentration was calculated using the equation $c\left[\frac{ng}{\mu l}\right] = \frac{A230 * 50}{0.3} * 20$, considering a dilution factor of 20.

To ensure purity, clones without contaminations were sequenced using Capillary Electrophoresis Sequencing (CES) by MACROGEN CO., LTD, with the primers listed in Table 4.

Table 4: Sequencing primers. The nucleotide sequence of primers used for capillary electrophoresis sequencing by Macrogen are demonstrated.

Primer	Sequence
Seq REV	5’-AATTCTCATGTTTGACAGC-3’
T7 promoter	5’-TAATACGACTCACTATAGGG-3’

Sequenced plasmids were subsequently transformed into BL21 (DE3) *E. coli*, following the protocol outlined in section 2.1.2.

2.1.3 Protein Expression and Purification

The process of expressing and purifying recombinant, N-terminal acetylated aSyn variants (WT, A18C, A90C, Y39E, A18C/Y39E, and Y39E/A90C) involved inducing protein expression with isopropyl-1-thio-β-D-galactopyranoside (IPTG). This was followed by cell lysis, protein precipitation, high-pressure liquid chromatography (HPLC) purification, and subsequent dialysis.

Bacterial glycerol stocks of BL21 (DE3) *E. coli*, containing pNatB and pT7-7 aSyn, were utilized to inoculate 5 x 5 ml LBm with AMP and CHL and incubated overnight at 37 °C, 250 rpm. The precultures where then combined and diluted either in 275 ml LBm with AMP and CHL for ^{15}N-labeled expression, or in 275 ml Terrific Broth medium (Table 5) with AMP and CHL for non-labeled expression. Bacteria were allowed to grow at 37 °C, 250 rpm until reaching an OD_{600} of 4 for non-labeled expression. At this point, protein expression was induced by adding 1 mM IPTG for 2 hours to the cell suspension. Bacteria were then collected by centrifugation at 4000 rpm for 15 min at 4 ºC and stored at -20 °C. For ^{15}N-labeled protein expression, at an OD_{6000} value of 3-4, bacteria were centrifuged at 2500 g, 5 min, and the pellet was resuspend in 250 ml Minimal medium (Table 5). Once the OD_{600} value increased by one unit or after a maximum of 1.5 hours of incubation time at 37 °C and 250 rpm, IPTG induction occurred (1 mM) for 2 hours. Cells were harvested as for non-labeled protein expression.

To ensure quality control throughout the process, aliquots have been taken before (pre-IPTG) and after (post-IPTG) IPTG induction for both ^{15}N-labeled and non-labeled protein expression.

Table 5: Composition of Terrific Broth and Minimal medium. The components and their final concentrations are stated for both media.

Terrific Broth medium		**Minimal medium**	
Yeast extract	12 g/l	**Na_2HPO_4**	60.5 mM
Tryptone	6 g/l	**KH_2PO_4**	22.0 mM

Terrific Broth medium		**Minimal medium**	
Glycerol	5.5 g/l	**NaCl**	8.6 mM
Glucose	0.5%	**$MgSO_4$**	5.0 mM
$MgSO_4$	2.0 mM	**Glucose**	1%
$(NH_4)_2SO_4$	25.0 mM	**$^{15}NH_4Cl$**	1 g/l
KH_2PO_4/Na_2HPO_4	50.0 mM	**Trace elements (1000x)**	1x
AMP	0.1 mg/ml	**CaCl2 100 mM**	0.2 mM
CHL	25 µg/ml	**AMP**	0.1 mg/ml
		CHL	25 µg/ml

Trace elements stock solution contained 0.134 mM ethylenediaminetetraacetic acid (EDTA), 0.077 mM $ZnSO_4$ • 7 H_2O, 0.184 mM H_3BO_3, 0.026 mM $MnCl_2$ • 4 H_2O, 0.018 mM $FeSO_4$ • 7 H_2O, 0.007 mM $CoCl_2$ • 6 H_2O, 0.005 mM $CuSO_4$ • 5 H_2O, and 0.0008 mM $(NH_4)_6Mo_7O_{24}$ • 4 H2O.

Cell lysis involved resuspending the pellet in 20 ml lysis buffer (10 mM Tris, 1 mM EDTA, pH 8), supplemented with 1 mM of serine protease inhibitor phenylmethyl-sulfonyl fluoride (PMSF). Subsequently, the cells were sonicated on ice using a 250 Branson Sonifier at a frequency of 20 Hz for 30 sec on, 2 min off, 10 times, and then boiled at 95 °C for 20 min. To remove cell debris, samples were centrifuged at 11 000 rpm for 40 min at 4 ºC. An aliquot of the supernatant was collected for quality control (Ctr1) before incubating the supernatant for 30 min at 4 °C with 50 rpm agitation, along with 0.01 g/ml streptomycin sulfate to precipitate DNA. After centrifugation (11 000 rpm for 40 min at 4 ºC) and collection of another aliquot for quality control (Ctr2), aSyn was precipitated by salted out. The supernatant was incubated with 0.361 g/ml ammonium sulfate for 30 min at 4 °C with 50 rpm agitation, and precipitated proteins were collected by centrifugation (11 000 rpm for 40 min at 4 ºC) and resuspended in 5 ml buffer Tris (25 mM, pH 8). An aliquot was collected

(Ctr3), and the protein concentrate was dialyzed overnight at 4 °C against the same buffer to ensure desalting.

The following day, samples were centrifuged (10 000 rpm for 10 min at 4 °C) and sterile filtered through 0.22 µM pores. The protein solution was purified using an ÄKTA Pure chromatography system (Cytiva) equipped with a HiTrap Q HP anion exchange chromatography column (GE Healthcare). A linear salt gradient was used to elute aSyn from the column, titrating Tris buffer (25 mM Tris, pH 8, 0.22 µm filtered and degassed) with high-salt Tris buffer (25 mM Tris, 1 M NaCl, pH 8, 0.22 µm filtered and degassed). At a concentration of approximately 300 mM NaCl, aSyn elutes. The fractions surrounding the peak corresponding to aSyn were analyzed with sodium dodecyl-sulfate polyacrylamide gel electrophoresis (SDS-PAGE) based on their aSyn content. Fractions containing a sufficient amount of aSyn were combined and dialyzed overnight at 4 °C against 1 l of buffer MES (20 mM MES, 100 Mm NaCl, pH 6.5).

The protein solution was recovered, and the concentration was determined by measuring the absorbance at 274 nm using a quartz cuvette (100 µl) and an optical path of 0.3 cm. For WT aSyn, an extinction coefficient of 1680 M^{-1} cm^{-1} was applied, while for Y39E, due to the removal of one aromatic side chain, a coefficient of 1260 M^{-1} cm^{-1} was used. The protein was aliquoted and stored at -80 °C until its usage.

To prevent dimerization of A18C, A90C, A18C/Y39E and Y39E/A90C aSyn by cysteine bridges during the purification process 1 mM dithiothreitol (DTT) was added to all solutions.

2.1.3.1 SDS-PAGE

For quality control purposes, samples obtained at various stages of the purification process, as well as fractions of the eluted aSyn post-HPLC purification, underwent analysis by SDS-PAGE. The supernatant from pre- and post-IPTG samples (pelleted for 3 min at 5000 rpm), along with the samples Ctr1, Ctr2, and Ctr3 were supplemented with 5x Lämmli buffer (250 mM Tris pH 6.8, 10% SDS, 1.25% bromophenol blue, 5% β-mercaptoethanol, 50% glycerol)[268]. These samples were then boiled for 10 min at 98 °C and centrifuged for 3 min at maximum speed.

Separation was conducted on 12% separating / 4% stacking SDS-polyacrylamide gels, see Table 6 for composition. Protein separation occurred in a running buffer (1.9 mM glycine, 0.25 mM Tris, 0.035 mM SDS) at 90 V using a Mini-PROTEAN Tetra Vertical Electrophoresis Cell (Bio-Rad).

Table 6: Composition of SDS-polyacrylamide gel. The ingredients for separating and stacking SDS-polyacrylamide gel are specified. Ammonium persulfate (APS), tetramethylethylenediamine (TEMED).

	12% separating gel	**4% stacking gel**
(Bis)-acrylamide (1% / 29%)	50%	16.25%
Tris 1.5 M, pH 8.8	25.3%	
Tris 1 M, pH 6.8		12.5%
SDS 10%	1.3%	1%
APS 10%	1.3%	1%
TEMED	0.053%	0.1%

Following protein separation, Coomassie staining was employed for protein visualization. SDS-polyacrylamide gels were boiled in solution A (0.5 g/l Coomassie-R, 10% acetic acid, 25% isopropanol) and incubated with agitation for 10 min. Subsequently, gels were transferred to solutions B (0.05 g/l Coomassie-R, 10% acetic acid, 10% isopropanol), C (0.02 g/l Coomassie-R, 10% acetic acid), and D (10% acetic acid), each time briefly boiled. To enhance gel destaining, it was kept overnight in solution D with agitation. Figure 21 illustrates a representative SDS-polyacrylamide gel featuring purification controls.

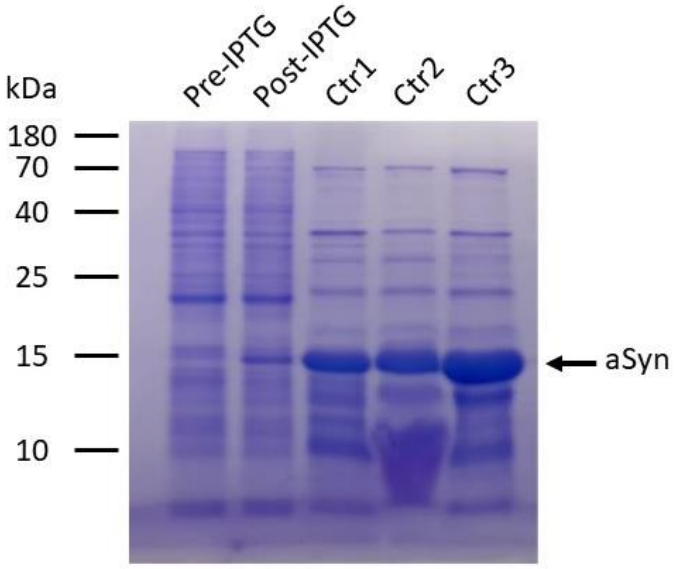

Figure 21: Representative SDS-PAGE displaying purification controls. Coomassie-stained SDS-PAGE of control samples collected during protein expression and purification, separated on 12% SDS-PAGE.

SDS-PAGE was additionally performed with monomers of aSyn and the final product of aggregation monitored by NMR or ThT fluorescence. Upon reaching a plateau phase in the aggregation process, ThT triplicates were combined, and sample underwent centrifugation at 21 000 g for 1 hour at 4 °C. The resulting supernatant was isolated, and the pellet was resuspended in an equivalent volume of buffer MES. Subsequently, 20 µl of both supernatant and pellet were combined with 5 µl of Lämmli buffer, boiled, loaded, and separated as outlined for purification control samples.

2.1.4 Paramagnetic Relaxation Enhancement (PRE): The Probe MTSL

Paramagnetic relaxation enhancement (PRE) constitutes a nuclear magnetic resonance (NMR)-based technique for investigating transient long-range protein interactions. To facilitate this, point mutations to cysteine were introduced at positions 18 and 90 of aSyn (resulting in A18C and A90C aSyn). Subsequently, the paramagnetic probe, 1-Acetoxy-2,2,5,5-tetramethyl-δ-3-pyrroline-3-methyl (MTSL), was covalently attached to these positions by disulfide bridges. Selectivity was

achieved by the fact, that aSyn lacks further cysteine residues. The use of MTSL in combination with the mutants A18C and A90C of aSyn has been extensively studied[238,269,270].

For the covalent binding of MTSL to A18C, A90C, A18C/Y39E, or Y39E/A90C aSyn, DTT, present during purification to shield cysteine groups from chemical interactions, was extracted through overnight dialysis at 4 °C in DTT-free buffer MES. MTSL, dissolved in acetone, was then incubated with the freshly dialyzed protein in a 5:1 ratio overnight at 4 °C in the dark. To remove excess MTSL, another round of dialysis was performed overnight at 4 °C in buffer MES. Subsequently protein concentration was adjusted to 100 µM and PRE-NMR experiments were conducted.

2.1.5 Preparation of SUVs

To simulate SVs, small unilamellar vesicles (SUVs) composed of 1,2-di-(9Z-octadecenoyl)-sn-glycero-3-phosphoethanolamine (DOPE), 1,2-di-(9Z-octadecenoyl)-sn-glycero-3-phospho-L-serine (DOPS), and 1,2-di-(9Z-octadecenoyl)-sn-glycero-3-phosphocholine (DOPC) were prepared. DOPE:DOPS:DOPC were used in a 5:3:2 ratio in titration experiments using circular dichroism (CD) spectroscopy, while a 5:2:12 ratio served in NMR experiments.

A glass tube, washed with chloroform, was used to prepare the SUVs. Coagulation Reagent I (Avanti), comprising DOPE:DOPS:DOPC (5:3:2) in chloroform, or combined 1:1 with 18:1 (Δ9-Cis) PC (DOPC, Avanti) in chloroform to achieve the 5:3:12 ratio, was briefly vortexed and slowly evaporated under nitrogen gas, forming a thin, homogeneous lipid layer on the glass surface. Covered with aluminum foil, the samples were lyophilized overnight using a Lyoquest-55 (Azbil Telstar Technologies S.L.U.).

On the following day, to achieve a lipid concentration of 7 mM, 2 ml of buffer MES were added to the glass tube and incubated for 15 min at 35 °C in a water bath to hydrate the lipids, with brief vortexing every 3 min. SUVs were then sonicated on ice 10 times for 2 min each, with 2 min rest intervals. After centrifugation for 5 sec at 10 000 g, the supernatant was utilized to measure the size of the SUVs through dynamic light scattering (DLS) on a Zetasizer Nano ZS (Malvern). If the diameter

exceeded 80 nm in diameter, sonication was repeated until the desired SUV size was reached.

2.2 Biophysical Methods

2.2.1 ThT Fluorescence

To identify amyloid fibrils of aSyn, the fluorescent probe ThT was employed. ThT undergoes changes in its absorption and emission spectra upon binding to cross β-sheet-rich fibrils[186]. At the initial and final stage of aSyn aggregation, 5 µl of the sample was diluted in 95 µl of buffer MES, supplemented with 20 µM ThT. The excitation wavelength was set to 446 nm, while fluorescence was detected between 470 nm and 600 nm using a fluorescence spectrophotometer (Cary Eclipse, Varian).

Moreover, to monitor fibril formation during the aggregation process, aggregation experiments were conducted in triplicates using microplates in the presence of ThT and an POLARstar OMEGA (BMG Labtech) plate reader. In 96-well plates supplemented with beads, 50, 100, or 200 µM of aSyn in buffer MES with 5 µM ThT and 0.01% NaN_3 (to prevent contamination) in a total volume of 150 µl were incubated at 37 °C with 300 rpm agitation every 10 min. ThT was excited at a wavelength of 440 nm, and the fluorescence emission was detected at 480 nm after each agitation step.

The kinetics of the aggregation were analyzed by normalizing the emission spectra to their highest values within the replicates. The resulting sigmoidal curves of normalized fluorescence against the time of aggregation were fitted to Equation 1 to estimate the half time of the aggregation process and the elongation factor.

$$y(t) = \frac{1 - e^{-a*t}}{1 + e^{-a*(t-t_{1/2})}} \qquad \text{Equation 1}$$

Here, *y(t)* represents the fraction of fibrils present at a given time point *t*, while $t_{1/2}$ indicates the half time of the completed aggregation process. The process is considered complete if the ThT fluorescence reaches its plateau phase. *a* is the elongation factor, referring to the speed of fibril elongation.

The elongation factor *a* and the half time $t_{1/2}$ depend on the initial protein concentration *[P]*, the velocity of the incorporation of monomers into aggregating nuclei (expressed by the constant k_M), the concentration of aggregating nuclei in the sample *[N]*, and the fraction of interaction sites on pre-existing aggregates where aSyn monomers can incorporate (I_S). The relations between these parameters are stated in Equation 2 and 3.

$$a = [P] * k_M * I_S \qquad \text{Equation 2}$$

$$t_{1/2} = \frac{ln\left(\frac{I_S * [P]}{[N]}\right)}{a} \qquad \text{Equation 3}$$

2.2.2 CD Spectroscopy

CD spectroscopy is used to analyze the secondary structure of a protein by taking advantage of the chiral nature of proteins that can rotate the plane of polarized light. Amino acids exist as two mirrored enantiomers, namely L or D amino acids, which rotate polarized light differently. In CD spectroscopy, a beam of polarized circular light, rotating clockwise (right circular polarization) and then anti-clockwise (left circular polarization), is passed through the sample. Chiral amino acids in the protein alter the plane of the polarized circular light, with distinct alterations of rotations for right and left circular polarization due to the prevalence of L-amino acids. The output data, often presented as the degree of ellipticity, relates to the detection of ellipses instead of a round circle of light upon changing the polarized light. When plotted against the excitation wavelength, these degree of ellipticity profiles can reveal typical spectra for pure secondary structures of a protein. α-helical structures typically show two minima at 222 and 208 nm and one maximum at 193 nm. β-sheet structures

exhibit one minimum at 218 nm and one maximum at 195 nm, whereas proteins with disordered secondary structures are represented by one minimum at 195 nm[271] (Figure 22). Since proteins usually feature more than one kind of secondary structure, the resulting CD spectra are typically overlays of different pure secondary structure profiles.

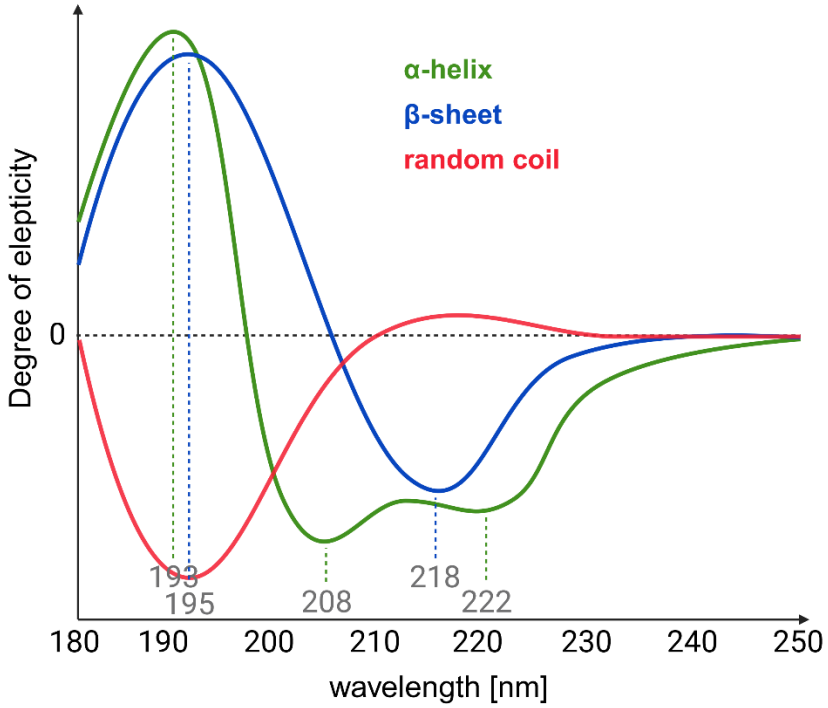

Figure 22: CD spectra of pure secondary structures in proteins. The degree of ellipticity is plotted against the wavelength. The resulting spectra for pure α-helices, β-sheets or random coil structures are displayed.

2.2.2.1 Characterization of the Final Product of Aggregation

To investigate the final product of aggregation, separated into supernatant and pellet as described in section 2.1.3.1 for SDS-PAGE, and samples containing aSyn monomers, CD spectroscopy was employed. The samples consisted of 48 µl aSyn (monomers, supernatant or pellet) and 192 µl H_2O. CD spectra were recorded in triplicates on a J-1500 CD spectrometer (JASCO) from 190 nm to 250 nm at 25 °C. The spectra were baseline-corrected against buffer MES and smoothed (Savitzky–Golay filter).

2.2.2.2 Membrane Binding Titration Experiments

CD spectra of aSyn monomers and subsequently increasing concentrations of SUVs were recorded. For SUVs composed of DOPE:DOPS:DOPC (5:3:2), 10 µM aSyn was used along with 5, 10, 20, 40, 60, 80, 100, 125, 150, 200, 250 and 300 equivalents of SUVs in a total volume of 250 µl. Spectra acquisition and data processing were done as described above. For Y39E, two replications were performed.

The degree of ellipticity at 222 nm wavelength was then plotted against the SUV concentration. The resulting curves were fitted to Equation 4 to estimate the dissociation constant K_d and the average number of lipids aSyn is interacting with (*L*).

Equation 4

$$f = (b) - ((b - c) * \left(\frac{a + \frac{abs(x)}{L} + K_d}{2 * a} - \left(\frac{\sqrt{\left(a + \frac{abs(x)}{L} + K_d\right)^2 - \left(4 * a * \frac{abs(x)}{L}\right)}}{2 * a} \right) \right)$$

where:

a: aSyn concentration [µM]

b: minimum degree of ellipticity at 22 nm

c: maximum degree of ellipticity at 22 nm

L: average number of lipids interacting with aSyn

x: lipid concentration [µM]

K_d: dissociation constant

2.2.3 Size Exclusion Chromatography

Size exclusion chromatography (SEC) serves as a method for separating molecules based on their size by passing the sample through a gel containing spherical beads

with pores of specific sizes. Small molecules infiltrate more fine pores of the matrix, extending their path length to traverse the column. Consequently, molecules are eluted based on their size, with larger ones, such as soluble aSyn oligomers, appearing in earlier fractions, while smaller molecules, like monomers, are eluted in later fractions.

SEC was conducted using an ÄKTA Pure (Cytiva) equipped with a superdex 200 (10/300 GL) column (GE Healthcare). Following column washing, 200 µl of the supernatant from aggregation experiments monitored by ThT fluorescence (supernatant separated as described for analysis of the final product through SDS-PAGE in section 2.1.3.1), or monomers of WT and Y39E aSyn, were applied to the column. Elution was carried out using buffer MES.

2.2.4 NMR Spectroscopy

NMR spectra were acquired using a Bruker Ascent 600 MHz spectrometer, equipped with a PA TXI 600 S3 H-C/N-D-05 Z probe, with all measurements conducted at 15 °C. The samples, consisting of aSyn in buffer MES with 10% D_2O, were processed using TopSpin Version 3.5 (Bruker) and analyzed using CCPNMR 2.4.2[272]. The backbone assignment of ^{15}N-labelled aSyn was kindly provided by Claudio Fernández.

2.2.4.1 Aggregation Assay

Aggregation was induced by incubating 50 µM of either WT or Y39E aSyn, dissolved in 10% deuterated buffer MES, within 5 mm NMR tubes at 37 °C under constant magnetic stirring (500 rpm). To monitor aSyn aggregation through NMR experiments, daily acquisition of conventional 1D ^1H spectra was performed using the "zgesgp" pulse program. Additional details regarding the pulse program and acquisition parameters are available in the Appendix. The decay of protein signals was assessed by integrating the signal within the 0.8-0.6 parts per million (ppm) range. This decay is directly correlated with the quantity of monomers present in the sample, as aggregated aSyn, due to its size, remains undetectable in liquid-phase NMR

experiments. Consequently, the reduction in signal intensity reflects the percentage of monomers remaining in the sample. Data of four different aggregation experiments was collected for each, WT and Y39E aSyn.

2.2.4.2 2D ^{1}H-^{15}N HSQC

Two-dimensional HSQC experiments were employed to investigate the structural properties of aSyn monomers. These heteronuclear experiments correlate the chemical shifts of protons (^{1}H) with the chemical shifts of a covalently bound nucleus, specifically ^{15}N in this case. The pulse sequence involves transferring magnetization between different nuclei to create a correlation spectrum. Initially, amide protons of aSyn are excited, and their magnetization is transferred to the directly bound ^{15}N nucleus through a series of pulses in a module known as insensitive nuclei enhanced polarization transfer (INEPT). During the evolution period (t_1), the heteronuclear coherence is labeled with the chemical shift of the heteronucleus. Subsequently, magnetization is transferred back to the protons (reverse-INEPT), and the resulting signal is detected based on the chemical shift of protons during t_2.

During protein expression, ^{15}N-labeled nitrogen served as the exclusive source of nitrogen, leading to the incorporation of ^{15}N into amino acids of aSyn. Each amino acid in the protein sequence features one amide group, encompassing the ^{15}N-labeled nitrogen atom. Every resulting cross peak in the HSQC spectra corresponds to a specific pair of amide proton (^{1}H) and heteronucleus (^{15}N), representing a distinct amino acid of aSyn in the protein sequence. The intensities and location of cross peaks are influenced by its chemical environment; therefore, changes in the protein's structure can be monitored by changes in the intensities and/or chemical shifts of cross peaks.

HSQC experiments in this study were performed on 100 µM WT or Y39E ^{15}N-labelled aSyn samples, using the pulse program "hsqcfpf3gpphwg," detailed in the Appendix. Chemical shift perturbations between WT and Y39E aSyn were calculated using the Equation 5:

$$\Delta ppm = \sqrt{(\Delta\delta^{1}H)^{2} + (\Delta\delta^{15}N)^{2}} \qquad \text{Equation 5}$$

2.2.4.3 PRE-NMR Experiments with MTSL

In PRE-NMR experiments, the paramagnetic probe MTSL was introduced at positions 18 or 90, as detailed in section 2.1.4. HSQC spectra were acquired using 100 µM A18C, A90C, A18C/Y39E, or Y39E/A90C ^{15}N-labeled aSyn in the presence and absence of MTSL incorporation.

The paramagnetic character of the probe is due to the presence of a chemical radical within MTSL. This unpaired electron can interact magnetically with protons in a radius of up to 20-25 Å. The strength of the paramagnetic character is thereby proportional to the distance between the unpaired electron and the proton. Amide protons close in primary sequence or in space interacting with the paramagnetic probe, show reduced signal intensity of cross peaks of the corresponding residue in the HSQC spectra. The signal intensities of cross peaks from HSQC spectra acquired in absence (I_0) and in presence (I) of MTSL were calculated. To obtain an intensity profile of the protein that is representative of the network of transient long-range interaction in aSyn, the ratio I/I_0 was plotted against the primary sequence of aSyn. For A18C/Y39E and Y39E/A90C two replicates were analyzed.

2.2.4.4 Membrane Binding Characterization

To assess the binding of aSyn to membranes in a residue-specific manner, HSQC spectra of 100 µM WT or Y39E aSyn in the absence and presence of 2500 µM DOPE:DOPS:DOPC (5:3:12) SUVs were recorded and analyzed. Amino acids interacting with the membrane adopt secondary structure elements, lose their flexibility and show a decrease in signal intensity of cross peaks. The signal intensities of HSQC spectra acquired in the presence of SUVs (I) were divided by the signal intensities of the respective cross peaks of HSQC spectra acquired in the absence of SUVs (I_0). The calculated I/I_0 ratio was then plotted against the amino acid sequence of aSyn, resulting in a residue-specific interaction profile of aSyn with the SUVs.

Amino acids 1-25 of aSyn play a pivotal role in membrane binding, adopting an α-helical structure upon interaction with membranes[273]. This strong interaction of the N-terminus of membrane-bound aSyn with the membrane leads to a signal intensity

reduction of NMR signals beyond the detection limit. The total bound population of aSyn molecules is therefore directly proportional to the mean peak intensity ratios (I/I_0) of the amino acids 3-25 ($(I/I_0)_{mean,3\text{-}25}$), and was calculated as $1\text{-}(I/I_0)_{mean,3\text{-}25}$. The NAC region of aSyn is not as tightly associated with membranes as the N-terminal region. It has membrane-sensing properties and can bind to membranes either in a hidden (associated) or in an exposed (dissociated) conformation. The peak intensity rations of amino acids 66-80 were considered to calculate the population of membrane-bound aSyn molecules in an associated and dissociated conformation. The tighter this region binds to the membrane, the stronger decreases the corresponding cross peak signal intensities observed in the HSQC spectra. The population of membrane-bound aSyn binding in an associated conformation was calculated as $1\text{-}(I/I_0)_{mean,66\text{-}80,}$ while the population of membrane-bound aSyn in a dissociated state was determined by subtracting the hidden from the total bound population[219].

2.2.4.5 Relaxation Rate Measurements

Longitudinal and transversal relaxation rates provide residue-specific insights into the structure and dynamics of proteins. The longitudinal relaxation time T_1 describes the time required for nuclear spins to return to their equilibrium along the direction of the external magnetic field M_z (longitudinal direction) after perturbation. R_1, reflecting the exponential decay of magnetization along this direction, is related to T_1 and M_z through the Equations 6 and 7:

$$R_1 = \frac{1}{T_1} \qquad \text{Equation 6}$$

where:

R_1: longitudinal relaxation rate [Hz]

T_1: longitudinal relaxation time [sec]

$$M_z = M_0 * (1 - e^{-R_1 * t}) \qquad \text{Equation 7}$$

where:

M_z: external magnetic field

M_0: equilibrium magnetization of nuclear spins

t: delay time [sec]

Similarly, the transversal relaxation rate R_2, related to the transversal relaxation time T_2, was determined. After a 90-degree pulse, nuclear spins process in the transverse (x-y) plane, creating transverse magnetization. R_2 characterizes the decay of the magnetization in the x-y plane due to various interactions causing dephasing, and it is related to T_2 and M_{xy} as follows:

$$R_2 = \frac{1}{T_2}$$ Equation 8

where:

R_2: transversal relaxation rate [Hz]

T_2: transversal relaxation time [sec]

$$M_{xy} = M_0 * e^{\frac{-R_2}{t}}$$ Equation 9

where:

M_{xy}: transversal magnetization

M_0: equilibrium magnetization of nuclear spins

t: delay time [sec]

The relaxation rates R_1 and R_2 are providing information regarding dynamical properties of the protein. Dynamic processes and fluctuations occurring in a time scale of picosec to milisec can be detected, including fluctuations in protein folding, the exchange with the solvent and chemical exchange within the protein. R_1 values are sensitive to pico- to nanosec time scale motions, while R_2 values are sensitive to conformational transitions occurring at a micro- to milisec time scale.

To determine the relaxation rates R_1 and R_2 of the ^{15}N nuclei, spectra of 200 µM aSyn with different delay times (R_1: between 0.05-1.600 sec, R_2: 0.064-0.8 sec) were recorded, peaks were assigned, and intensity changes over time were fitted to a two-parameter exponential decay function to obtain sequence-specific R_1 and R_2 rates.

Detailed pulse programs and acquisition parameters are provided in the Appendix. For WT aSyn, one repetition for each relaxation rate was conducted, while for Y39E aSyn two repetitions of R_1 measurements and 3 repetitions of R_2 measurements were performed.

2.2.4.6 $^3J_{HN\text{-}H\alpha}$ Coupling

The ^3J coupling constants is influenced by the torsional angles (dihedral angles) within the peptide backbone. The protein backbone exhibits rotation around two principal torsional angles: the Φ (phi) angle and the Ψ (psi) angle. These angles describe the orientation of consecutive peptide planes and significantly impact the overall protein structure. The peptide bond itself, characterized by the omega (ω) angle, remains fixed at 180 °C, defining the peptide plane. The $^3J_{HN\text{-}H\alpha}$ coupling constants between neighboring protons in the backbone are particularly sensitive to the dihedral angle Φ (Figure 23).

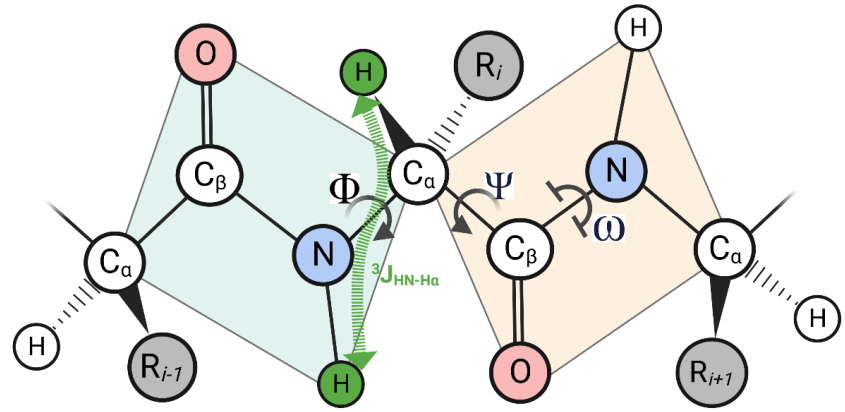

Figure 23: Dihedral angles in peptides. The peptide plane is depicted and the dihedral angles Φ (phi) and the Ψ (psi), as well as the peptide bond (ω) is indicated. The green arrow indicates the protons determining the $^3J_{HN\text{-}H\alpha}$ coupling constant.

The scalar coupling arises from the interaction of magnetic dipole moments associated with the nuclear spins of two adjacent nuclei, leading to characteristic splitting patterns in the NMR spectrum. A doublet indicates a $^3J_{HN\text{-}H\alpha}$ coupling, where the separation of the doublet peaks defines the $^3J_{HN\text{-}H\alpha}$ coupling constant.

In this study, the $^3J_{HN\text{-}H\alpha}$ coupling constant was determined through NMR experiments. Doublet peaks resulting from this experiment were assigned, the shift

differences of the doublet peaks were calculated and multiplied by the external magnetic field, yielding the $^{3}J_{HN\text{-}H\alpha}$ coupling constant in Hz. The Karplus equation correlates the $^{3}J_{HN\text{-}H\alpha}$ coupling constant with the Φ dihedral angle. For instance, an α-helical structure can only form if the Φ angle is between 50–70 deg or between 105-120 deg (Figure 24). Thus, different coupling values represent specific secondary structures: 3.0-6.0 Hz for α-helical structures, 6.0-8.0 Hz for random coil structures, and 8.0-11.0 Hz for β-sheets[274].

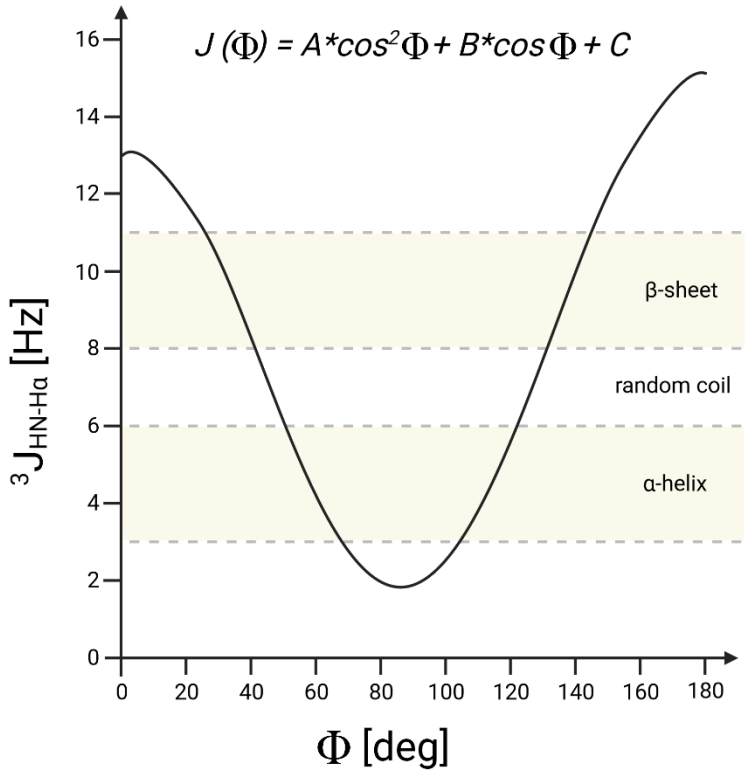

Figure 24: Graphical demonstration of the Karplus-equation. The Karplus-equation describes the relation between the dihedral angle Φ and the $^{3}J_{HN\text{-}H\alpha}$ coupling constant.

Two independent experiments were performed, each with 200 µM WT and Y39E aSyn. The detailed pulse program and acquisition parameters are stated in the Appendix.

2.2.4.7 Hydrodynamic Radius

The hydrodynamic radius (R_H) of aSyn was determined through pulse-field gradient NMR. This technique utilizes the diffusional movement of molecules in a magnetic

field to probe their diffusion characteristics. Depending on the viscosity of the solvent, the diffusion characteristics relate to the hydrodynamic radius of the protein in question. Pulse field gradient NMR has been widely used for determining the translational diffusion of molecules in solution and elating it to hydrodynamic properties[275–277]. Hereby, a magnetic field of varying magnitudes in space is applied (dephasing gradient). After a defined time period in which molecules can diffuse within the solvent, a second magnetic field gradient with the same magnitude but opposite algebraic sign is applied (refocusing gradient). This restores the initial state of molecules that did not change position. Molecules that changed their position within the sample tube due to molecular diffusion consequently exhibit a decrease in NMR signal intensity. This relates to the dephasing process that will be partially reversed after the application of the second refocusing gradient. The faster a particular molecule diffuses, the stronger the intensities of its signals will decay in the NMR spectra recorded after the application of the second refocusing gradient. Furthermore, the diffusion rate of a molecule depends on the viscosity of the solution in which it is dissolved. To relate the viscosity to the hydrodynamic radius, the experiments were conducted in the presence of dioxane, a protein which hydrodynamic radius is known.

To prevent interference from NMR signals of the solvent, aSyn was lyophilized overnight and then resuspended in buffer MES prepared in D_2O. Subsequently, 100 mM NaCl and 0.1% dioxane were added to 150 µM aSyn in MES/D_2O. A linear gradient ranging from 2% to 95% was applied, while recording a series of 20 individual PFG-NMR experiments, using different intensities of applied magnetic field gradients. The signal intensities in the aliphatic region of each spectrum (0.8-0.6 ppm) and the signal corresponding to dioxane (approximately 3.6 ppm) were integrated and plotted against the applied gradient intensity to obtain signal decay curves. The curves were fitted to equation 10 to calculate the decay rates of the NMR signal.

$$\mathrm{I(g)} = e^{(-D_r g^2)} \qquad \text{Equation 10}$$

where:

$I(g)$: measured signal intensity

g: gradient

D_r: decay rate of NMR signal

To estimate the hydrodynamic radius of aSyn, the decay rate of the NMR signal intensities of dioxane and aSyn and the hydrodynamic radius of dioxane were related as follows:

$$R_{H,aSyn} = \frac{D_{r,dioxane}}{D_{r,aSyn}} * 2.12 \qquad \text{Equation 11}$$

The experiment was repeated three times, the detailed pulse program and acquisition parameters are outlined in the Appendix.

2.3 Cell-based Methods

2.3.1 Cell Lines and Maintenance

H4 human neuroglioma cells and SH-SY5Y human neuroblastoma cells were cultured in a humidified environment at 37 °C with 5% CO_2. H4 cells were cultivated in Opti-Mem medium (PAN, Germany), supplemented with 10% heat-inactivated fetal bovine serum (FBS) and 1% penicillin-streptomycin. Meanwhile, SH-SY5Y cells were cultured in Dulbecco's Modified Eagle Medium (DMEM, Gibco), complemented with 3.7 g/l sodium bicarbonate, 10% heat-inactivated FBS, and 1% penicillin-streptomycin. Cells were maintained through regular passaging, involving washing with phosphate-buffered saline (PBS, 137 mM NaCl, 2.7 mM KCl, 10 mM Na_2HPO_4, 1.8 mM KH_2PO_4), trypsinization at 37 °C, and subsequent seeding at a 1:10 dilution, conducted twice a week.

2.3.2 Toxicity Assessment by MTT in SH-SY5Y Cells

Thiazolyl Blue Tetrazolium Bromide (MTT, Sigma) is a yellow tetrazolium salt widely employed in colorimetric assays to evaluate cell viability, proliferation, and cytotoxicity. Within living cells, soluble MTT undergoes conversion by the mitochondrial enzyme succinate dehydrogenase, resulting in the formation of insoluble purple formazan crystals. These crystals can be dissolved in dimethyl sulfoxide (DMSO) and quantified spectrophotometrically by measuring their absorbance at 570 nm. The detected light is thereby proportionate to the number of metabolically active, living cells[278].

In preparation for treatment, 5 000 cells per well were seeded in triplicates in a 96-well plate one day prior. The cell count was determined using a Neubauer counting chamber. On the following day, the growth medium was aspirated and replaced with treatment medium (culture medium without FBS), containing 1 µM aSyn, 0.1% SDS or equal amounts of buffer MES. Additionally, wells without cells but with medium were included in the assay and treated with MTT for background measurements. The aSyn treatment involved the use of monomers and the final product of aggregation (monitored by NMR under sterile conditions).

SH-SY5Y cells were incubated in the treatment medium for 48 hours at 37 °C and 5% CO_2. Subsequently, the medium was replaced with MTT solution (0.5 mg/ml in PBS) and incubated for 2 hours at 37 °C. The MTT solution was aspirated, and formazan crystals were solubilized in DMSO with agitation in the dark. Absorbance at 570 nm was then measured (POLARstar Omega, BMG Labtech). Following background subtraction, the data was normalized by defining the absorbance measured for medium-only treated cells as 100%. Three biological replicates were analyzed for WT and Y39E aSyn.

2.3.3 Cellular Inclusions in H4 Cells

To investigate the aggregation of Y39E aSyn in a cellular context, the aSyn-SynT/Synphilin-1 model was employed with 3 biological replicates for WT and Y39E

aSyn. In this model, H4 cells are co-transfected with plasmids encoding aSyn-SynT or Synphilin-1. aSyn-SynT, comprising the human aSyn fused C-terminally to the first 95 amino acids of the green fluorescent protein (GFP), promotes aSyn aggregation. Synphilin-1, a binding partner of aSyn, colocalizes in cellular aggregates and enhances aSyn aggregation[279]. This assay, extensively validated for evaluating and quantifying intracellular aSyn inclusions, is commonly used to assess the impact of aSyn mutations[280,281].

Two days before transfection, coverslips were coated by placing them in 12-well plates and overlaying them with a 1.5% gelatine solution. After a 1-hour incubation at room temperature, the solution was removed, and coverslips were left to dry overnight. The following day, 80 000 cells per well for immunofluorescent staining on coated coverslips or 100 000 cells per well for western blotting were seeded in 12-well plates and incubated overnight at 37 °C and 5% CO_2. Cell counts were determined using a Neubauer counting chamber.

2.3.3.1 Transfection

H4 cells were transfected with FuGene HD Transfection Reagent (Promega) using 1 µg of each plasmid and 6 µl FuGene in a total volume of 100 µl per well. Plasmids were diluted in medium and incubated for 15 min at room temperature with FuGene. The transfection mix was added dropwise to the wells, and cells were further incubated for 24 hours at 37 °C and 5% CO_2.

2.3.3.2 Immunofluorescent Staining

Following the incubation period, cells were washed 3 times for 5 min in PBS and fixed in 4% paraformaldehyde for 20 min at room temperature with agitation. After 3 washes for 5 min each with PBS, membrane permeabilization was achieved by incubating the cells for 20 min at room temperature with 0.1% Triton-X100 in PBS with agitation. The supernatant was removed, and unspecific antibody recognition sites were blocked in 3% bovine serum albumin (BSA) in PBS (blocking solution) for 1 hour at room temperature with agitation. Incubation with primary antibodies (Table **7**) was carried out in blocking solution overnight at 4 °C with agitation. The next day,

cells were washed 3 times for 5 min in PBS and incubated with secondary antibodies (Table 7) in blocking solution for 2 hours in the dark at room temperature. To minimize background fluorescence, cells were washed once more 3 times for 5 min in PBS, and the nucleus was visualized by DAPI staining (1:10 000 in blocking solution) for 5-10 min. After washing off excess DAPI with PBS (3 times for 5 min), coverslips were mounted with Mowiol and dried overnight in the dark at room temperature. Images were captured using a Leica Inverted Microscope DMI 6000 B (Leica) equipped with a 40x objective (HCX Pl Fluotar) or a 63x objective (HCX Pl Fluotar).

Table 7: Antibodies for immunofluorescent staining. Primary and secondary antibodies used in the cellular inclusion assay are stated, specifying their origin and dilutions.

Target	Species	Manufacturer	Dilution
Primary antibodies			
aSyn	mouse	BD Transduction	1:1000
pAB to V5 tag	rabbit	Abcam	1:1000
Secondary antibodies			
Alexa Fluor 555 anti-mouse	donkey	Invitrogen	1:1000
Alexa Fluor 488 anti-rabbit	donkey	Invitrogen	1:1000

2.3.3.3 SDS-PAGE and Western Blotting

To validate the equal expression levels of aSyn, SDS-PAGE and subsequent western blotting were conducted. Cell lysates were quantified for their total protein content, and equal protein amounts were separated on SDS-polyacrylamide gels. The proteins were then transferred to a membrane and visualized by antibody staining[282].

Transfected H4 cells were washed once with PBS and lysed by adding radioimmunoprecipitation assay (RIPA) buffer (50 mM Tris pH 8.0, 150 mM NaCl, 0.1% SDS, 1% Nonidet P40, 0.5% sodium-deoxycholate, and freshly added

cOmplete Protease Inhibitor Cocktail (Roche)). Cells were scraped, and lysates were collected and stored at -20 °C.

The total protein concentration of the lysate was determined using the Bradford Protein Assay Kit (Pierce). In brief, 50 µl H_2O or standard BSA samples were placed in triplicates into a 96-well plate. Then, 1 µl lysate was added to H_2O-containing wells before adding 150 µl Bradford reagent to samples and standards. The plate was incubated for 15 min at room temperature in the dark, and absorbance was measured at 595 nm on an Infinite M200 Pro (Tecan) plate reader.

Next, 30 µg protein, supplemented with 5x Lämmli buffer (250 mM Tris pH 6.8, 10% SDS, 1.25% bromophenol blue, 5% β-mercaptoethanol, 50% glycerol) were separated by SDS-PAGE using 12% separating / 4% stacking SDS-polyacrylamide gels (as described in section 2.1.3.1), and the PageRuler Plus Prestained Protein Ladder (ThermoScientific). After completed protein separation, the proteins were semi-dry transferred to a PVDF membrane using a Trans-Blot Turbo System (Bio-Rad) and Trans-Blot Turbo Mini 0.2 µm PVDF Transfer Packs (Bio-Rad). Blotting was performed at 25 mA for 30 min. Blocking of unspecific antibody recognition sites was done in 5% BSA in TBS-T (20 mM tris, 150 mM NaCl, 0.1% Tween 20, pH 7.5) for 1 hour at room temperature with agitation. The membrane was incubated with the primary antibody against aSyn (BD Transduction 1:5000) in blocking solution overnight at 4 °C with agitation. The following day, the membrane was washed 3 times for 5 min in TBS-T. Subsequently, secondary antibody incubation with anti-mouse HRP-conjugated antibody (1:10,000 in blocking solution) for 1 hour at room temperature with agitation was performed.

After washing 3 times for 5 min with TBS-T, the Immobilon Western Chemiluminescent HRP Substrate (Merck Millipore) was employed to visualize proteins on a Fusion Fx detection system (Vilber Lourmat). To do so, detection reagents 1 and 2 were combined in a 1:1 ratio, added to the membrane, and visualized within 5 min. Subsequently, the membrane underwent a brief wash in TBS-T, followed by a repetition of the primary and secondary antibody incubation and detection steps. The antibodies used were anti-β-tubulin (rabbit, Santa Cruz, 1:5000) and anti-rabbit HRP-conjugated antibody (1:10 000).

2.4 Animal-based Methods

2.4.1 Site-directed Mutagenesis PCR and Molecular Cloning

With the aim to generate transgenic *C. elegans* strains, plasmids containing tissue-specific promoters and encoding WT or Y39E aSyn tagged with a fluorescent protein were constructed. All plasmids used in animal-based methods carried ampicillin resistance genes, further details are provided in the Appendix (Supplementary Figure **1**).

The plasmid pFR4023, encoding WT aSyn fused C-terminally to the yellow fluorescent protein (YFP) and driving its expression in the body wall muscles of *C. elegans* (*myo3* promoter), was generously provided by Stefan Eimer (Goethe University Frankfurt, Institute of Cell Biology and Neuroscience, Department of Strurtural Cell Biology). Using site-directed mutagenesis PCR and molecular cloning strategies, the Y39E mutation was introduced. Additionally, a transition to the pan-neuronal promoter (*rab3* promoter) was performed, resulting in aSyn expression across all neuronal cells of *C. elegans*, with aSyn fused to the fluorescent protein mCherry. For exclusive expression in dopaminergic neurons, the *dat1* promoter was incorporated, and aSyn was fused to YFP (Table 8).

Table 8: Plasmids encoding aSyn used to generate transgenic *C. elegans* stains. The table lists plasmid names, promoters, and the fluorescent tag fused C-terminal to aSyn.

Plasmid	aSyn	Promoter (tissue)	Tag
pFR4023	WT	*myo3* (body wall muscles)	YFP
pFR5978	Y39E		
pFR5896	WT	*rab3* (all neurons)	mCherry
pFR6049	Y39E		
pFR6050	WT	*dat1* (dopaminergic neurons)	YFP
pFR6054	Y39E		

2.4.1.1 Introduction of the Y39E Mutation via site-directed Mutagenesis

Site-directed mutagenesis PCR was conducted to introduce the Y39E mutation in aSyn. An overview of the mutagenesis process is depicted in Figure 25.

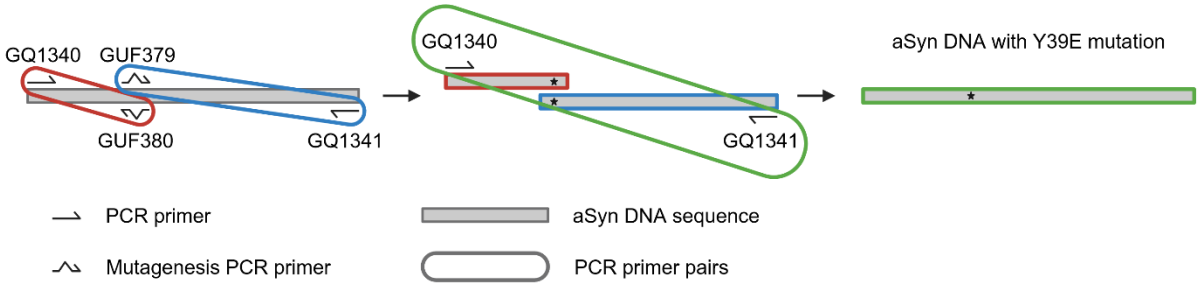

Figure 25: Site-directed mutagenesis PCR overview. The principal of site-directed mutagenesis PCRs to generate the Y39E mutant is shown.

In the first step, two PCR reactions were set up to mutate position 39, using the primer pairs GQ1340/GUF380 or GQ1341/GUF379. The PCR program and oligonucleotides are provided in Table 9 and Table 10, respectively. The reaction mix contained 50 ng template DNA (plasmid pFR4023), 1 µl of each primer (10 pmol) and 12 µl KAPA Polymerase (Kapabiosystems) in a total volume of 24 µl.

Table 9: Mutagenesis PCR program. The temperature and time of each step of the mutagenesis PCR is displayed along with the number of repetitions.

Step	Temperature [°C]	Time	Cycle repetition
Denaturation	95	3 min	
Denaturation	98	20 sec	x 35
Primer annealing	65	15 sec	
Extension	72	30 sec	
Extension	72	1 min	
Hold	4	∞	

Table 10: PCR Primer to introduce the Y39E mutation. A description of the primers and their sequence are listed.

Primer	Description	Sequence 5' → 3'
GQ1340	aSyn forward primer, introducing AgeI and KpnI recognition sites upstream	GGGGGTACCGGTAATGGATGTATTC ATGAAAGGACTTTC
GQ1341	aSyn reverse primer, deleting stop codon and introducing NotI recognition sites downstream	GGGGCTAGCGCGGCCGCCACCGGC TTCAGGTTCGTAGTCTTG
GUF379	aSyn Y39E forward mutation primer	GGTGTTCTCGAAGTAGGCTCCAAAA CCAAGGAG
GUF380	aSyn Y39E reverse mutation primer	GGAGCCTACGAAGAGAACACCCTCT TTTGTCTT

The template plasmid was digested by DpnI. Hereby, 0.5 µl DpnI (ThermoScientific) and 3 µl Tango buffer (ThermoScientific) were added to the PCR products and incubated at 37 °C for 1 hour. Next, the two PCR products were combined in one reaction. The third PCR reaction used the same components, followed the same PCR protocol, employed the primer pair GQ1340/GC1341, and used 1 µl of each PCR product from the previous reactions as templates.

In a next step, the resulting product was purified through agarose gel extraction. Therefore, 1% agarose gels containing ethidium bromide were casted and run in TAE buffer (40 mM tris, 5 mM EDTA, 20 mM acetic acid). The samples, supplemented with 10x loading solution (60% glycerol, 20 mM EDTA, 10 mM tris, spatula tip OrangeG), were separated at 150 V in a horizontal electrophoresis system. Gel documentation was performed on a GenoPlex (VWR) equipped with the GenoCapture software. DNA extraction utilized the Gene Elute Gel Extraction Kit (Sigma Aldrich) following the manufacturer's instructions, with elution performed in H_2O.

To distinguish bacteria, which were successfully transformed with the correctly cloned plasmid, the pGEM-T Easy Vector System (Promega) was employed, which makes

use of the TA-vector cloning method and blue-white screening of transformed colonies[283,284]. To ligate the purified PCR product into the pGEM-T Easy Vector System, A-overhangs at both ends of the PCR product were introduced. 15 µl of purified PCR product were incubated at 65 °C for 30 min with 0.5 µl $MgCl_2$ (50 mM, Invitrogen), 0.5 µl dNTPs (10 mM, Invitrogen), 2.5 µl 10x PCR buffer (minus $MgCl_2$, Invitrogen) and 0.5 µl Taq Polymerase (Invitrogen) in a total volume of 25 µl. Subsequently, ligation was performed by incubating 1 µl purified PCR product with A-overhangs along with 0.5 µl pGEM-T vector, 5 µl 2x Rapid ligation buffer (Promega), and 1 µl T4 Ligase (Promega) in a total volume of 10 µl overnight at 4 °C.

For amplification and purification of the ligated plasmid, transformation into competent *E. coli* DH5α (Invitrogen) was conducted. Competent cells, stored at -80 °C, were thawed on ice. A 100 µl aliquot of cells was added to the ligation reaction and incubated on ice for 20-30 min. Subsequently, a heat-shock at 42 °C was performed for 45 sec, followed by an additional 2 min-incubation on ice. 900 µl of LBm were added and samples incubated at 37 °C for > 30 min at 250 rpm to achieve ampicillin resistance. Cells were then pelleted by centrifugation (2 min, 5000 rpm), resuspend in 100 µl LBm and plated on LBa plates supplemented with AMP, 40 µl IPTG (100 mM, Carl Roth) and 40 µl X-Gal in DMSO (20 mg/ml, ThermoScientific) for blue-white screening. Plates were incubated overnight at 37 °C.

For plasmid extraction from bacteria, 5 ml LBm with AMP were inoculated with single colonies from transformation plates. After overnight incubation at 37 °C with 250 rpm agitation, plasmids were purified using the PureLink Quick Plasmid Prep Kit (Invitrogen) following the manufacturer's instructions. DNA was eluted in 50 µl H_2O and analyzed by restriction hydrolysis, followed subsequent separation and visualization on 1% agarose gels. Clones exhibiting a correct restriction hydrolysis pattern underwent sequencing (GATC/Eurofins Scientific).

To clone the Y39E aSyn from the pGEM-T vector system into the pFR vectors, restriction cloning strategies were employed. Molecular cloning was facilitated by designing mutagenesis primers to introduce the same restriction enzyme recognition sites up- and downstream of aSyn as present in the template vector pFR4023 (Table 10). Consequently, for the exchange of the WT aSyn coding sequence with the Y39E aSyn DNA, 2.5 µg pFR4023 or pGEM-T with Y39E aSyn were incubated with 0.5 µl each of KpnI-HF (New England Biolabs) and NotI-HF (New England Biolabs), along

with 2 µl 10x CutSmart buffer (New England Biolabs), in a total volume of 20 µl at 37 °C for 1 hour. The product was separated on 1% agarose gels, and the backbone vector (pFR4023) and insert (Y39E aSyn) were extracted as described above. Ligation involved 1 µl backbone vector and 7.5 µl insert, along with 1 µl 10x T4 ligation buffer (ThermoScientific) and 0.5 µl T4 Ligase (ThermoScientific). The ligation reaction was incubated overnight at 4 °C. Transformation, plasmid purification, restriction control, and sequencing were carried out as indicated above, using AMP LBa plates for transformation, resulting in the generation of pFR5978.

2.4.1.2 Expression of aSyn in Neuronal Cells

Restriction cloning was additionally employed to generate the vectors pFR5896 and pFR6049. For this purpose, the *rab3* promoter was excised from a plasmid exhibiting the same restriction sites up- and downstream of the promoter region (pFR4956) as present in pFR4023, kindly provided by Stefan Eimer. PstI-HF (New England Biolabs) and AgeI-HF (New England Biolabs) were employed as restriction enzymes. All other components and steps, including sequencing to ensure the correct incorporation of the promoter, were performed as indicated above. Subsequently, the C-terminal fused YFP was exchanged with mCherry using the same principal. The vector pFR1808 provided by Stefan Eimer and encoding mCherry was used in conjunction with the *rab3* aSyn plasmids. Restriction enzymes Acc65I, XhoI, BamHI, and BglII (New England Biolabs) were utilized, along with their respective restriction buffers (CutSmart or buffer 3.1 (New England Biolabs)).

2.4.1.3 Expression of aSyn Exclusively in Dopaminergic Neuronal Cells

To express aSyn exclusively in dopaminergic neurons, a PCR-based method was applied. Using genomic DNA of *C. elegans* (provided by Stefan Eimer), the *dat1* promoter was amplified using the mutagenesis primers GC111 and GC112 (Table 11), which introduced HindIII and PstI restriction sites upstream and BamHI and KpnI restriction sites downstream of the promoter. The same PCR program as described for generating the Y39E mutation was employed, using an extension time of 50 sec

(Table 9). The PCR product and pFR4023 or pFR5978 were then digested with PstI-HF and KpnI-HF (New England Biolabs), ligated, transformed into *E. coli*, amplified, purified, and sequenced as described above.

Table 11: Primers used to amplify the *dat1* promoter. Primers to amplify the *dat1* promoter and introducing restriction enzyme recognition sites up- and downstream are listed.

Primer	Description	Sequence 5' → 3'
GQ111	Forward primer to amplify the *dat1* promoter and introduces a HindIII and PstI restriction site upstream	CCCAAGCTTCTGCAGTCCATGAAAT GGAACTTGAATCC
GQ112	Reverse primer to amplify the *dat1* promoter and introduces a BamHI and KpnI restriction site downstream	GGTACCGGATCCGGCTAAAAATTGT TGAGATTCGAG

2.4.2 *C. elegans* Maintenance

C. elegans strains were cultured on Nematode Growth Medium (NGM) plates containing 1.6% agar, 0.25% peptone, 50 mM NaCl, 1 mM $CaCl_2$, 5 µg/ml cholesterol in 95% ethanol, 25 mM KPO_4, 1 mM $MgSO_4$, and 10 µg/ml Nystatin (AppliChem) in DMSO. These plates were seeded with *E. coli* OP50 and maintained at 20 °C[248]. *C. elegans* strains used in this study are listed in Table 12.

Table 12: *C. elegans* strains used in this study. A description of the strains is provided.

Strain	Genotype	Description	Reference
N2 Bristol	Wild type		
BZ555	egIs1 [dat-1p::GFP]	GFP expression in dopaminergic	Kindly provided by Stefan Eimer

Strain	Genotype	Description	Reference
		neurons	
RM2707 dat-1(ok157) III	Cosmid coordinates (with respect to T23G5): 24967-26802 (or 24965-26800, or 24966-26801, or 24968-26803, or 24969-26804). Flanking sequences: CTATTCGGATATCTTGCCAAT GCTA//TAGGAATTATTTTTGCG CTCTCAGG. Deletion size: 1836 bp.	Knockout of the dat-1 shuttle	Kindly provided by Stefan Eimer

2.4.3 Generation of Mutant Strains via Microinjection

Transgenic *C. elegans* strains with extrachromosomal arrays were generated through microinjection using a FemtoJet (Eppendorf) connected to an Axiovert 200 Microscope (Carl Zeiss). The injection mix contained the plasmid of interest along with a co-injection marker to identify positive progeny. The DNA concentration of the injection mix was adjusted to 100 ng/µl by adding pBluescript II SK(+). The injection mix was injected into the distal gonads of young adults as described by Mello and Fire, 1995[285]. Therefore, the nematodes were immobilized in oil on a dried 2% agarose pad. Following the injection process, the nematodes were rescued through the addition of M9 buffer (22 mM KH_2PO_4, 42 mM Na_2HPO_4, 86 mM NaCl, 1 mM $MgSO_4$) and then transferred to NGM plates pre-seeded with OP50. Nematodes belonging to the F1 generation and expressing the co-injection marker, were individually isolated on NGM plates. A positive F1 progeny, if resulting in positive F2 progeny, constituted a transgenic strain. Co-injection markers used in this study included the dominant mutant *rol-6(su1006)*, which induces circular crawling and rotation around the body axis in nematodes. Additionally, fluorescent co-injection markers, namely *ttx-3::RFP*, *myo-2::GFP*, *myo-2::RFP*, and *myo-2::mTFP*, facilitated the expression of fluorescent proteins in two head neurons (*ttx-3*) or the pharynx

muscles (*myo-2*). Details of the injection mixes used in this study are provided in Table 13.

Table 13: Injection mixes used for microinjection. The composition of the injection mixes is stated.

Injection mix number / strain	Plasmid of interest	Co-injection marker
06 / WTTC	40 ng/µl *myo-3::aSynWTtagYFP* [pFR4023] 2 ng/µl *myo-3::TOM70mCherry* [pFR5754]	40 ng/µl *rol-6(su1006)* 5 ng/µl *myo-2::RFP*
09 / TCCtr	2 ng/µl *myo-3::TOM70mCherry* [pFR5754]	5 ng/µl *myo-2::RFP*
20 / Y39ETC	40 ng/µl *myo-3::aSynY39EtagYFP* [pFR5978] 2 ng/µl *myo-3::TOM70mCherry* [pFR5754]	40 ng/µl *rol-6(su1006)* 5 ng/µl *myo-2::RFP* 5 ng/µl *myo-2::mTFP*
42 / WTrab	55 ng/µl *rab-3::aSynWTmCherry* [pFR5896]	40 ng/µl *rol-6(su1006)* 20 ng/µl *ttx-3::RFP*
45 / Y39Erab	55 ng/µl *rab-3::aSynY39EmCherry* [pFR6049]	40 ng/µl *rol-6(su1006)* 20 ng/µl *ttx-3::RFP*
59 / WTdat	85 ng/µl *dat-1::aSynWTYFP* [pFR6050]	
63 / Y39Edat	85 ng/µl *dat-1::aSynY39EYFP* [pFR6054]	

2.4.4 Crossings

In order to visualize dopaminergic neurons in the RM2707 (dat1 knockout strain), a crossing with the BZ555 strain was executed. To distinguish between cross- and self-progeny, males were generated from the BZ555 strain. L4 larvae were incubated for 1 hour at 20 °C in 10% ethanol in M9 buffer and subsequently transferred to fresh

NGM plates. Males from the F1 generation were obtained and crossed with hermaphrodites of the RM2707 strain. Positive F1 progeny resulting from the cross were isolated on individual NGM plates and allowed to lay eggs. This process was repeated for positive progeny of the F2 generation. Following egg laying, F2 hermaphrodites, along with N2 WT hermaphrodites as a positive control and RM2707 hermaphrodites as a negative control, underwent lysis and genotyping via PCR reaction.

Worm lysis involved adding single (F2 hermaphrodites) or multiple (N2 WT or RM2707) nematodes to 15 µl lysis buffer (10 mM Tris pH 8.3, 50 mM KCl, 2 mM $MgCl_2$, 0.2 mM Proteinase K (Carl Roth)). Lysis was performed by freezing the worms at -80 °C for at least 10 min and subsequently incubating at 65 °C for 1 hour. Following a 10-min incubation at 95 °C to inactivate the proteinase K, genotyping PCR was carried out. The PCR reaction comprised 2 µl worm lysate, 0.25 mM dNTPs (Genaxxon), 10 mM Tris pH 8.3, 50 mM KCl, 20 mM $MgCl_2$, 10 pmol forward and reverse primer, and 0.25 µl Taq A polymerase (amplified and purified by the research group of Stefan Eimer) in a total volume of 25 µl. The genotyping primers and PCR program are detailed in Table 14 andTable **15**.

Table 14: Genotyping primer for PCR reaction. The sequences of the primers used to detect the dat1 knockout are listed.

Primer	Description	Sequence 5’ → 3’
GQ555	Genotyping of dat1 knockout, forward primer	ACCCGCGGCTAAAGTTCTCAT
GQ556	Genotyping of dat1 knockout, reverse primer	TTACCAGAGGCTTTGTAGAACT

Table 15: PCR program for genotyping. The PCR program used for genotyping the dat1 knockout is stated.

Step	Temperature [°C]	Time	Cycle repetition
Denaturation	94	3 min	
Denaturation	94	30 sec	x 40
Primer annealing	60	45 sec	
Extension	72	60 sec	
Extension	72	10 min	
Hold	10	∞	

The PCR product was analyzed on a 1% agarose gel, as previously described, to confirm the deletion of the dat1 gene.

2.4.5 Imaging

One day prior to imaging, animals were staged at the larval L4 stage to ensure imaging of young adult hermaphrodites. Nematodes were immobilized in a drop of 50 mM NaN_3 in M9 buffer on freshly prepared 2% agarose pads on microscope cover slides before being covered with a glass cover slip. Between 25 and 40 individuals were imaged per genotype on at least two different days. Confocal imaging was executed on a Zeiss LSM 780 NLO (63x/1.4 or 40x/1.3 oil-objective) or on a VisiScope spinning disk confocal microscope (Visitron Systems), utilizing the DMi8 inverted microscope (Leica) equipped with a YokogawaCSU XI scan head, a Hamamatsu ORCA-Flash 4.0 CC1140, and a super-resolution correction unit by GATACA LiveSR system (63x/1.4-0.6 oil-objective). Z-stacks of 0.3-0.4 µm were captured on both microscopes, and maximum intensity projections were performed using Fiji (ImageJ).

To assess neurodegeneration of dopaminergic neurons, animals were subjected to 6-hydroxydopamine (6OHDA) treatment one day before imaging. 6OHDA enters cells via the dopamine transporter dat1, causing an increase in free radicals and leading to neurodegeneration. Thus, 6OHDA selectively induces toxicity in dopaminergic neurons. The concentration used in this study was 50 mM, sufficient to induce a weak neurodegenerative phenotype and establish a sensitized background[286]. L4 larvae were staged and transferred to the assay mix in a glass tube. The assay mix comprised 50 mM 6OHDA and 10 mM ascorbic acid to prevent 6OHDA oxidation in PBS buffer. Animals were incubated in the assay mix for 1 hour at room temperature with agitation and subsequently transferred with a glass pipet to NGM plates. The following day, animals were anesthetized and imaged as indicated above.

2.4.6 Behavioral Assay

To assess the impact of Y39E aSyn on dopaminergic neurodegeneration, the food slowing response was analyzed. Healthy individuals exhibit reduced crawling speed in the presence of bacterial food, a behavior mediated by the mechanosensitive characteristics of dopaminergic neurons in *C. elegans*. As dopaminergic neurodegeneration progresses, individuals lose the ability to detect food, resulting in an increased crawling speed on bacterial lawn compared to controls[286].

The experimental procedure involved staging individuals one day prior to the assay at the larval L4 stage. On the following day, animals were transferred to fresh NGM plates seeded with OP50, and the number of body bends was counted for a duration of 1 min. Subsequently, individuals were transferred to unseeded NGM plates, and body bends were again counted. Before each counting session, individuals were allowed a 2-min acclimation period to the new environment. A minimum of 37 individuals per group were included in the assay.

2.4.7 Western Blotting

To validate the comparable expression levels of aSyn across various *C. elegans* strains, western blotting was conducted. For this purpose, 100 aSyn-expressing worms per strain were harvested in PBS supplemented with phosphatase and protease inhibitors (PhosphoStop Phosphatase Inhibitor Cocktail Tablets, Roche; complete EDTA-free Protease Inhibitor Cocktail Tablets, Roche). Animals underwent two washes by centrifugation at 200 g for 1 min, discarding the supernatant each time, and resuspending the pellet in fresh PBS supplemented with inhibitors. The worm pellet was then resuspended in 60 µl lysis buffer (150 mM NaCl, 1 mM EDTA, 25 mM Tris pH 7.5, 10% glycerol, 1% Triton X, supplemented with 100 mM DTT, 4 mM Pefabloc SC-Protease Inhibitor (A 154.1, Roth), and the above-mentioned phosphatase and protease inhibitors) before being shock-frozen in liquid nitrogen.

Upon thawing, 15 µl of 4x SDS-PAGE protein sample buffer (40% glycerol, 240 mM Tris pH 6.8, 8% SDS, 5% β-mercaptoethanol, 0.04% bromophenol blue) were added, and samples were sonicated on ice for 3 min (20 sec on, 10 sec off, 70% amplitude) using a SonoPlus mini20 Sonicator (3665, Bandelin, Sonotrode Type MS2.5). Lysates were boiled at 100 °C for 10 min, centrifuged at 17 000 g for 10 min, and 30 µl of lysate was separated on 4% stacking / 12% separating SDS-polyacrylamide gels. The gel composition is outlined in **Fehler! Verweisquelle konnte nicht g efunden werden.**, protein separation was achieved at 80-130 V in running buffer (25 mM Tris, 198 mM glycine, 3.5 mM SDS). Subsequently, proteins were transferred to a PVDF membrane (10600023, Amersham Hybond) by applying 220 mA for 90 min under cooling conditions in blotting buffer (48 mM Tris, 39 mM glycine, 10% ethanol).

Table 16: Composition of SDS-polyacrylamide gels for western blotting of *C. elegans* lysates

	12% separating gel	**4% stacking gel**
(Bis)-acrylamide (1% / 29%)	40%	18.2%
Tris 1 M, pH 8.8	24.6%	
Tris 0.5 M, pH 6.8		19.8%

	12% separating gel	4% stacking gel
SDS 10%	1%	1%
APS 10%	1%	1%
TEMED	0.13%	0.1%

To prevent non-specific antibody binding, the membrane was incubated in 1% semi-skimmed milk in TBS-T buffer (20 mM Tris, 150 mM NaCl, 0.1% (v/v) Tween 20, pH 7.6) for 1 hour with agitation. Primary antibody incubation occurred overnight at 4 °C in blocking solution with agitation using a mouse anti-aSyn antibody (1:1000, 610787, BD Transduction Laboratories). After washing 3 times for 7 min in TBS-T, membranes were incubated at room temperature for 1 hour with agitation in blocking solution containing the secondary antibody (goat anti-mouse HRP-conjugated, 1:5000, 1721011, Bio-Rad Laboratories, Inc.). Following 3 washes with TBS-T for 7 min, aSyn was detected. Protein visualization employed the chemiluminescence ECL Kit Prime Western Blotting Detection Reagents (RPN2232, Amersham), with a 1:1 mixture of Solution A and B applied to the membrane. Images were captured on an Intas ChemoCam Imager. Repetition of primary and secondary antibody incubation, followed by image development, was undertaken to visualize the housekeeping gene α-tubulin (mouse anti-α-tubulin 1:2000, T6199, Sigma-Aldrich).

2.5 Software and Statistical Analysis

Statistical analysis was performed with GraphPad Prism versions 5 to 7. For testing normality distributions, the D'Agostino and Pearson test or the Shapiro-Wilk test for small number of repetitions was used. If data followed a gaussian distribution, unpaired, two-tailed t-tests or One-way ANOVA with the post-hoc Bonferroni's multiple comparisons test were performed. If there was no gaussian distribution of data sets, the Mann-Whitney test was applied. Error bars represent the standard

error of the mean, and p-values are denoted by asterisks: ns: $p > 0.05$, *: $p < 0.05$, **: $p < 0.01$, ***: $p < 0.001$, ****: $p < 0.0001$.

Image processing and analysis were conducted using Fiji (ImageJ). Figure compositions utilized Adobe Illustrator, Microsoft PowerPoint (Microsoft Corporation), or BioRender.

Furthermore, various software tools were utilized throughout the study, including different versions of SnapGene, Ugene, PyMOL, Topspin, CCPN, Microsoft Word and Excel, SigmaPlot, Zentasizer 7.03, Unicorn 7.3, Spectra Manager, and Omega software.

3 Results

3.1 Structural Characterization of the Y39E aSyn Monomer

To explore differences between WT aSyn and the phosphomimetic mutant Y39E, in a first step the monomer was addressed regarding its structure, dynamics and interaction with lipid membranes. Firstly, the analysis included 2D ^{1}H-^{15}N HSQC NMR spectra to assess chemical shift perturbations in Y39E and WT aSyn. In a second step, PRE measurements of amide groups were performed in order to characterize the network of transient long-range interactions in the studied proteins. Furthermore, secondary structure preferences and backbone dynamics were analyzed, in combination with the measurements of hydrodynamic properties. Finally, investigations of membrane interactions were conducted by titration experiments of aSyn variants with SUVs monitored through CD and NMR spectroscopy.

3.1.1 Structural Properties of Y39E aSyn

Insights into the structural features of monomeric Y39E aSyn were gained through the acquisition and analysis of 2D ^{1}H-^{15}N HSQC NMR spectra (Figure 26). Chemical shift changes between WT and Y39E aSyn were observed only for residues around position 39 and for the pH-sensitive histidine residue located at position 50 (Figure 26B). The investigation of secondary structure properties was achieved by measuring the $^{3}J_{HN\text{-}H\alpha}$ coupling constants. Values between 3.0-6.0 Hz are indicative of α-helical structural elements, while 8.0-11.0 Hz corresponds to β-sheets-rich structures. A coupling constant between 6.0 and 8.0 Hz is characteristic of unstructured regions in a random coil formation[274]. The $^{3}J_{HN\text{-}H\alpha}$ coupling constant values obtained for Y39E and WT aSyn resulted in values between 6 and 8 Hz throughout all residues, indicating a lack of preferences for any secondary structural elements in both monomeric states (Figure 27).

In summary, this data suggests that the structural properties of Y39E aSyn as a monomer do not differ substantially from WT aSyn.

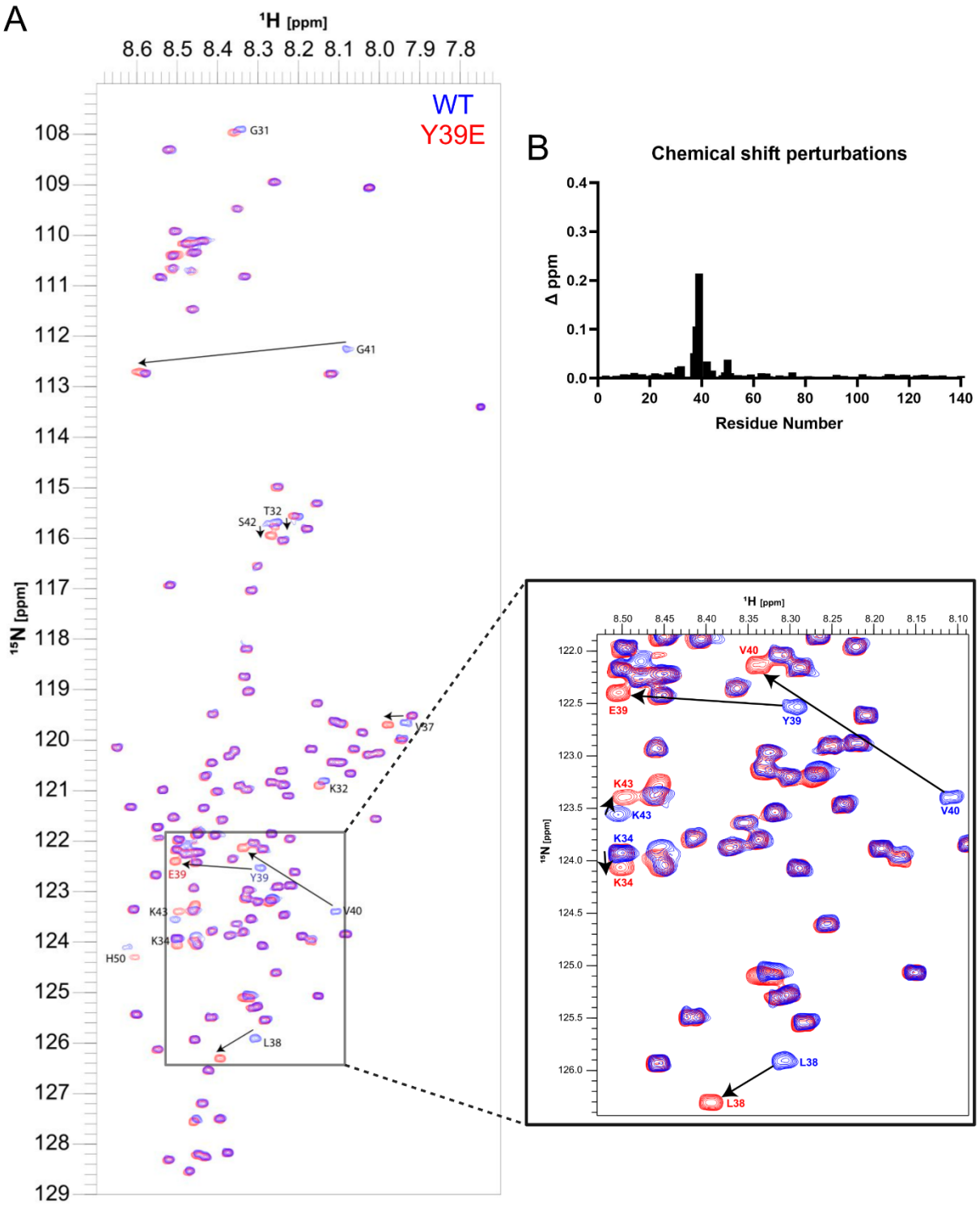

Figure 26: 2D ^{1}H-^{15}N HSQC NMR spectra of WT and Y39E aSyn. (A) Overlayed 2D ^{1}H-^{15}N HSQC NMR spectra of 100 µM aSyn WT (blue) and Y39E (red) in buffer MES, acquired at 15 °C and 600 MHz. (B) Chemical shift perturbation plot of ^{15}N labelled aSyn WT versus Y39E.

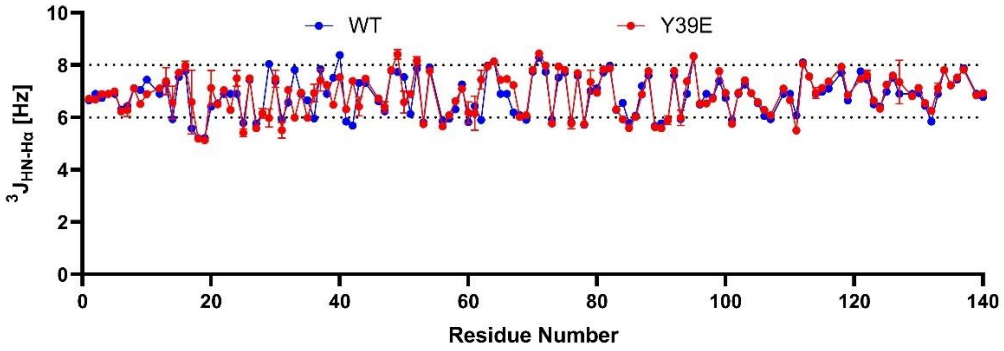

Figure 27: $^3J_{HN-Hα}$ coupling constant. The $^3J_{HN-Hα}$ coupling constant was determined for WT (blue) and Y39E (red) aSyn. Dashed lines indicate limits of random coil structures represented between 6 and 8 Hz. NMR spectra were acquired using 200 µM aSyn in buffer MES at 15 °C and 600 MHz.

3.1.2 Backbone Dynamics of the Y39E aSyn Monomer

For the characterization of the backbone dynamics of Y39E aSyn, ^{15}N R_1 and R_2 rates of amide groups were evaluated. These relaxation parameters of nitrogen atoms present in amide groups correlate with the dynamic properties of proteins, particularly with the degree of mobility of their protein backbone on time scales ranging from picosec to milisec. This allows for direct monitoring of conformational constraints characterizing the protein.

No discernible differences in R_1 relaxation rates between WT and Y39E aSyn were identified (Figure 28A). In contrast, R_2 rates for Y39E aSyn exhibited slight elevations around the regions of residues 10, 25, 60, and 95 (Figure 28B). These differences in R_2 rates were relatively small and coincided mainly with regions containing positive residues, particularly highlighted by the depiction of Lys residues in green in the primary sequence in Figure 28B.

Finally, the hydrodynamic properties of both variants were explored by measuring the hydrodynamic radius by pulse field gradient NMR experiments. Consistent with the structural and dynamical data above, the hydrodynamic radius values were of a comparable magnitude for both WT and Y39E aSyn (WT: 32 ± 1, Y39E: 31 ± 1, Table 17).

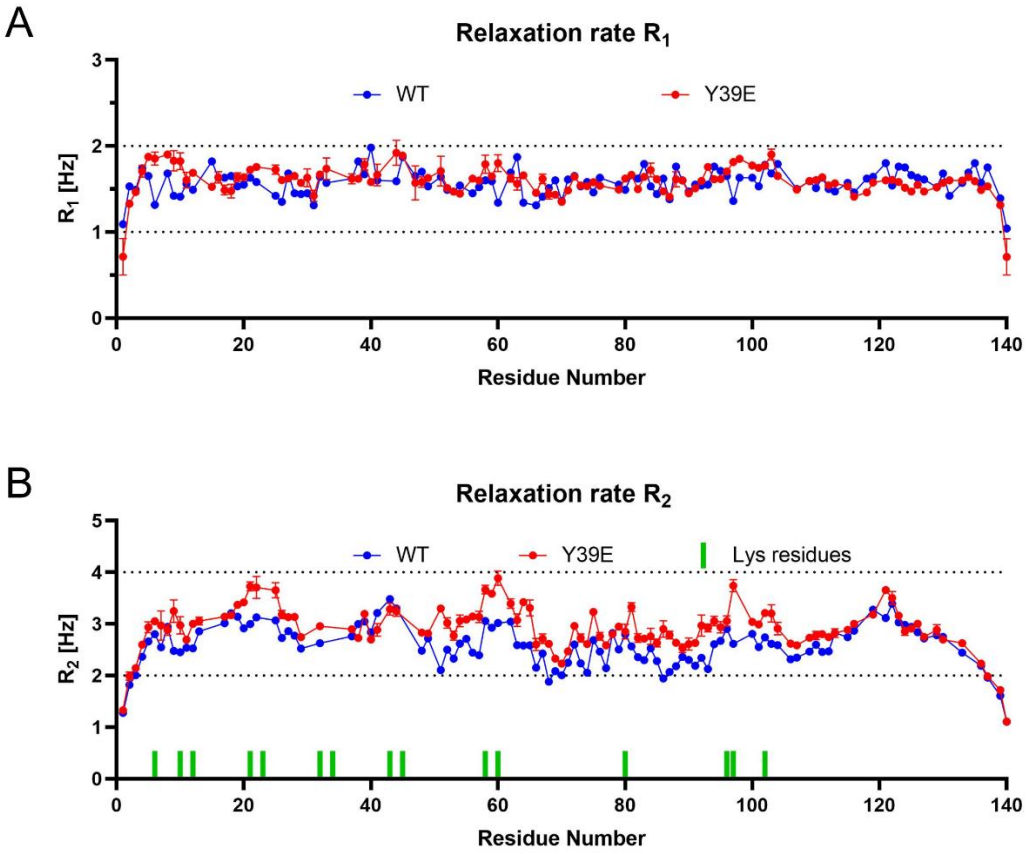

Figure 28: ^{15}N NMR relaxation rates of WT and Y39E aSyn. (A) Relaxation rate R_1 of WT (blue) and Y39E (red) ^{15}N aSyn. (B) Relaxation rate R_2 of WT (blue) and Y39E (red) ^{15}N aSyn. Lysine residues in the primary sequence are depicted in green. NMR spectra were acquired on 200 µM aSyn in buffer MES, at 15 °C and 600 MHz.

Table 17: Hydrodynamic radius of WT and Y39E aSyn. The hydrodynamic radius was determined by pulse field gradient NMR experiments.

	WT	**Y39E**
R_H [Å]	32 ± 1	31 ± 1

Furthermore, in order to explore whether the Y39E mutation induces alterations in the network of transient long-range interactions, the paramagnetic probe MTSL was introduced at positions 18 and 90, respectively, and PRE of backbone amide groups were measured. This involved performing alanine to cysteine mutations at the respective sites, facilitating the covalent binding of the probe through disulfide bridges. The ratio intensity changes in 2D ^{1}H-^{15}N HSQC NMR spectra were

analyzed, where proximity to the paramagnetic probe (up to 20-25 Å) results in a decrease in NMR signal intensity. By locating the probe at positions 18 or 90, it becomes possible to examine transient long-range interactions with the N-terminus or the late-NAC region, respectively. Representative 2D ^{1}H-^{15}N HSQC NMR spectra of Y39E aSyn in the presence and absence of MTSL at positions 18 and 90 are shown in Figure 29A and Figure 30A.

For both WT and Y39E aSyn, transient long-range interactions between position 18 and C-terminal regions (residues 110-140) were observed (Figure 29B, C). Placing MTSL at position 90 revealed differences between Y39E and WT aSyn. While both displayed reduced peak intensity ratios around regions 100-140, only WT exhibited an additional decrease in signal intensity in the region around residue 40 (Figure 30B, C). These differences in the structural profiles found in the MTSL signature of Y39E aSyn however are minor and cannot be correlated with a change in the hydrodynamic radius of the protein.

Considering the results shown in this section, it can be concluded, that no substantial changes exist between the structural and dynamical properties of both proteins in their monomeric states.

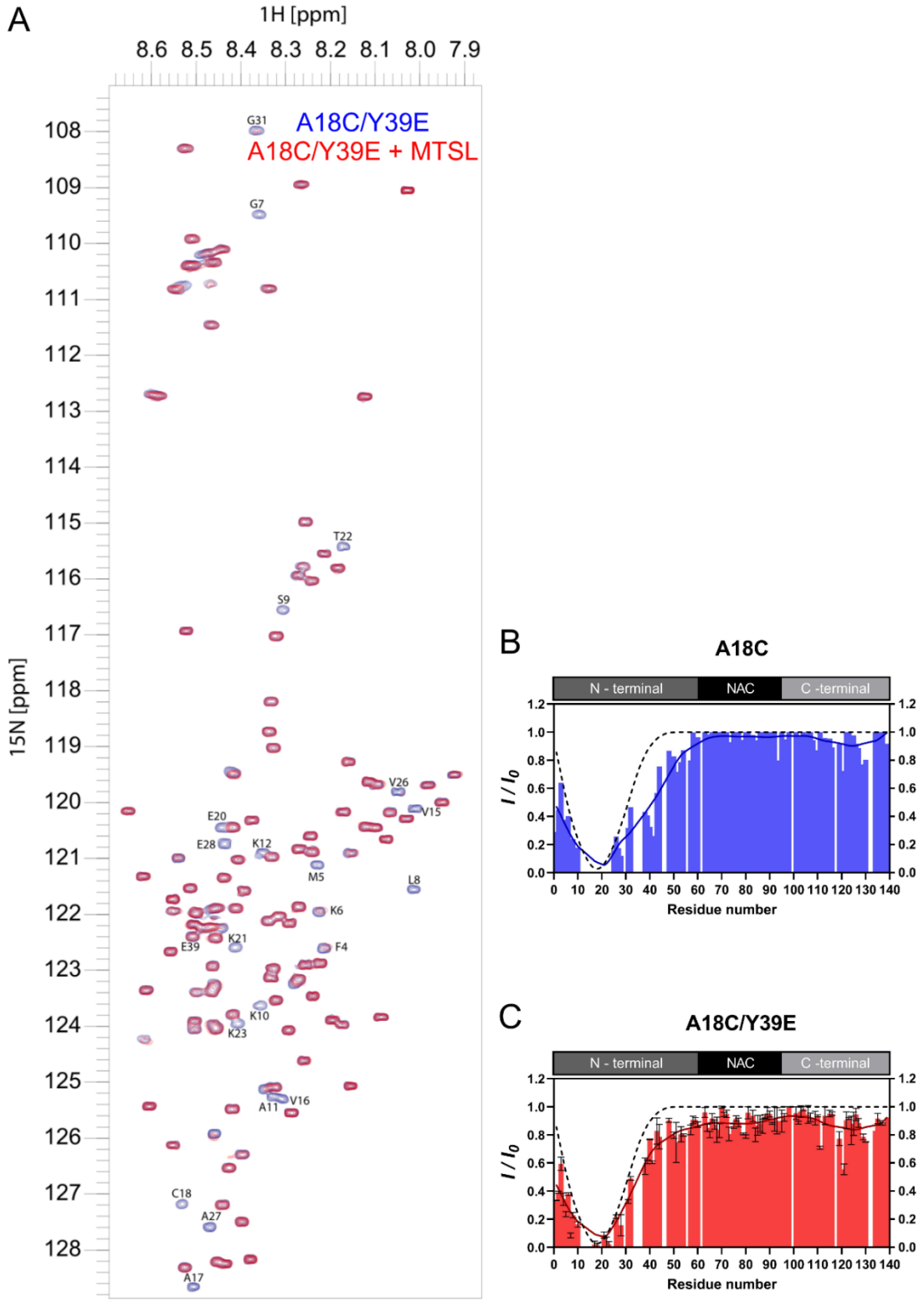

Figure 29: PRE profile of amide groups of aSyn with MTSL probe at position 18. (A) Overlayed 2D ^{1}H-^{15}N HSQC NMR spectra of 100 µM aSyn A18C/Y39E in absence (blue, I_0) and presence (red, I) of MTSL acquired at 15 °C and 600 MHz. (B) Peak intensity ratio (I/I_0) of A18C in absence and presence of MTSL (100 µM aSyn in buffer MES was used and 2D ^{1}H-^{15}N HSQC NMR spectra obtained at 15 °C and 600 MHz). (C) Peak intensity ratio (I/I_0) of A18C/Y39E in absence and presence of MTSL (100 µM aSyn in buffer MES was used and 2D ^{1}H-^{15}N HSQC NMR spectra obtained at 15 °C and 600 MHz). (B, C) Dashed lines represent the expected profile for a random coil polypeptide, with the paramagnetic probe at the same position. Bold lines show LOWESS-fitting curves.

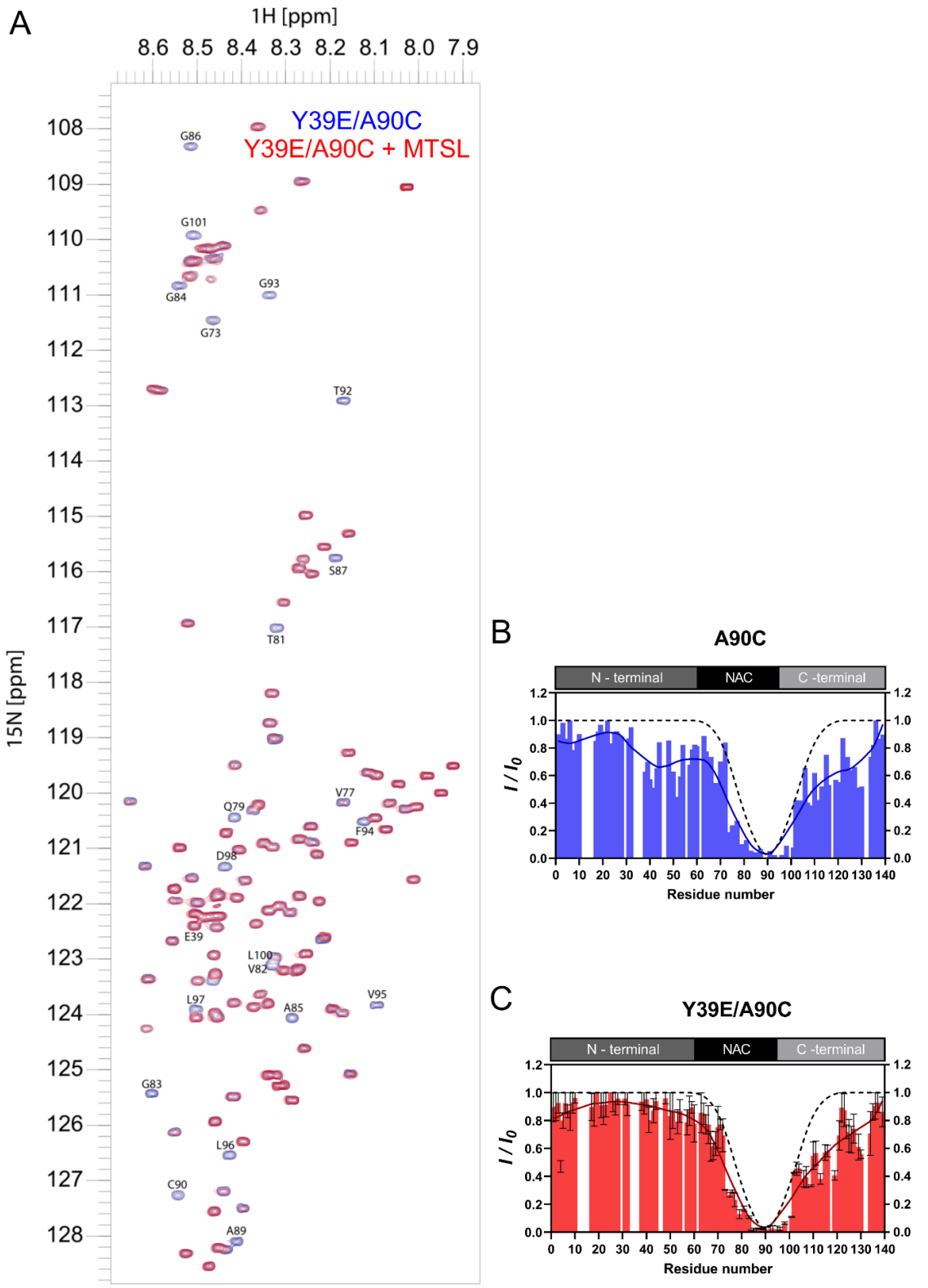

Figure 30: PRE profile of amide groups of aSyn with MTSL probe at position 90. (A) Overlayed 2D ^{1}H-^{15}N HSQC NMR spectra of 100 µM aSyn Y39E/A90C in absence (blue, I_0) and presence (red, I) of MTSL acquired at 15 °C and 600 MHz. (B) Peak intensity ratio (I/I_0) of A90C in absence and presence of MTSL (100 µM aSyn in buffer MES was used and 2D ^{1}H-^{15}N HSQC NMR spectra obtained at 15 °C and 600 MHz). (C) Peak intensity ratio (I/I_0) of Y39E/A90C in absence and presence of MTSL (100 µM aSyn in buffer MES was used and 2D ^{1}H-^{15}N HSQC NMR spectra obtained at 15 °C and 600 MHz). (B, C) Dashed lines represent the expected profile for a random coil polypeptide, with the paramagnetic probe at the same position. Bold lines show LOWESS-fitting curves.

3.1.3 Membrane Affinity Assessment of Y39E aSyn

In a next step, the affinity of Y39E aSyn to membranes was evaluated. CD titration experiments were conducted using SUVs composed of DOPE:DOPS:DOPC in a 5:3:2 ratio, together with 10 µM of either WT or Y39E aSyn (Figure 31A, B). The mean residue ellipticity at a wavelength of 222 nm was plotted against the SUV concentration and fitted as described in detail in section 2.2.2 (Figure 31C). The calculated K_d value for WT was 0.3 µM, and for Y39E, it was 0.3 µM ± 0.03, indicating similar affinity features for both species. The number of lipids bound to a single aSyn molecule (L) was slightly higher for Y39E aSyn (121 for WT and 163 ± 16 for Y39E, Table 18).

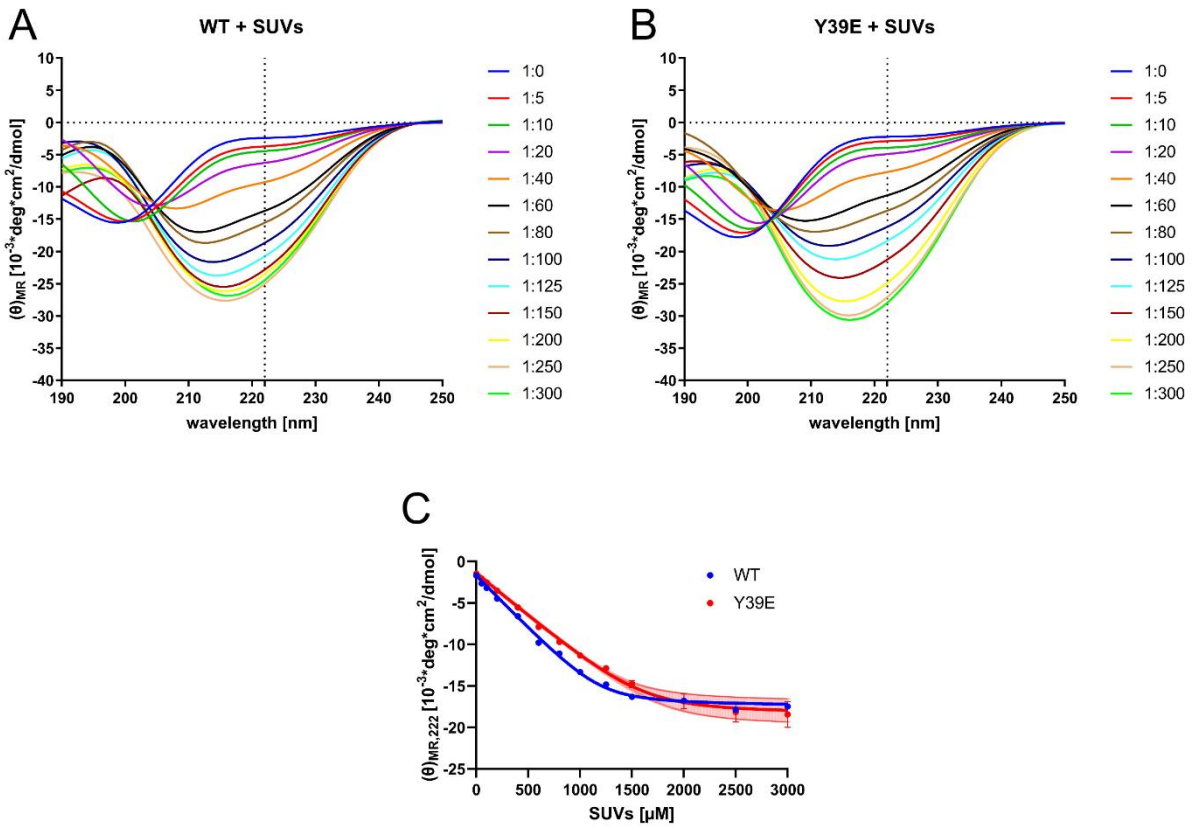

Figure 31: Affinity features of WT and Y39E aSyn to SUVs as monitored by CD. (A) CD spectra of WT aSyn with increasing concentration of SUVs (B) CD spectra of Y39E aSyn with increasing concentrations of SUVs (A,B) aSyn concentration was 10 µM for WT and Y39E. SUVs were composed of DOPE:DOPS:DOPC (5:3:2). Dashed lines are drawn at 222 nm wavelength. (C) Mean residue ellipticity values at 222 nm wavelength are plotted against the SUV concentration for WT (blue) and Y39E (red) aSyn.

Table 18: Membrane binding parameters of WT and Y39E aSyn. Dissociation constant (K_d) and number of lipids interacting with aSyn (L) for WT and Y39E aSyn are displayed.

	K_d [µM]	**L**
WT	0.3	121
Y39E	0.3 ± 0.03	163 ± 16

Subsequently, membrane binding was further elucidated through NMR experiments using SUVs composed of DOPE:DOPS:DOPC in a 5:3:12 ratio, with a 1:25 ratio of aSyn to SUVs. 2D ^{1}H-^{15}N HSQC NMR spectra were recorded in the presence and absence of SUVs, and peak intensity ratios were compared (Figure 32 and Figure **33**). For details, see section 2.2.4.

For both WT and Y39E aSyn, 89% of the total population was found to be membrane-bound. The NAC region of WT aSyn was found predominantly in an associated state (72%), while Y39E aSyn showed 62% in an associated state and 27% in a dissociated state, corresponding to a 1.6-fold increase in the dissociated state compared to WT aSyn (Table 19).

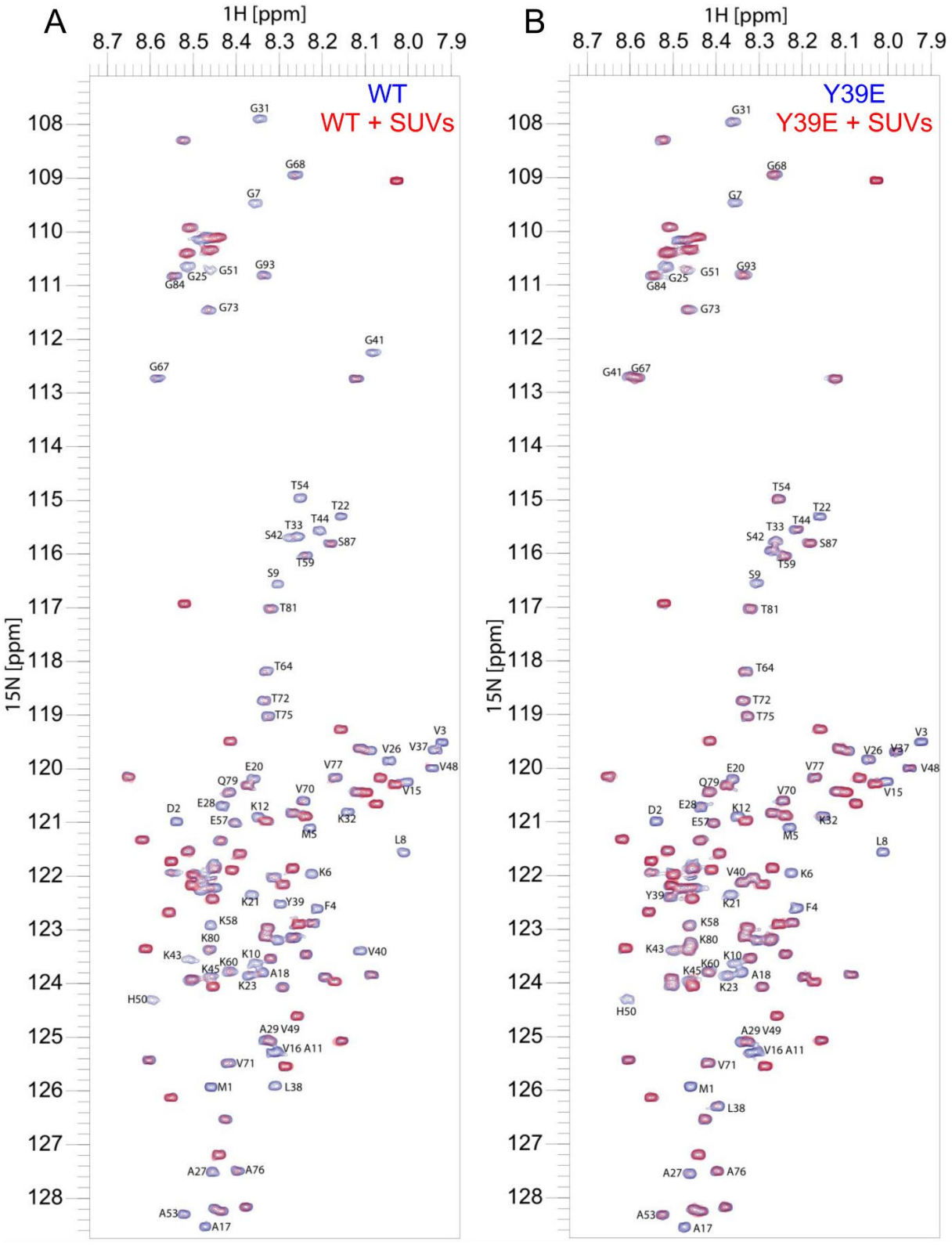

Figure 32: 2D ^{1}H-^{15}N HSQC NMR spectra of WT and Y39E aSyn in the presence of SUVs. (A) Overlay of 100 µM WT aSyn in absence (blue) and presence (red) of SUVs. (B) Overlay of 100 µM Y39E aSyn in absence (blue) and presence (red) of SUVs. (A,B) Spectra were obtained at 15 °C and 600 MHz with a 1:25 ratio of aSyn:SUVs. SUVs were constituted of DOPE:DOPS:DOPC (5:3:12) and aSyn dissolved in buffer MES.

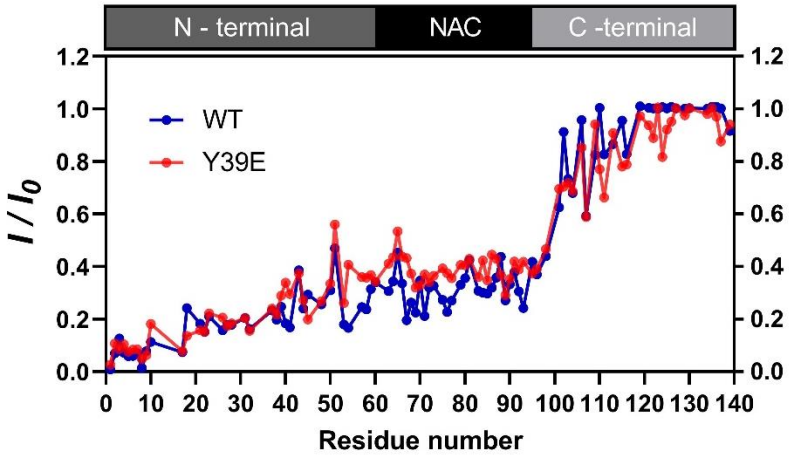

Figure 33: Structural characterization of 2D ^{1}H-^{15}N HSQC NMR spectra of WT and Y39E aSyn with SUVs. Peak intensity ratio (I/I_0) of WT (blue) and Y39E (red) aSyn (100 µM) plotted again the residue number. I and I_0 are the peak intensities of aSyn cross peaks observed in absence (I_0) and or presence (I) of SUVs. Spectra were obtained at 15 °C ad 600 MHz with a 1:25 ratio of aSyn:SUVs. SUVs were constituted of DOPE:DOPS:DOPC (5:3:12). aSyn was dissolved in buffer MES.

Table 19: Characterization of membrane binding by NMR. Parameters of peak intensity ratio of WT and Y39E aSyn, in presence (I) and absence (I_0) of SUVs are shown:

	Total bound	**Hidden**	**Exposed**	
	$1-\left(I/I_0\right)_{mean,3-25}$	$1-\left(I/I_0\right)_{mean,66-86}$	$Total\ bound-hidden$	Fold increase
WT	0.89	0.72	0.17	1
Y39E	0.89	0.62	0.27	1.6

3.2 *In vitro* Aggregation of Y39E aSyn

After characterizing the structural and dynamic properties of the monomeric state of both aSyn variants, the *in vitro* aggregation of WT and Y39E aSyn was compared. Firstly, the aggregation process was monitored by ^{1}H NMR experiments, and the final product of aggregation was investigated through ThT fluorescence assessment, CD spectroscopy, and SDS-PAGE. Additionally, the kinetics of the aggregation were analyzed through continuous ThT fluorescence measurements at different

concentrations, with in-depth evaluation of the final product of aggregation using CD spectroscopy, SEC, and SDS-PAGE.

3.2.1 Aggregation Assay Monitored by ^{1}H NMR Spectroscopy

To monitor the aggregation of aSyn, 50 µM WT or Y39E were incubated at 37 °C under stirring conditions and ^{1}H NMR spectra were acquired daily. Given the invisibility of large aggregates in liquid-state NMR under the experimental conditions, the reduction in signal corresponded to the decrease of free monomers during the aggregation process. The consumption of monomers was faster, and the signal reduction was more pronounced for WT than for Y39E aSyn (Figure 34A, B). The region between 0.8 and 0.6 ppm, corresponding to the aliphatic protein region, was integrated and the fraction of aggregated aSyn plotted against the time of aggregation. WT aSyn reached a plateau phase after 70 hours, whereas Y39E aSyn reached a plateau at approximately 100 hours of incubation time (Figure 34C). The percentage of monomers present at the end of the aggregation process was significantly lower for WT (13%) than for Y39E (22%, $p = 0.0155$), while the ThT fluorescence of the final product of aggregation was slightly higher for WT than for Y39E aSyn (Figure 34D, E).

The final product of aggregation was separated into supernatant and pellet for a more detailed assessment. CD spectroscopy revealed a random coil structure for both WT and Y39E aSyn monomers and the supernatant of both aggregation processes. The CD spectra of the pellet showed β-sheet structures, more pronounced for WT than for Y39E aSyn (Figure 34F). SDS-PAGE revealed a greater aSyn content in the pellet than in the supernatant for both WT and Y39E, with the Y39E aSyn supernatant band being stronger than the WT supernatant band. This was shown for two Y39E aSyn replicates (Figure 34G). In summary, the aggregation process of Y39E aSyn consumed fewer monomers than WT, confirmed by CD spectroscopy and SDS PAGE.

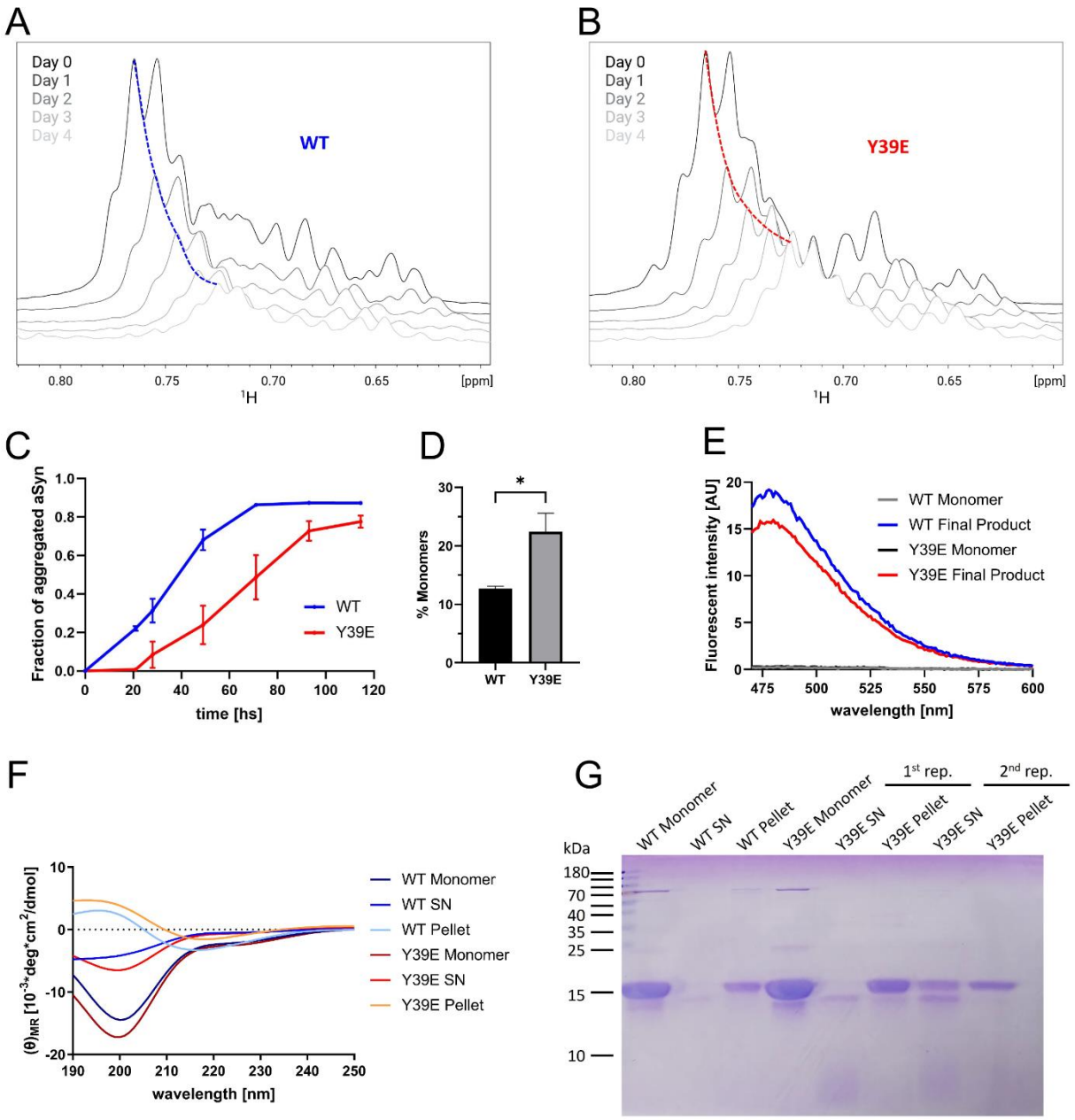

Figure 34: WT and Y39E aSyn aggregation *in vitro*. Representative ^{1}H NMR spectra recorded at 15 °C and 600 MHz of WT (A) and Y39E (B) aSyn in buffer MES at 5 subsequent days while incubating at 37 °C under stirring conditions. (C) Integration of spectra shown in (A) and (B) for WT (blue) and Y39E (red). Integrated area (0.8-0.6 ppm) was normalized to day 0 and plotted against the incubation time. (D) Percent of monomers present at the end of aggregation, quantified by integration of NMR spectra between 0.8 and 0.6 ppm, $p = 0.0155$ (unpaired, two-tailed t-test). (E) ThT fluorescence of monomers and final product of aggregation of WT (blue) and Y39E aSyn (red). (F) CD spectra of monomers (dark blue and dark red) and final product of aggregation separated into supernatant (blue and red) and pellet (light blue and light red) for WT and Y39E aSyn, respectively. (G) Coomassie-stained SDS-PAGE of monomers and final product of aggregation separated into supernatant and pellet for WT and Y39E aSyn (2 replicates).

3.2.2 Aggregation Kinetics Assessed by ThT Fluorescence

ThT fluorescence was monitored continuously throughout the aggregation process at 37 °C under shaking conditions using 50, 100, and 200 µM aSyn (Figure 35A, B). Kinetic parameters such as the half time of the aggregation process and the elongation factor were calculated as mentioned in section 2.2.1. The half time of aggregation maintained at 22 to 26 hours for all WT aSyn concentrations used, while for Y39E aSyn, it decreased concentration-dependent from 75 hours at 50 µM to 42 hours at 200 µM (Table 20). The elongation factor for all samples was 0.1-0.28 hours.

The final product of aggregation was in detail characterized by CD spectroscopy and SDS-PAGE, performed as for aggregation experiments monitored by NMR. The CD spectra showed random coil structures in monomers and the supernatants of both reactions, and a more pronounced β-sheet structure in the pellet of WT compared to Y39E aSyn (100 µM samples, Figure 36A). Monomers and the supernatant of the final product of aggregation were additionally accessed by SEC. Results indicated the absence of soluble oligomeric structures, with a higher reduction in signal for the supernatant of WT than for Y39E aSyn (Figure 36B). Coomassie-stained SDS-PAGE showed aSyn predominantly in the pellets of WT aSyn samples and to a lesser extent in the supernatant of the 200 µM sample. For Y39E aSyn, protein was detected in the supernatant of all samples (Figure 36C, D).

In conclusion, the kinetic parameters of the aggregation process for Y39E aSyn showed greater half times than WT aSyn while the elongation factor was comparable. Furthermore, Y39E aSyn, in contrast to WT, showed a concentration dependency, with greater half times at lower concentrations. The reduced monomer consumption of Y39E aSyn, observed in ^{1}H NMR aggregation experiments (Figure 34), could also be seen in continuous ThT fluorescence measurements by investigating the final product of aggregation using CD spectroscopy, SEC and SDS-PAGE (Figure 36).

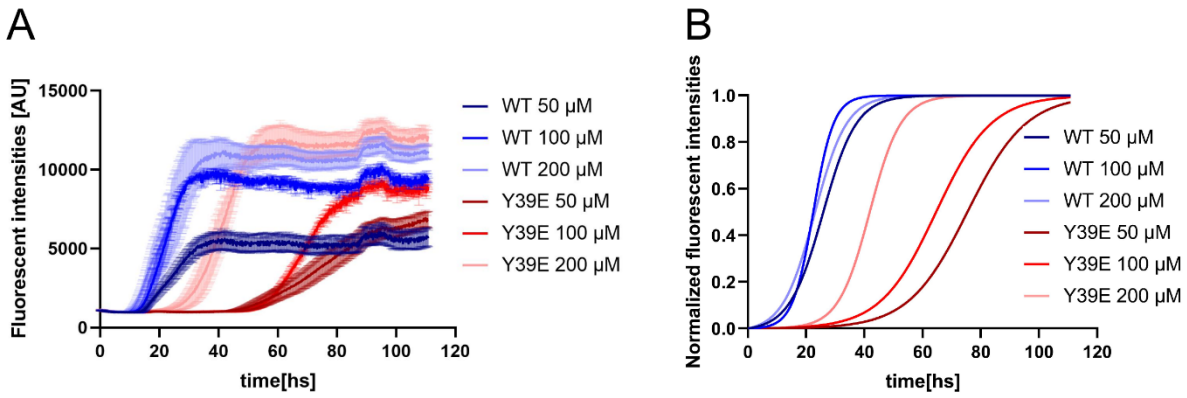

Figure 35: Kinetics of WT and Y39E aSyn aggregation *in vitro*. (A) Raw data of ThT fluorescence monitored throughout the aggregation process at 37 °C under shaking conditions for WT (blue) and Y39E (red) aSyn, 50, 100 and 200 µM each. (B) Normalized ThT fluorescence of (A).

Table 20: Kinetic parameters of WT and Y39E aSyn aggregation *in vitro*. The half time and elongation factor of aSyn aggregation, measured by ThT fluorescence, visualized in Figure 35 B, are listed.

	WT			**Y39E**		
	50 µM	100 µM	200 µM	50 µM	100 µM	200 µM
Elongation factor [hs]	0.17	0.28	0.18	0.10	0.11	0.19
$t_{1/2}$ [hs]	26	22	23	75	65	42

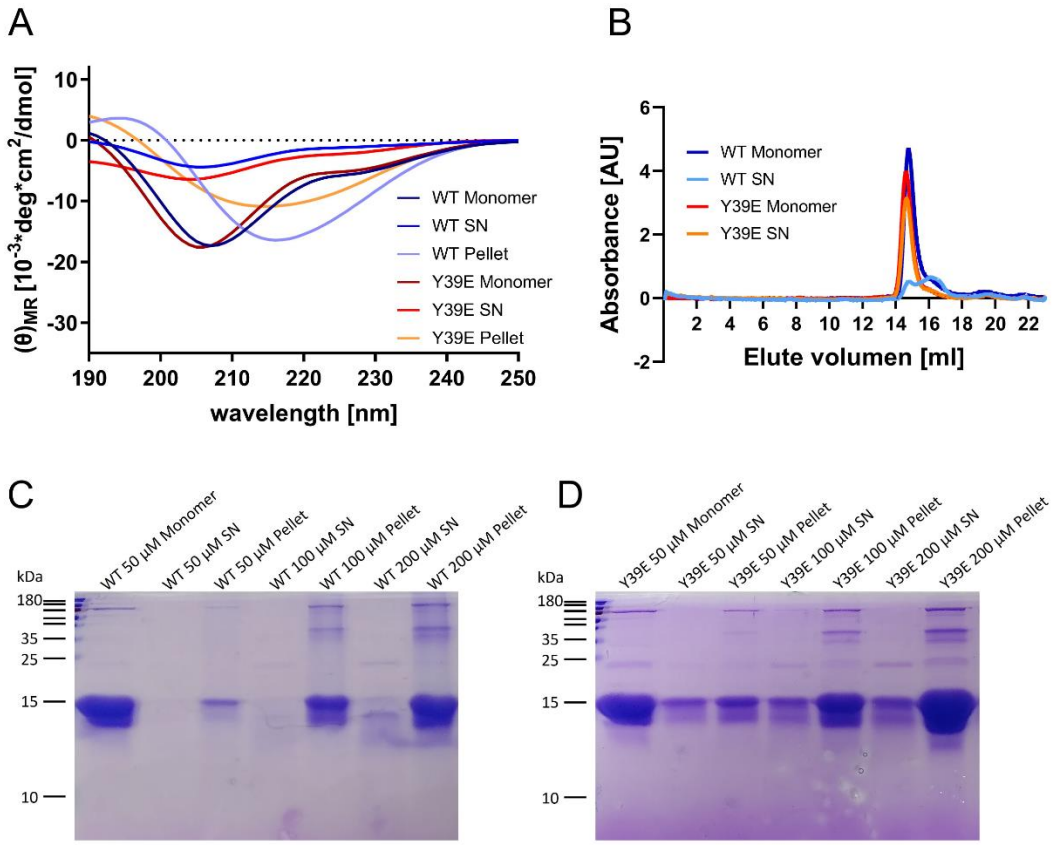

Figure 36: Analysis of the final product of aggregation of WT and Y39E aSyn. (A) CD spectra of monomers (dark blue and dark red) and final product of aggregation (100 µM sample in Figure 35) separated into supernatant (blue and red) and pellet (light blue and light red) for WT and Y39E aSyn, respectively. (B) SEC of 50 µM monomers and supernatant of final product of aggregation (50 µM sample shown in Figure 35) of WT (dark and light blue) and Y39E (red and orange) aSyn. (C,D) Coomassie-stained SDS-PAGE of monomers and final product of aggregation separated into supernatant and pellet for WT (C) and Y39E (D) aSyn.

3.3 Aggregation of Y39E aSyn in Cellular Models

In addition to the *in vitro* characterization of the Y39E mutant, its aggregation, neurodegeneration and toxicity were investigated in cellular and animal models. Initially, the aggregation in neuroglioma H4 cells and in the neuronal cells of *C. elegans* was addressed. To quantify aSyn aggregations in H4 cells, the aSyn-SynT/Synphilin-1 model was employed (for details, see section 2.3.3). H4 cells were co-transfected with WT or Y39E aSyn-SynT and Synphilin-1 to enhance aSyn aggregation. Cellular inclusions were predominantly present in WT aSyn-transfected cells, with an average of 6 inclusions per cell, whereas Y39E aSyn expression led to an average of 2 inclusions per cell. The difference in the number of inclusions per cell

was significantly reduced for Y39E aSyn ($p < 0.0001$), while the expression levels of WT and Y39E aSyn within each replicate were comparable (Figure 37).

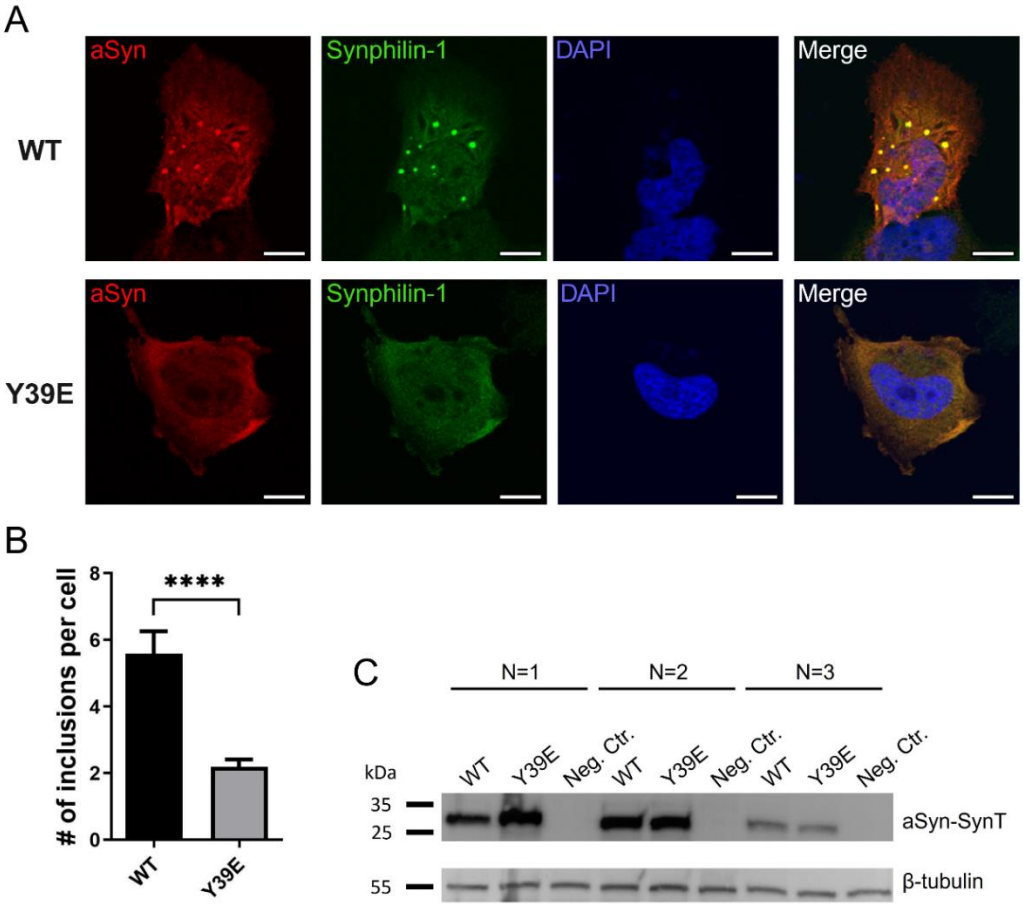

Figure 37: aSyn-SynT/Synphilin-1 aggregation model in H4 cells. (A) Confocal microscopy images of H4 cells expressing WT or Y39E aSyn-SynT and Synphlin-1**.** Immunofluorescent staining of aSyn (red), Synphilin-1 (green) and the nucleus (DAPI, blue), scale bar represents 10 µM. (B) Quantification of cellular inclusions in H4 cells expressing WT or Y39E aSyn-SynT, $p < 0.0001$ (Mann-Whitney test). (C) Western blot of three replicates of aSyn-SynT/Synphilin-1 co-transfected H4 cells.

Next, the aggregation of WT and Y39E aSyn was investigated in the model organism *C. elegans*. To enable the visualization of aSyn within the living animal, aSyn was fused C-terminally to the fluorescent protein mCherry. Tissue specificity was achieved by expressing aSyn under control of the pan-neuronal promoter *rab3*, leading to aSyn expression in neuronal cells of *C. elegans*. For both, WT and Y39E aSyn expression, round-shaped aggregates were detected (Figure 38A). The number of aggregates was significantly reduced when expressing Y39E aSyn ($p = 0.0458$) and aggregates were smaller in size (Figure 38C, D). Furthermore, the aggregate area per cell was significantly reduced considering Y39E aSyn in comparison to WT

($p < 0.0001$), while the aSyn expression levels of all analyzed WT and Y39E strains were comparable, as shown by western blotting (Figure 38B, E).

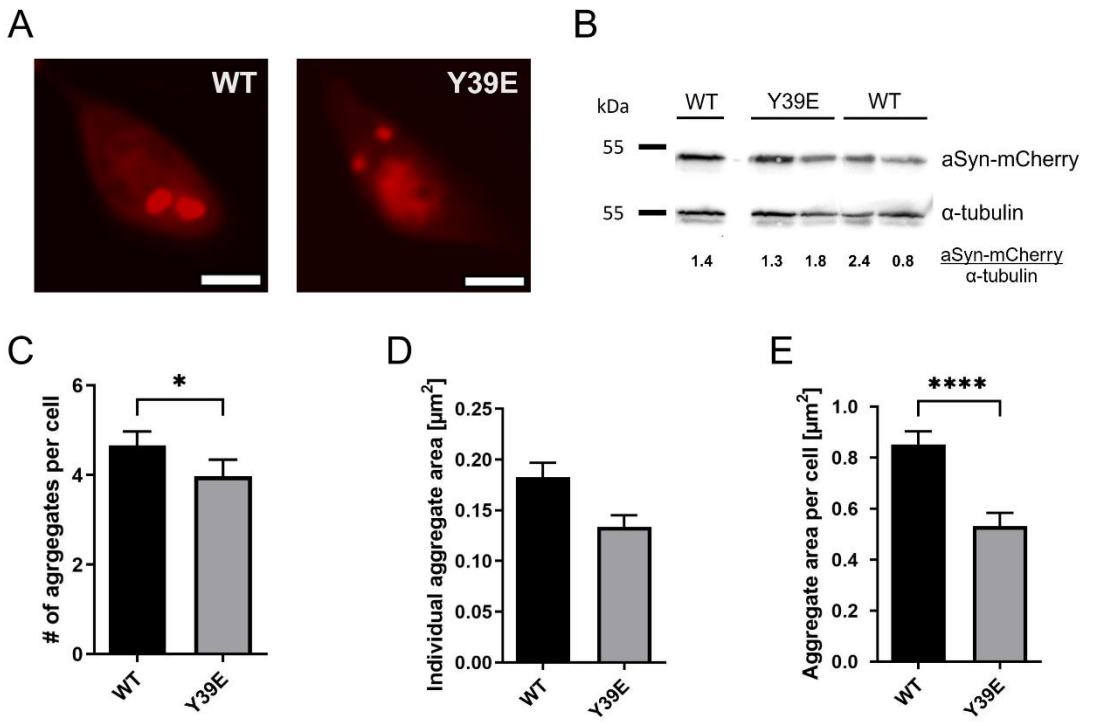

Figure 38: Aggregation of WT and Y39E aSyn in pan-neuronal cells of *C. elegans*. (A) Confocal microscopy images of WT and Y39E aSyn, fused C-terminally to mCherry, expressed under the control of the pan-neuronal promoter *rab3.* Scale bar represents 2 µm. (B) Western blot of *C. elegans* strains expressing WT or Y39E aSyn in pan-neuronal cells included in the study. (C) Quantification of the number of cellular aggregates within cell bodies. At least 40 cells per genotype were analyzed, $p = 0.0458$ (Mann-Whitney test). (D) Quantification of the individual aggregate area. A minimum of 159 cells per genotype were analyzed. (E) Comparison of the aggregate area per cell of WT and Y39E-expressing neurons. At least 40 cells per genotype were analyzed, $p < 0.0001$ (Mann-Whitney test).

In summary, the aggregation of Y39E aSyn in neuroglioma H4 cells and in neuronal cells of C. elegans led to fewer and smaller aggregates located in cellular inclusions.

3.4 Neurodegeneration and Toxicity of Y39E aSyn

To address the neurodegeneration caused by the Y39E mutant, the animal model *C. elegans* was used. Neurodegeneration was assessed in the dopaminergic neuronal system, while toxicity was evaluated by visualizing mitochondria in muscular tissue.

Furthermore, toxicity was investigated in the neuroblastoma cell line SH-SY5Y by measuring the mitochondrial activity, thus observing the cell survival.

3.4.1 Degeneration of Dopaminergic Neurons in *C. elegans*

The dopaminergic system of *C. elegans* comprises 8 neurons, of which 6 are located in the head region. The 4 CEPs have dendritic projections extending until the mouth of the animal, allowing the evaluation of neurodegeneration. In healthy individuals, all 4 projections can be visualized evenly. The first sign of degeneration is punctual thickening of the dendrite (blebs). Increased neurodegeneration is marked by breaks within the dendritic projections, where subsequent blebs lose their connection to one another (broken dendrite). The final step of neurodegeneration is characterized by the absence of the dendrite (missing dendrite, Figure 39).

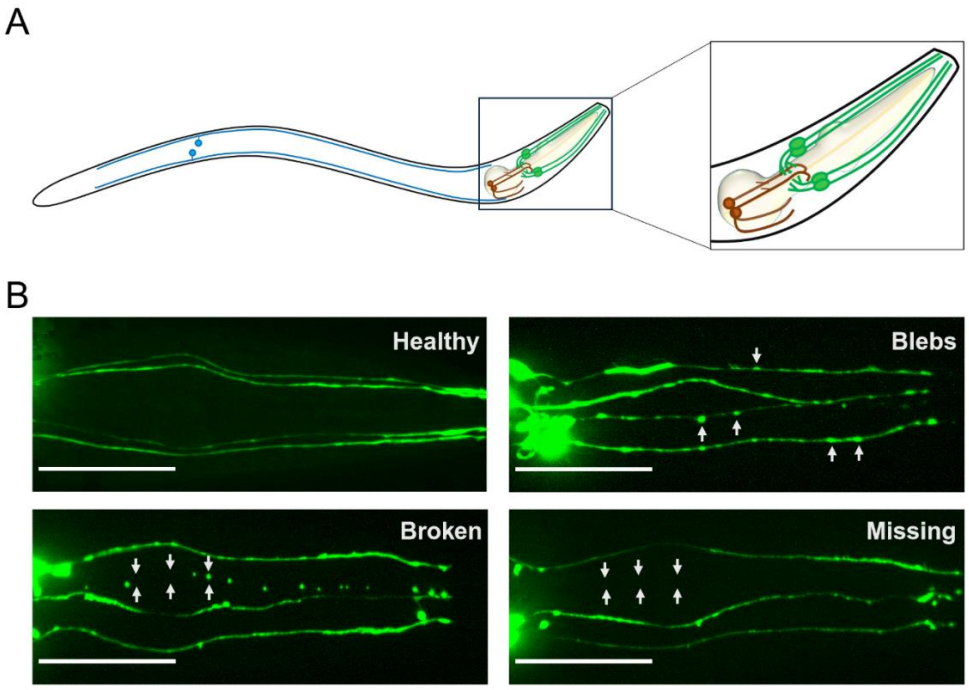

Figure 39: Neurodegeneration of dopaminergic neurons in *C. elegans*. (A) Representation of the dopaminergic neurons of *C. elegans*, including 4 CEPs (green), 2 ADEs (brown), and 2 PDEs (blue). (B) Classification of neurodegeneration, ranging from a healthy phenotype to the presence of blebs, broken and missing dendrites of CEPs. Scale bar represents 50 µm.

To evaluate the effects of Y39E aSyn on dopaminergic neurodegeneration, WT or Y39E aSyn, fused C-terminally to YFP, was expressed under the control of the *dat1* promoter, achieving tissue-specific expression in dopaminergic neurons. Furthermore, animals underwent 6OHDA treatment to achieve a sensitized background (see details in section 2.4.5). Confocal images of WT and Y39E expressing strains showed increased neurodegeneration caused by the Y39E mutant, while the expression levels of the strains included in the study were comparable (Figure 40A-C). Dendrites were then classified according to their phenotype as healthy, blebs, broken or missing. Control strains expressing GFP but not aSyn in dopaminergic neurons, exhibited predominantly a healthy phenotype. The percentage of blebs increased slightly upon 6OHDA treatment, representing the sensitized background. Animals lacking the dat1 transporter (dat1KO), and thus being inefficient in the uptake of 6OHDA into dopaminergic cells, did not show a response to the treatment. The expression of aSyn led to a neurodegenerative phenotype, which was more pronounced for the Y39E mutant than for WT aSyn (Figure 40D).

To evaluate neurodegeneration differences statistically, each animal was assigned a score depending on the phenotype of the 4 CEPs. Healthy dendrites were rated with 1, blebs with 2, broken with 3 and missing dendrites with 4. The score was calculated as the sum of the 4 rated CEPs. For an animal showing 1 healthy, 2 broken and 1 missing dendrite, the score would be 1x1 + 2x3 + 1x4 = 11. The average score for control animals was 5.1, which increased upon 6OHDA treatment to an average score of 5.8 but was found unaffected for dat1KO animals. The expression of aSyn led to a significantly increased score (WT: 7.1, $p < 0.0001$; Y39E: 8.4, $p = 0.0002$), with a direct comparison of WT and Y39E aSyn revealing significantly elevated neurodegeneration caused by the Y39E mutant ($p = 0.004$, Figure 40E).

As the dopaminergic neuronal system of *C. elegans* is mechanosensitive, its function encompasses the detection of food sources. To linger in areas with food supply, healthy animals exhibit a food-induced slowing response[260]. With increased neurodegeneration of dopaminergic neurons, individuals lose the ability to detect food sources and thus lack a food-induced slowing response. To assess the impact of neurodegeneration on the animal's behavior, GFP, WT or Y39E aSyn expressing animals were subjected to behavioral assay. A food-induced slowing response was

detected for GFP and WT aSyn-expressing animals, where the counted body bends per minute were significantly less in the presence of food ($p < 0.0001$ (GFP), $p = 0.0004$ (WT)). Individuals expressing Y39E aSyn, however, exhibited the same crawling speed on and off food ($p = 0.9527$, Figure 40F).

In summary, aSyn expression resulted in increased neurodegeneration. Y39E aSyn expression induced hereby greater neurodegeneration than WT expression, reaching a level of severity that caused a loss of function of dopaminergic neurons, consequently impairing the nematode's behavior.

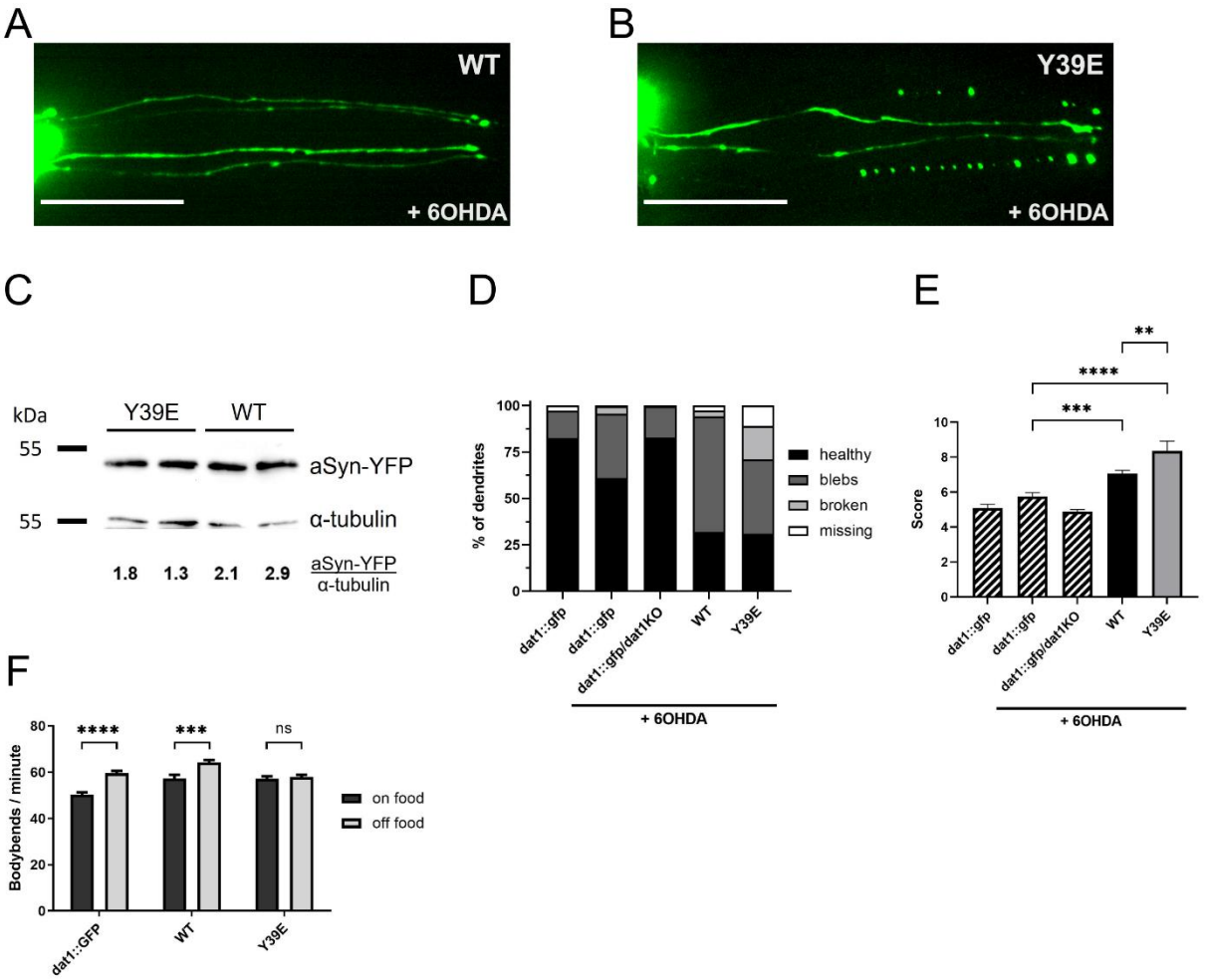

Figure 40: Dopaminergic neurodegeneration in *C. elegans* of WT and Y39E aSyn. (A, B) Confocal microscopy images of WT (A) or Y39E aSyn (B), fused C-terminally to YFP, expressed under the control of the *dat1* promoter. Scale bar represents 50 µm. (C) Western blot of *C. elegans* strains expressing WT or Y39E aSyn in dopaminergic neurons included in the study. (D) Categorization of dendrites according to their phenotype. (E) Scoring of animals according to the phenotype of their CEPs ($Score = (\#healthy * 1 + \#blebs * 2 + \#broken * 3 + \#missing * 4)$. A minimum of 25 individuals per group was analyzed, **p = 0.004 (One-way ANOVA), ***p = 0.0002 (One-way ANOVA), ****$p < 0.0001$ (One-way ANOVA). (F) Body bends per minute of *C. elegans* expressing GFP, WT or Y39E aSyn, fused C-terminally to YFP, in presence and absence of food. A minimum of 37 individuals per genotype and condition was analyzed, ns: p = 0.5897 (unpaired, two-tailed t-test), ***p = 0.0004 (unpaired, two-tailed t-test), ****$p < 0.0001$ (unpaired, two-tailed t-test).

3.4.1 Mitochondria-Mediated Toxicity

To investigate the cause of toxicity, mitochondria were evaluated in cell-based and animal-based models. SH-SY5Y cells were treated with WT or Y39E aSyn monomers, the final product of aggregation monitored by NMR, or buffer MES, medium only or SDS as control. Healthy, living cells convert MTT by the mitochondrial enzyme succinate dehydrogenase to purple formazan crystals, which can be quantified spectrophotometrically. The normalized absorbance is thereby proportionate to the number of metabolically active, living cells[278].

Treatment of SH-SY5Y cells with buffer MES or monomers of WT or Y39E aSyn did not reduce cell survival, whereas treatment with SDS led to 90% of cells being dead. The final product of aggregation led to a decrease in cell survival to approximately 35% (WT) or 44% (Y39E, Figure 41A). There was no significant difference found between the toxicity generated by WT and Y39E aSyn.

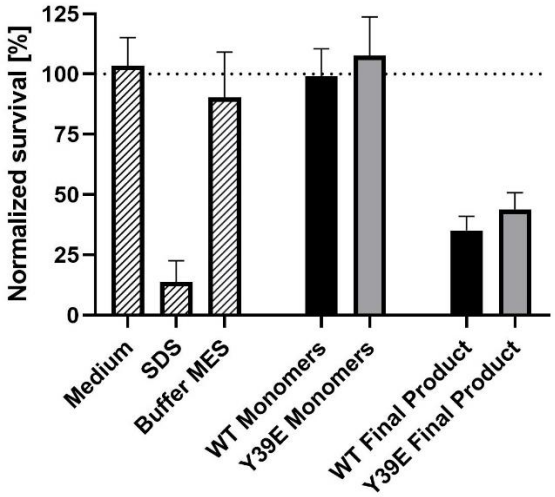

Figure 41: MTT toxicity of WT and Y39E aSyn aggregates in SH-SY5Y cells. SH-SY5Y cells were treated with buffer MES, medium or 0.1% SDS as controls, or with 1 µM WT or Y39E aSyn monomers or the final product of aggregation. MTT conversion by mitochondrial enzymes to purple formazan was detected by measuring the absorbance at 570 nm. Normalized cell survival es is shown.

The phenotype of mitochondria was additionally assessed in the muscular tissue of *C. elegans*. Therefore, aSyn, fused C-terminally to YFP, was expressed under the control of the *myo3* promoter. To visualize the mitochondria, the transmembrane domain of TOM70, a mitochondrial transmembrane protein, was fused to mCherry and expressed in muscle tissue. Healthy animals display a network structure of

mitochondria, where the organelles are organized in a dynamic network. Upon stress, mitochondria appear oval-shaped and less connected. Enhanced cellular toxicity leads to round-shaped mitochondria, lacking connections.

Confocal images of the muscular tissue of *C. elegans* showed a network structure of mitochondria in control stains lacking aSyn for 60% of the population, while about 40% exhibited an oval phenotype. The expression of WT aSyn shifted the phenotype to almost 80% round-shaped mitochondria and 20% oval shaped. Y39E aSyn expression led to 10% network structure, 50% oval and 40% round-shaped mitochondria (Figure 42A, C).

Next, a scoring system, similar to the scoring of degeneration in dopaminergic neurons, was implemented. A network structure was assigned with the value 1, while oval-shaped mitochondria were rated with 2 and round-shaped mitochondria with 3. The average score of control strains was 1.5. The score for WT aSyn (2.7) was significantly higher than that for Y39E aSyn (2.2, $p = 0.0378$, Figure 42D), even though the expression levels, evaluated by western blotting, revealed a greater expression level of Y39E aSyn in comparison to WT (Figure 42B).

In conclusion, aSyn expression or treatment of cells with the product of aggregation resulted in increased toxicity and an impaired mitochondrial phenotype for both, WT and Y39E aSyn. Nevertheless, Y39E aSyn, in comparison to WT, even though it did not alter the cell survival in the MTT-based assay, its expression led to a healthier mitochondrial phenotype in the muscle tissue of *C. elegans*. The toxicity causing the elevated neurodegeneration observed for Y39E aSyn is therefore unlikely to be mediated by mitochondrial pathways.

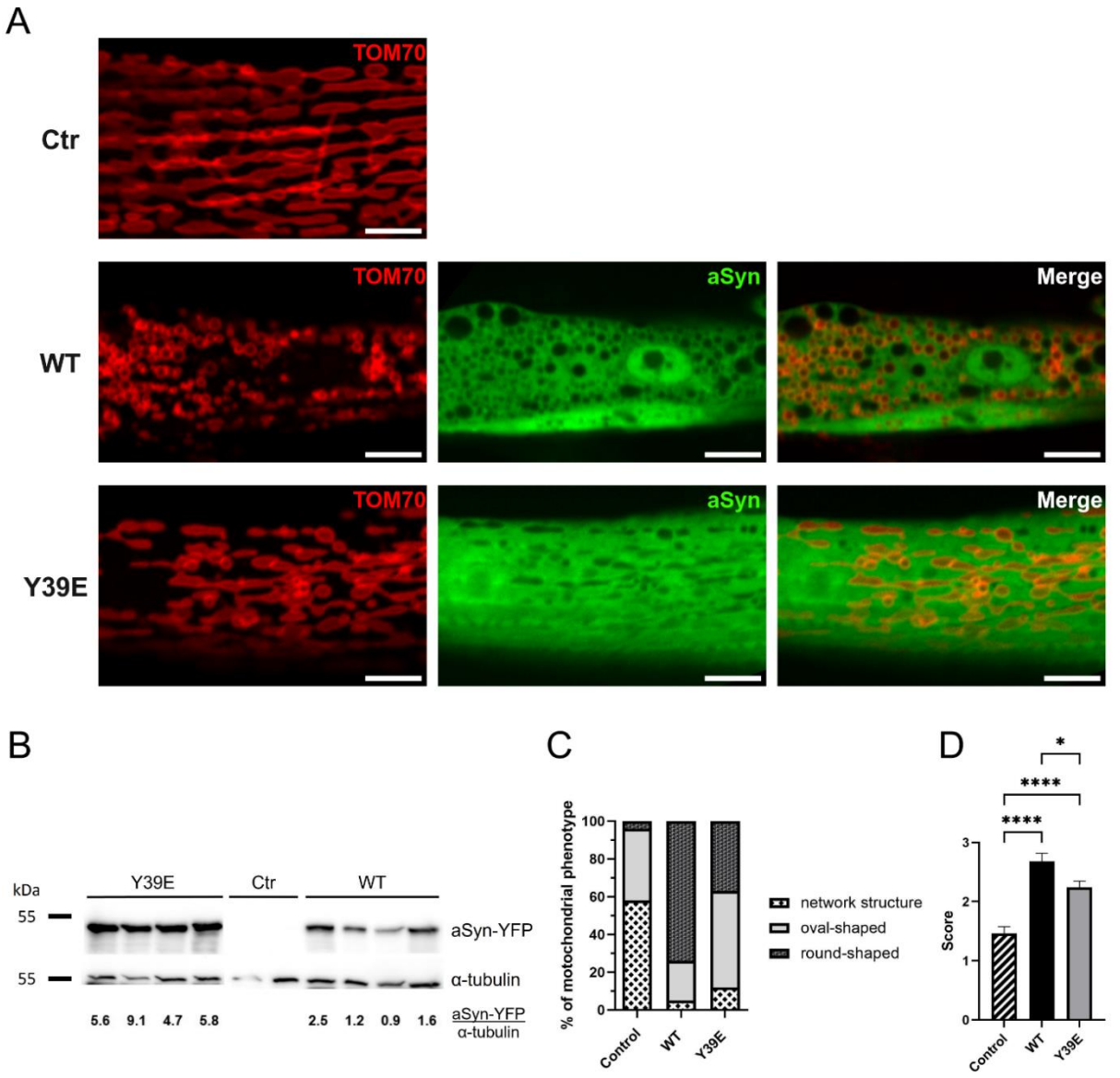

Figure 42: Mitochondria in muscle tissue of *C. elegans* expressing WT or Y39E aSyn. (A) Confocal microscopy images of body wall muscles expressing WT (A) or Y39E aSyn (B), fused C-terminally to YFP, under the control of the *myo3* promoter. Mitochondria are visualized by expressing TOM70-mCherry. Scale bar represents 5 µm. (B) Western blot of *C. elegans* strains expressing TOM70-mCherry, WT or Y39E aSyn in body wall muscles included in the study. (D) Categorization of mitochondria according to their phenotype. (E) Scoring of individuals according to their mitochondrial phenotype (network structure = 1, oval-shaped = 2, round-shaped = 3). A minimum of 19 individuals per group was analyzed, *p = 0.0378 (One-way ANOVA), ****p < 0.0001 (One-way ANOVA).

4 Discussion

Numerous research groups have investigated the role of modified aSyn as a contributing factor to PD. Traditionally, attention was restricted to familial mutations and gene multiplications; however, PTMs, particularly phosphorylation, have recently emerged as influential contributors to altered protein pathology. PTMs have for instance found to be able to modulate the interplay with membranes[234]. Phosphorylation, a prevalent PTM in eukaryotic proteins, frequently serves as a molecular switch regulating protein interactions[287]. The dysregulation of protein phosphorylation has implications for various diseases, with kinases becoming prominent targets for pharmaceutical interventions, particularly in cancer research[288,289].

aSyn undergoes phosphorylation at various sites, with the kinase c-abl notably phosphorylating aSyn primarily at position Y39[192]. Activation of c-abl has been observed in patients' brains of advanced stages of PD, correlating with increased phosphorylation levels of aSyn[246]. Conversely, aSyn overexpression also upregulates c-abl protein levels, creating a reciprocal regulatory relationship[192]. Furthermore, phosphorylation at Y39 is believed to enhance aSyn toxicity[246,290].

In this study, the phosphomimetic mutant Y39E was characterized to elucidate the impact of phosphorylation at this site. The investigation encompassed the structural and dynamic analysis of Y39E aSyn as a monomer, its interaction with membranes, and its aggregation properties both *in vitro* and *in vivo*, exploring subsequent effects on neurodegeneration and toxicity. Notably, the Y39E mutant did not alter the monomeric structure or dynamics compared to WT aSyn, while the membrane binding affinity for the NAC region slightly decreased. Y39E aSyn exhibited concentration-dependent aggregation kinetics, with a prolonged lag phase in comparison to WT aSyn. Despite of forming smaller aggregates *in vivo*, Y39E aSyn-induced dopaminergic neurodegeneration was elevated, while mitochondrial pathways were ruled out as the cause of increased toxicity.

4.1 Structural and Dynamic Properties of Monomeric Y39E aSyn

In analyzing the structure of the Y39E monomer, no discernible distinctions from the WT aSyn counterpart were observed. An analysis of 2D ^{1}H-^{15}N HSCQ NMR spectra revealed that chemical shift differences were confined to the vicinity of position 39 (Figure 26), aligning with findings reported by Dikiy *et al*. (2016)[290]. The measured $^{3}J_{HN\text{-}H\alpha}$ coupling constants, ranging between 6 and 8 Hz for both WT and Y39E aSyn, underscored the intrinsically disordered and unstructured nature of the protein (Figure 27), which could be confirmed by CD measurements of aSyn monomers (Figure 34 and Figure **35**).

While assessing the backbone dynamics of the Y39E monomer, minor distinctions from the WT monomer were observed. Longitudinal relaxation rates (R_1) of amide groups exhibited comparability, whereas R_2 relaxation rates were slightly elevated for Y39E (Figure 28A and B).

Exploration of the network of transient long-range interactions was facilitated by introducing the paramagnetic probe MTSL at positions 18 and 90. Both WT and Y39E aSyn manifested transient long-range interactions between the C-terminus (MTSL at position 18) and the N-terminal region of the protein (Figure 29). The late NAC region (MTSL at position 90) of both WT and Y39E interacted with the C-terminus. Notably, the WT C-terminus exhibited additional transient interactions with the region 35-65 (Figure 30). This additional transient long-range interaction however was not affecting the hydrodynamic radius, which was comparable between WT and Y39E aSyn (Table **17**).

4.2 Membrane Binding Features of Y39E aSyn

In-depth exploration of the membrane binding properties of Y39E aSyn revealed no distinctions from WT concerning overall affinity to DOPE:DOPS:DOPC (5:3:2) SUVs, with comparable K_d values (Figure 31 and Table 18). The number of lipids interacting with aSyn was slightly elevated for Y39E aSyn, indicating that the mutant interacts with a higher number of membranes simultaneously (Table 18). A more detailed

investigation of DOPE:DOPS:DOPC (5:3:12) SUVs using NMR unveiled that Y39E aSyn exhibits an elevated binding propensity in a dissociated state compared to WT aSyn (Figure 33). Similar findings for the Y39E mutant were reported by Dikiy *et al*. (2016), demonstrating reduced binding beyond the mutation site, extending through the helix-2 region[290]. Notably, the introduction of a charge by tyrosine to glutamate mutation at position 39, crucial for membrane interaction, resulted in only slight differences in membrane binding, unlike other mutations that lead to more pronounced alterations[219,220]. This discrepancy might be attributed to the position of residue 39 in the membrane-bound helical aSyn structure. Illustration of the α-helix composed of residues 23 to 66 in Figure 43, emphasizes that one side of the helix predominantly consists of non-polar amino acids, while the other side, facing away from the membrane upon interaction, comprises numerous charged lysine and glutamate residues[220,273]. The position of Y39 on the charged side of the helix suggests a comparatively weaker impact on membrane interaction upon the introduction of a charged amino acid at this position, compared to introducing a charged amino acid at the side facing the membrane.

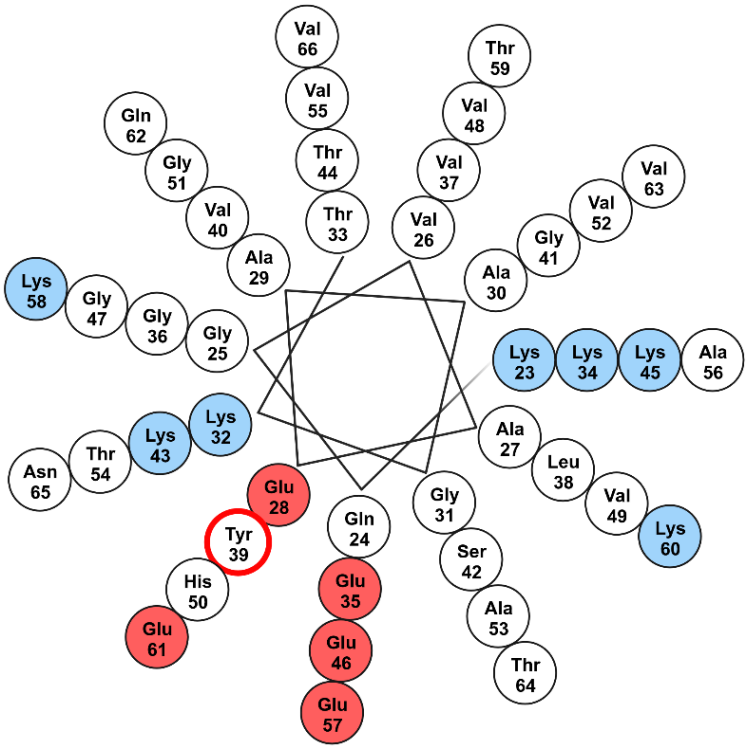

Figure 43: Helical wheel plot of membrane-bound aSyn helix. The residues 23 to 66 of the membrane-bound aSyn organize in an amphipathic α11/3 helix. The position 39 is encircled in red, basic residues are depicted in blue, acidic residues in red. Adopted from Ysselstein *et al.* (2015)[220].

4.3 Aggregation of Y39E aSyn

The aggregation of Y39E aSyn was investigated through diverse methodologies. NMR experiments tracking the aggregation process enables the quantification of monomer consumption. Y39E aSyn exhibited reduced monomer consumption throughout the aggregation process, as illustrated in Figure 34A-D. This observation was confirmed by CD and SEC measurements, along with SDS-PAGE analysis (Figure 34F, G and Figure 35D-G).

Assessment of the aggregation kinetics via continuous ThT fluorescence measurements unveiled a concentration-dependent pattern unique to the Y39E mutant, contrasting with other aSyn mutations. The half time of aggregation decreased from 75 hours at 50 µM to 42 hours at 200 µM Y39E aSyn, while WT aSyn displayed a consistent half time range of 22 to 26 hours across all concentrations. The comparable elongation factor between Y39E and WT aSyn, coupled with the lack of concentration dependency of WT aSyn aggregation, suggests that the differences in half time could be attributed to the prolonged lag phase of the Y39E mutant (Figure 35C). Experimental validation of the concentration dependency of Y39E aSyn aggregation was supported by collaborative investigations by Dr. Phelippe do Carmo Gonçalves, who explored WT aSyn in conjunction with PcTS. PcTS-dependent inhibition of amyloid fibril growth is facilitated by its interaction with residue Y39[243]. Continuous ThT fluorescence measurements of WT aSyn in conjunction with PcTS showed the same concentration dependency: Increasing PcTS concentration resulted in a prolonged half time of aggregation (Figure 44; Personal communication, unpublished results). Furthermore, Pan *et al.* (2020) reported a significant increase, up to four times, in the half time of aggregation when utilizing Y39E aSyn compared to WT aSyn (100 µM)[291].

As the structural and dynamical properties and thereby the intramolecular interactions of WT and Y39E aSyn were found comparable, the concentration dependent, prolonged lag time of Y39E aSyn aggregation is most likely due to impaired intermolecular interactions. The Y39E mutation leads to an inhibition of monomer assembly, which is essential to form aggregation prone nuclei and oligomers. This theory is supported by the binding of the amyloid formation inhibitor

PcTS to this position, which hinders fibril formation by stabilizing monomers and non-aggregating helical oligomers[243,292].

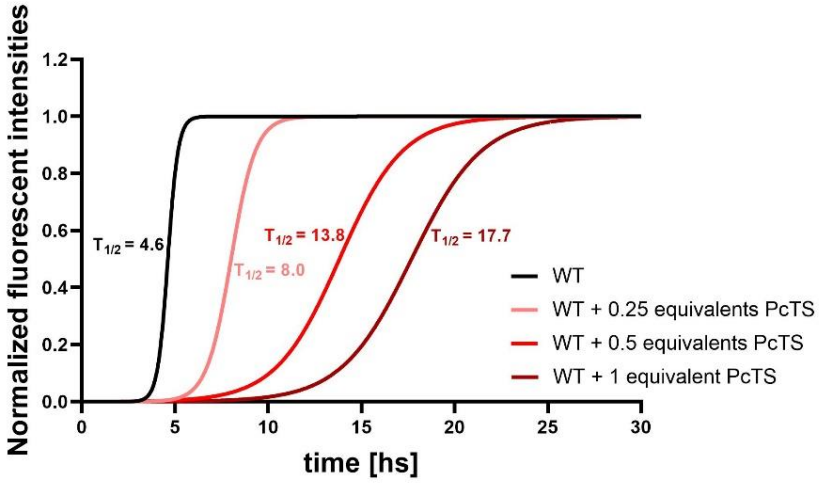

Figure 44: Aggregation kinetics of WT aSyn with the small-molecule PcTS. WT aSyn (100 µM) was incubated at 37 °C with agitation and 0, 0.25, 0.5 or 1 equivalent of PcTS, along with ThT to detect fibril growth. Unpublished data kindly provided by Dr. Phelippe do Carmo Gonçalves.

While NMR measurements and control experiments indicated a reduced monomer consumption for Y39E aSyn, continuous ThT fluorescence measurements reached comparable plateaus for both WT and Y39E aSyn indicating similar amounts of amyloid fibrils (Figure 35A). This unexpected result raises caution and may be related to distinct polymorphs formed by WT or Y39E aSyn. ThT, known to alter the fibril structure and increase fibrillization rates when present throughout aggregation, may not be entirely reliable for quantifications, as it binds differently to distinct polymorphs[188–190,293]. Alternative dyes such as Congo Red or DMASEBT might offer more reliable quantification of fibrillar content[294,295]. Indeed, Pan *et al.* (2020) have seen Y39E aSyn reaching a lower plateau than WT aSyn when using Congo Red[291].

In vivo, Y39E aSyn expression led to fewer cellular inclusions in H4 cells, in line to the effect observed for WT aSyn + PcTS treatment (Figure 37)[296]. This outcome was consistent with the investigations using the *C. elegans* animal model, where the expression of Y39E aSyn led to smaller and fewer aggregates (Figure 38). Zhang *et al.* (2023) reported similar effects using the Y39E aSyn mutant, noting a reduction in the prolongation of aSyn seeds originating from LBs when transduced into HEK293 cells expressing the Y39E mutant[297].

This effect could potentially be mediated by molecular chaperones. A recognized canonical motif comprising the N-terminus and a segment around Y39 in aSyn is recognized by diverse molecular chaperones, hindering aSyn aggregation upon interaction with the protein[245].

4.4 Neurodegeneration and Toxicity of Y39E aSyn

The impact of the Y39E mutant on neurodegeneration and toxicity was evaluated in the *C. elegans* animal model, where aSyn expression was confined exclusively to dopaminergic neurons. Both WT and Y39E aSyn expression resulted in a pathological phenotype, with the effects more pronounced for Y39E aSyn. The neurodegeneration induced by the mutant, but not by WT aSyn, significantly affected the nematode's behavior. The food-induced slowing response mediated by dopaminergic neurons was diminished, underscoring the impairment of the functionality of dopaminergic neurons caused by the Y39E mutant (Figure 40).

Importantly, the observed toxicity was not attributed to mitochondrial dysfunction. Even though WT and Y39E aSyn demonstrated a comparable level of toxicity in cellular toxicity assays involving mitochondrial enzymes, the pathological phenotype of mitochondria in the muscle tissue of *C. elegans* expressing aSyn was more prominent for WT than for Y39E aSyn (Figure 41 and Figure 42). The potential protective effect of mitochondria conferred by the Y39E mutant might be associated with its differences in interacting with membranes. Previous findings indicate that mitochondrial lipids trigger oligomerization, leading to the accumulation of reactive oxygen species and permeabilization of the mitochondrial membrane[201]. The introduction of a negative charge at this position might lead to less interactions with the mitochondrial membrane, making Y39E aSyn less prone to oligomerize thus less toxic in this context. To validate this hypothesis, it is imperative to perform membrane binding assays of aSyn with membranes that mimic the composition of the mitochondrial membrane.

In addition to Y39E aSyn, increased toxicity could also be linked to phosphorylation at Y39. aSyn expression activates c-abl, and increased c-abl expression in turn

elevates aSyn levels in mice[298]. Brahmachari *et al.* (2016) established a strong correlation between c-abl activation and disease progression in mice. Overexpression of a constitutively active form of c-abl induced dopaminergic neurodegeneration, while c-abl knockout significantly reduced pathology[246]. Moreover, inhibiting the phosphorylation of aSyn at position 39 by c-abl resulted in increased aSyn degradation[290]. This effect was demonstrated by using the c-abl inhibitor Nilotinib, where inhibition of c-abl enhanced aSyn clearance via the autophagic pathway[298]. These findings were supported by Mahul-Mellier *et al*. (2014), who illustrated that c-abl-mediated phosphorylation of aSyn protects against its degradation through the autophagic and proteasomal pathways in cortical neurons[247].

4.5 Y39E as a Phosphomimetic Mutant in aSyn

Given the focus of this study on the phosphomimetic mutant Y39E aSyn, this section discusses a comparison with pY39 aSyn. Expressing pY39 in large quantities exhibits challenges, such as potential dephosphorylation during protein expression in bacterial systems or phosphorylation of other residues when co-expressed with kinases. To circumvent these obstacles, pY39 can be expressed using unnatural amino acids coding for a stable pTyr analogue, where the phosphate group is shielded from hydrolysis and can be converted into native pTyr by a pH shift[299,300].

Several research groups have successfully employed such methods. Pan *et al.* (2021) and Dikiy *et al.* (2016) analyzed 2D HSQC NMR spectra of pY39 and reported only local chemical shifts around residue 39, akin to observations for the Y39E mutant in this study[290,301]. CD spectra of WT and pY39 aSyn were indistinguishable, displaying random coil patterns, indicating that pY39, like Y39E aSyn, does not have a substantial impact on the global secondary structure of aSyn[290]. This aligns with findings from other research groups, confirming the similarity of monomeric structures of WT and pY39 aSyn[291].

Similar to WT and Y39E aSyn, pY39 aSyn adopts helical structures upon binding to detergent micelles or highly negatively charged lipids. Moreover, the binding of pY39

aSyn to SDS micelles resembled that of Y39E aSyn, where the N-terminus binds to a similar extent as WT aSyn, with a reduction in binding beyond the phosphorylation site extending through the helix-2 region[290]. Thus, phosphorylation of Y39, as well as the Y39E mutation, locally detaches the protein from the membrane surface, restraining the propagation of helix formation and hindering the region downstream of position 39 from binding to the membrane. This leaves the remainder of the lipid-binding domain free in solution.

pY39 aSyn, like Y39E aSyn, was found to aggregate slower than WT aSyn, as measured by ThT fluorescence[290,291]. Furthermore, both pY39 and Y39E, but not WT aSyn, showed reduced prolongation of pathological aSyn seeds *in vivo* and exhibited a reduced seeding capacity *in vitro*[297]. Notably, Pan *et al.* (2020) observed an unusual bidirectional effect on aggregation depending on the ratio of pY39 to WT aSyn. They reported that using 1 to 5% pY39 aSyn as starting material, aSyn aggregation accelerated, whereas increasing the starting material above 10%, the rate of aggregation decreased. A similar phenomenon was observed for the Y39E mutant, with the turning point for acceleration found to be between 10 to 25%. Pan *et al.* (2020) explained this by the direct stacking of the residue Y39 upon the next monomer in the fibril. Introducing a charge at this position might result in electrostatic repulsion, thereby destabilizing fibril formation. This effect would be stronger for pY39 aSyn, which carries two negative charges, and less pronounced for the Y39E mutant, carrying only one negative charge[291]. This result gains significance in combination with recent findings by Zhang *et al.* (2023), who reported that 10 to 40% of aSyn in control and patient brains exhibits phosphorylation at position 39. Moreover, they demonstrated that 25 to 60% of pY39 aSyn is in a monomeric state free in solution[297]. Given that pY39 aSyn has been found in both, disease and healthy brains, a physiological role of this phosphorylation is likely.

Phosphorylation at Y39 aSyn represents the only PTM for which the resulting fibril structure has been resolved in detail. Zhao *et al.* (2020) identified three distinct pY39 aSyn fibril polymorphs, each displaying different morphologies compared to WT aSyn fibrils. Detailed characterization through cryoEM revealed that 20% of Y39E aSyn fibrils appeared straight, comprising two protofilaments aligned in parallel. The two other polymorphs were twisted fibrils (40%/40%), one with two protofilaments (twist-dimer) and the other with three protofilaments (twist-trimer, Figure 45A).

Interfaces between protofilaments in the twist-dimer and twist-trimer shared similarities, both being composed of salt bridges formed by residues E57 and K58[302].

CryoEM observations demonstrate that pY39 aSyn adopts a hook-like structure, encompassing residues 1 to 100, including the entire N-terminus, the NAC domain, and a short segment of the C-terminus. This configuration constitutes the largest fibril core reported for aSyn to date, potentially enhancing its stability and protection against proteases. Positioned at the center of the hook, pY39, along with E20 and E28, neutralizes the positive charges of K21, K23, K32, K34, K43, and K45 (Figure 45B)[302].

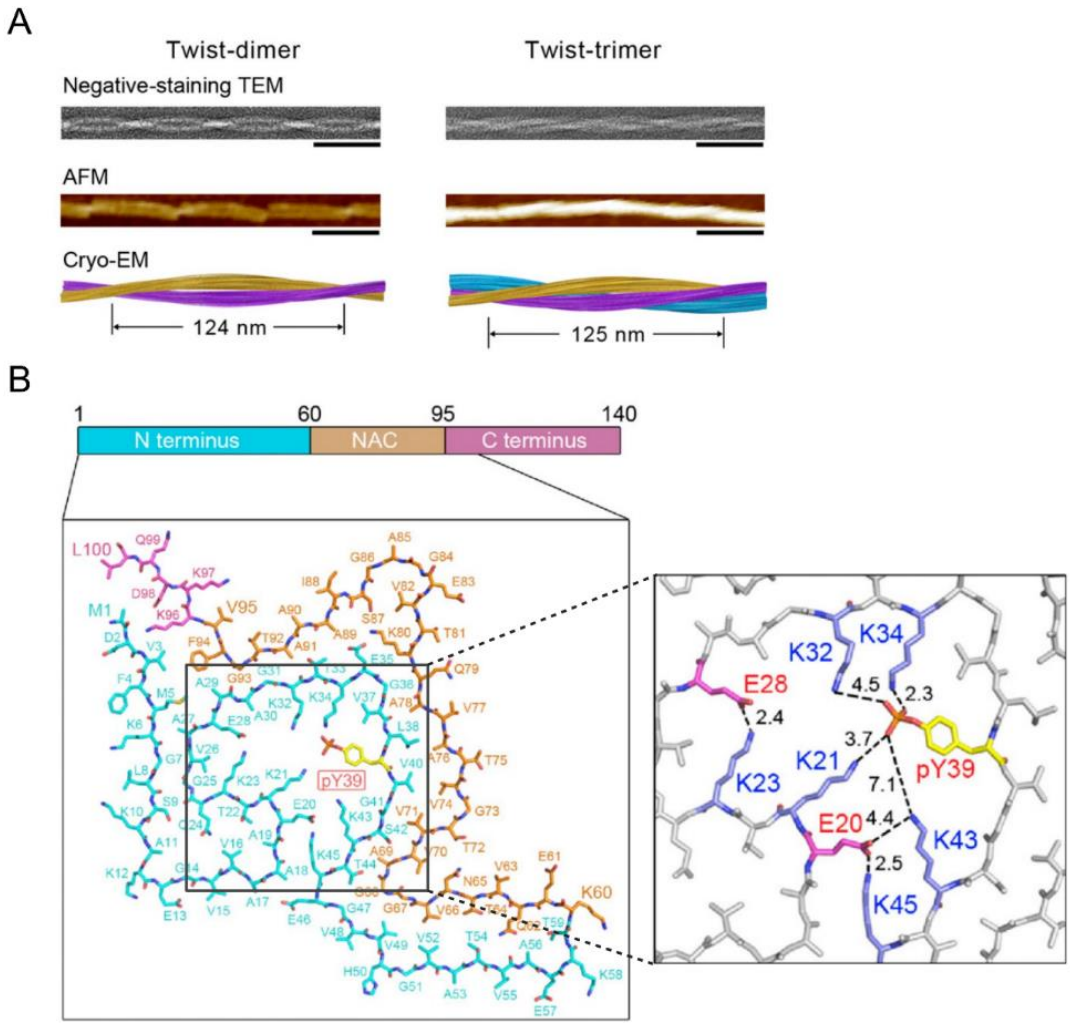

Figure 45: Structure of pY39 aSyn fibrils. (A) Twist-dimer and twist-trimer polymorphs of pY39 aSyn, TEM, atomic force microscopy (AFM) and cryoEM images. (B) Schematic representation of the structure of residues 1-100 of pY39 in fibrils. The center of the hook-like structure is stabilized by electrostatic interactions of positively charge lysine residues (blue) and negatively charged residues (red). Adopted from Zhao *et al.* (2020)[302].

Compelling evidence underscores the pathological significance of pY39 in aSyn. Inhibition of c-abl, a key kinase in the phosphorylation of aSyn at position 39, results in heightened degradation of aSyn and a consequential prevention of dopaminergic neurodegeneration[290,303]. Moreover, pY39 aSyn exhibits elevated toxicity to neurons compared to WT aSyn, observed by neuronal exposure to preformed fibril seeds (PFFs)[302]. Notably, the therapeutic compound 5, a promising c-abl inhibitor for PD treatment in humans, demonstrates significant efficacy. It effectively prevents PFF-induced neurotoxicity and LB pathology *in vivo*. Additionally, compound 5 provides protective effects against aSyn PFF-induced dopaminergic neurodegeneration, terminal loss, motor behavior deficits, and even shows potential in reducing neuroinflammation in mice[303]. Consequently, both pY39 aSyn and its phosphomimetic counterpart, Y39E aSyn, replicate a pathological phenotype, enhancing toxicity and ultimately leading to dopaminergic neurodegeneration and cell loss.

5 Conclusion

In conjunction with existing literature, the findings of this study reveal that the Y39E aSyn mutant exhibits the same structural properties and comparable backbone dynamics as the WT aSyn monomer, while the membrane binding of the NAC region is altered. Y39E aSyn shows reduced monomer consumption and slower, concentration dependent aggregation kinetics compared to WT aSyn, and results in fewer inclusions *in vivo*, while causing an increase in dopaminergic neurodegeneration. Notably, the toxicity induced by this mutant is not mediated through mitochondrial dysfunction (Figure 46). Instead, the elevated toxicity might originate from alterations in autophagic or necroptotic pathways. It could be shown that inhibiting either of these pathways leads to decreased dopaminergic neurodegeneration and improved motor performance[304]. Further cell death pathways, such as ferroptosis, an iron dependent cell death pathway involving a lethal accumulation of lipid peroxides, has emerged as another contributor to cell death in PD. Inhibitors of this pathway are being tested in clinical trials[305,306].

Moreover, given that the Y39E mutant displays slower aggregation kinetics and fewer cellular inclusions but heightened dopaminergic neurodegeneration, the outcomes of this investigation support the theory that toxicity is not related to the rate of fibrillization[216].

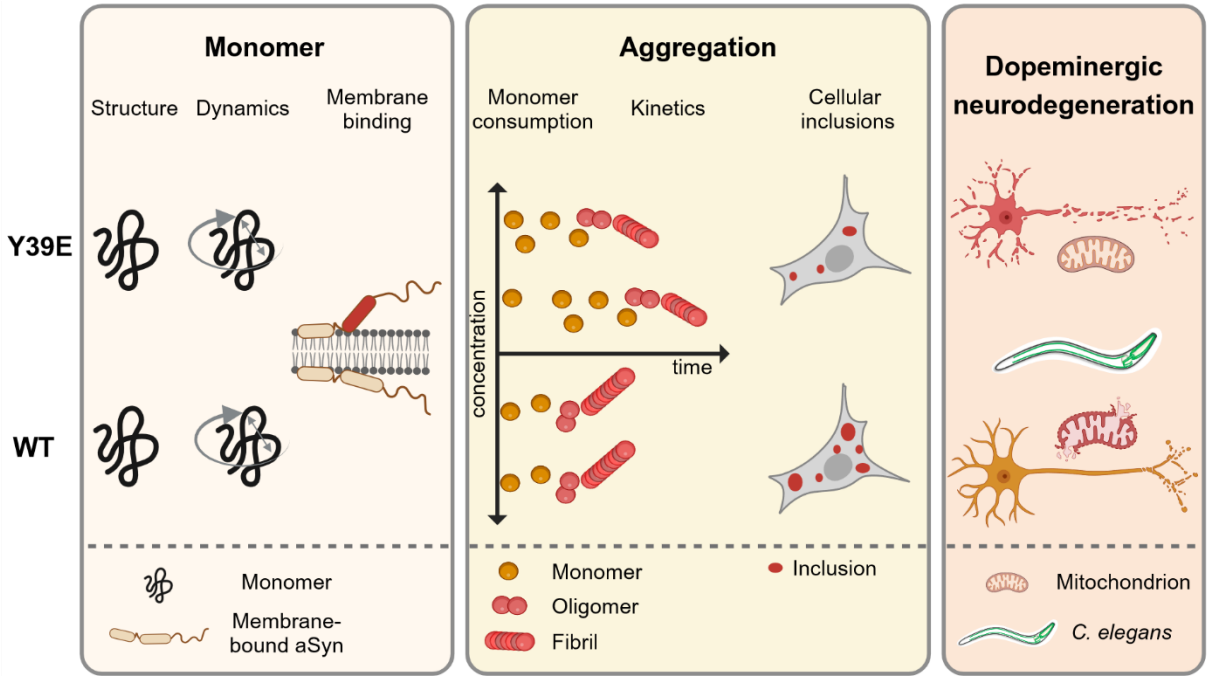

Figure 46: Schematic representation of differences between Y39E and WT aSyn. On a monomeric level, there were no differences in structural features and only slight differences in backbone dynamics observed. Membrane binding was reduced in the NAC region. The aggregation of Y39E aSyn is slower and concentration-dependent, while it leads to less cellular inclusions. Dopaminergic neurodegeneration was observed elevated in *C. elegans*, while mitochondria could be ruled out as toxicity-generating pathway.

The Y39E mutant serves as a suitable model for exploring various facets of phosphorylation at this site, although findings should be validated through the expression of pY39 aSyn.

The rationale behind phosphorylating aSyn at position 39 remains elusive, yet a speculative, physiological relevance for pY39 aSyn emerges. C-abl phosphorylation of aSyn at position 39 might play a protective role, preventing aggregation at the mitochondrial membrane by modulating its interaction with membranes. This, in turn, could support aSyn in fulfilling its physiological role of binding to SVs by enhancing the simultaneous binding to various membranes[245,290]. This notion finds support in the more exposed conformation that the NAC region of Y39E aSyn adopts upon membrane interaction and in the greater number of lipids interacting with Y39E aSyn. Furthermore, various chaperones interact with aSyn and trigger a re-location to the mitochondrial membrane, resulting in transient membrane binding and leading to the formation of aggregates. This interaction is directly impaired by the phosphorylation of aSyn at Y39[245]. The protective role of phosphorylation may transition to a toxic effect at higher phosphorylation levels, with toxicity likely mediated through

autophagic or lysosomal pathways[247,291,298]. To validate this hypothesis, further investigations into Y39E and pY39 aSyn are imperative, focusing on elucidating the origin of toxicity and unraveling the physiological role of aSyn.

6 References

1 Carrell RW, Lomas DA. Conformational disease. *Lancet (London, England)*. 1997;350(9071):134-138. doi:10.1016/S0140-6736(97)02073-4.

2 Kovacs GG. Molecular Pathological Classification of Neurodegenerative Diseases: Turning towards Precision Medicine. *Int J Mol Sci*. 2016;17(2). doi:10.3390/ijms17020189.

3 Dugger BN, Adler CH, Shill HA, et al. Concomitant pathologies among a spectrum of parkinsonian disorders. *Parkinsonism Relat Disord*. 2014;20(5):525-529. doi:10.1016/j.parkreldis.2014.02.012.

4 Uchikado H, DelleDonne A, Ahmed Z, Dickson DW. Lewy bodies in progressive supranuclear palsy represent an independent disease process. *Journal of neuropathology and experimental neurology*. 2006;65(4):387-395. doi:10.1097/01.jnen.0000218449.17073.43.

5 Arias, José Juan Antonio Ibarra. *Frontiers in Clinical Drug Research – Dementia: Volume 2:* Bentham Science Publishers; 2021.

6 Gibb WR, Lees AJ. The relevance of the Lewy body to the pathogenesis of idiopathic Parkinson's disease. *J Neurol Neurosurg Psychiatry*. 1988;51(6):745-752. doi:10.1136/jnnp.51.6.745.

7 Schmitt FA, Davis DG, Wekstein DR, Smith CD, Ashford JW, Markesbery WR. "Preclinical" AD revisited: neuropathology of cognitively normal older adults. *Neurology*. 2000;55(3):370-376. doi:10.1212/wnl.55.3.370.

8 Sparks DL, Danner FW, Davis DG, Hackney C, Landers T, Coyne CM. Neurochemical and histopathologic alterations characteristic of Pick's disease in a non-demented individual. *Journal of neuropathology and experimental neurology*. 1994;53(1):37-42. doi:10.1097/00005072-199401000-00005.

9 Uversky VN, Gillespie JR, Fink AL. Why are ?natively unfolded? proteins unstructured under physiologic conditions? *Proteins*. 2000;41(3):415-427. doi:10.1002/1097-0134(20001115)41:3<415:AID-PROT130>3.0.CO;2-7.

10 Bondos SE, Dunker AK, Uversky VN. On the roles of intrinsically disordered proteins and regions in cell communication and signaling. *Cell Commun Signal*. 2021;19(1):88. doi:10.1186/s12964-021-00774-3.

11 Yoon M-K, Mitrea DM, Ou L, Kriwacki RW. Cell cycle regulation by the intrinsically disordered proteins p21 and p27. *Biochem Soc Trans*. 2012;40(5):981-988. doi:10.1042/BST20120092.

12 Shammas SL. Mechanistic roles of protein disorder within transcription. *Curr Opin Struct Biol*. 2017;42:155-161. doi:10.1016/j.sbi.2017.02.003.

13 Forman-Kay JD, Mittag T. From sequence and forces to structure, function, and evolution of intrinsically disordered proteins. *Structure*. 2013;21(9):1492-1499. doi:10.1016/j.str.2013.08.001.

14 Dyson HJ, Wright PE. Intrinsically unstructured proteins and their functions. *Nat Rev Mol Cell Biol*. 2005;6(3):197-208. doi:10.1038/nrm1589.

15 Oldfield CJ, Dunker AK. Intrinsically disordered proteins and intrinsically disordered protein regions. *Annu Rev Biochem*. 2014;83:553-584. doi:10.1146/annurev-biochem-072711-164947.

16 Radivojac P, Iakoucheva LM, Oldfield CJ, Obradovic Z, Uversky VN, Dunker AK. Intrinsic disorder and functional proteomics. *Biophys J*. 2007;92(5):1439-1456. doi:10.1529/biophysj.106.094045.

17 Breydo L, Redington JM, Uversky VN. Effects of Intrinsic and Extrinsic Factors on Aggregation of Physiologically Important Intrinsically Disordered Proteins. *Int Rev Cell Mol Biol*. 2017;329:145-185. doi:10.1016/bs.ircmb.2016.08.011.

18 Haynes CM, Titus EA, Cooper AA. Degradation of misfolded proteins prevents ER-derived oxidative stress and cell death. *Mol Cell*. 2004;15(5):767-776. doi:10.1016/j.molcel.2004.08.025.

19 Hromadkova L, Siddiqi MK, Liu H, Safar JG. Populations of Tau Conformers Drive Prion-like Strain Effects in Alzheimer's Disease and Related Dementias. *Cells*. 2022;11(19). doi:10.3390/cells11192997.

20 Tsoi PS, Quan MD, Ferreon JC, Ferreon ACM. Aggregation of Disordered Proteins Associated with Neurodegeneration. *Int J Mol Sci*. 2023;24(4). doi:10.3390/ijms24043380.

21 Ross CA, Poirier MA. Protein aggregation and neurodegenerative disease. *Nat Med*. 2004;10 Suppl:S10-7. doi:10.1038/nm1066.

22 Cras P, van Harskamp F, Hendriks L, et al. Presenile Alzheimer dementia characterized by amyloid angiopathy and large amyloid core type senile plaques in the APP 692Ala--Gly mutation. *Acta Neuropathol*. 1998;96(3):253-260. doi:10.1007/s004010050892.

23 Goedert M, Spillantini MG, Jakes R, Rutherford D, Crowther RA. Multiple isoforms of human microtubule-associated protein tau: sequences and localization in neurofibrillary tangles of Alzheimer's disease. *Neuron*. 1989;3(4):519-526. doi:10.1016/0896-6273(89)90210-9.

24 Ballatore C, Lee VM-Y, Trojanowski JQ. Tau-mediated neurodegeneration in Alzheimer's disease and related disorders. *Nat Rev Neurosci*. 2007;8(9):663-672. doi:10.1038/nrn2194.

25 Arai T, Hasegawa M, Akiyama H, et al. TDP-43 is a component of ubiquitin-positive tau-negative inclusions in frontotemporal lobar degeneration and amyotrophic lateral sclerosis. *Biochem Biophys Res Commun*. 2006;351(3):602-611. doi:10.1016/j.bbrc.2006.10.093.

26 Valera E, Spencer B, Masliah E. Immunotherapeutic Approaches Targeting Amyloid-β, α-Synuclein, and Tau for the Treatment of Neurodegenerative Disorders. *Neurotherapeutics*. 2016;13(1):179-189. doi:10.1007/s13311-015-0397-z.

27 McKeith IG, Galasko D, Kosaka K, et al. Consensus guidelines for the clinical and pathologic diagnosis of dementia with Lewy bodies (DLB): report of the consortium on DLB international workshop. *Neurology*. 1996;47(5):1113-1124. doi:10.1212/wnl.47.5.1113.

28 Menšíková K, Matěj R, Colosimo C, et al. Lewy body disease or diseases with Lewy bodies? *npj Parkinsons Dis.* 2022;8(1):3. doi:10.1038/s41531-021-00273-9.

29 Driver JA, Logroscino G, Gaziano JM, Kurth T. Incidence and remaining lifetime risk of Parkinson disease in advanced age. *Neurology*. 2009;72(5):432-438. doi:10.1212/01.wnl.0000341769.50075.bb.

30 Ou Z, Pan J, Tang S, et al. Global Trends in the Incidence, Prevalence, and Years Lived With Disability of Parkinson's Disease in 204 Countries/Territories From 1990 to 2019. *Front Public Health*. 2021;9:776847. doi:10.3389/fpubh.2021.776847.

31 Tysnes O-B, Storstein A. Epidemiology of Parkinson's disease. *J Neural Transm (Vienna)*. 2017;124(8):901-905. doi:10.1007/s00702-017-1686-y.

32 Dorsey ER, Sherer T, Okun MS, Bloem BR. The Emerging Evidence of the Parkinson Pandemic. *J Parkinsons Dis*. 2018;8(s1):S3-S8. doi:10.3233/JPD-181474.

33 Tolosa E, Garrido A, Scholz SW, Poewe W. Challenges in the diagnosis of Parkinson's disease. *Lancet Neurol*. 2021;20(5):385-397. doi:10.1016/S1474-4422(21)00030-2.

34 Parkinson's Foundation. Statistics. https://www.parkinson.org/understanding-parkinsons/statistics. Updated November 1, 2023. Accessed November 1, 2023.

35 Braak H, Del Tredici K, Rüb U, Vos RAI de, Jansen Steur ENH, Braak E. Staging of brain pathology related to sporadic Parkinson's disease. *Neurobiology of aging*. 2003;24(2):197-211. doi:10.1016/s0197-4580(02)00065-9.

36 Forno LS. Neuropathology of Parkinson's disease. *Journal of neuropathology and experimental neurology*. 1996;55(3):259-272. doi:10.1097/00005072-199603000-00001.

37 Gibb WR. Idiopathic Parkinson's disease and the Lewy body disorders. *Neuropathology and Applied Neurobiology*. 1986;12(3):223-234. doi:10.1111/j.1365-2990.1986.tb00136.x.

38 Spillantini MG, Crowther RA, Jakes R, Hasegawa M, Goedert M. alpha-Synuclein in filamentous inclusions of Lewy bodies from Parkinson's disease and dementia with lewy bodies. *Proc Natl Acad Sci U S A*. 1998;95(11):6469-6473. doi:10.1073/pnas.95.11.6469.

39 Spillantini MG, Schmidt ML, Lee VM, Trojanowski JQ, Jakes R, Goedert M. Alpha-synuclein in Lewy bodies. *Nature*. 1997;388(6645):839-840. doi:10.1038/42166.

40 Shahmoradian SH, Lewis AJ, Genoud C, et al. Lewy pathology in Parkinson's disease consists of crowded organelles and lipid membranes. *Nat Neurosci*. 2019;22(7):1099-1109. doi:10.1038/s41593-019-0423-2.

41 Gottapu RD, Dagli CH. Analysis of Parkinson's Disease Data. *Procedia Computer Science*. 2018;140:334-341. doi:10.1016/j.procs.2018.10.306.

42 Balestrino R, Schapira AHV. Parkinson disease. *Eur J Neurol*. 2020;27(1):27-42. doi:10.1111/ene.14108.

43 Dauer W, Przedborski S. Parkinson's disease: mechanisms and models. *Neuron*. 2003;39(6):889-909. doi:10.1016/s0896-6273(03)00568-3.

44 Signature Health Services. Parkinson's Disease. https://www.signaturehealthservices.net/specialty/parkinsons-disease/#. Updated November 7, 2022. Accessed November 6, 2023.

45 van den Eeden SK, Tanner CM, Bernstein AL, et al. Incidence of Parkinson's disease: variation by age, gender, and race/ethnicity. *Am J Epidemiol*. 2003;157(11):1015-1022. doi:10.1093/aje/kwg068.

46 Skjærbæk C, Knudsen K, Horsager J, Borghammer P. Gastrointestinal Dysfunction in Parkinson's Disease. *J Clin Med*. 2021;10(3). doi:10.3390/jcm10030493.

47 Chaudhuri KR, Odin P. The challenge of non-motor symptoms in Parkinson's disease. *Prog Brain Res*. 2010;184:325-341. doi:10.1016/S0079-6123(10)84017-8.

48 Schaeffer E, Postuma RB, Berg D. Prodromal PD: A new nosological entity. *Prog Brain Res*. 2020;252:331-356. doi:10.1016/bs.pbr.2020.01.003.

49 Meles SK, Oertel WH, Leenders KL. Circuit imaging biomarkers in preclinical and prodromal Parkinson's disease. *Mol Med*. 2021;27(1):111. doi:10.1186/s10020-021-00327-x.

50 Davie CA. A review of Parkinson's disease. *Br Med Bull*. 2008;86:109-127. doi:10.1093/bmb/ldn013.

51 Lyons KE, Pahwa R. The impact and management of nonmotor symptoms of Parkinson's disease. *Am J Manag Care*. 2011;17 Suppl 12:S308-14.

52 Jankovic J, Tan EK. Parkinson's disease: etiopathogenesis and treatment. *J Neurol Neurosurg Psychiatry*. 2020;91(8):795-808. doi:10.1136/jnnp-2019-322338.

53 Chan PY, Ripin ZM, Halim SA, et al. Motion characteristics of subclinical tremors in Parkinson's disease and normal subjects. *Sci Rep*. 2022;12(1):4021. doi:10.1038/s41598-022-07957-z.

54 Hobson P, Meara J. Mild cognitive impairment in Parkinson's disease and its progression onto dementia: a 16-year outcome evaluation of the Denbighshire cohort. *Int J Geriatr Psychiatry*. 2015;30(10):1048-1055. doi:10.1002/gps.4261.

55 Cookson MR. alpha-Synuclein and neuronal cell death. *Mol Neurodegener*. 2009;4:9. doi:10.1186/1750-1326-4-9.

56 Chen Y, Sun X, Lin Y, Zhang Z, Gao Y, Wu IXY. Non-Genetic Risk Factors for Parkinson's Disease: An Overview of 46 Systematic Reviews. *J Parkinsons Dis*. 2021;11(3):919-935. doi:10.3233/JPD-202521.

57 Dutheil F, Beaune P, Tzourio C, Loriot M-A, Elbaz A. Interaction between ABCB1 and professional exposure to organochlorine insecticides in Parkinson disease. *Arch Neurol*. 2010;67(6):739-745. doi:10.1001/archneurol.2010.101.

58 Hu C-Y, Fang Y, Li F-L, et al. Association between ambient air pollution and Parkinson's disease: Systematic review and meta-analysis. *Environ Res*. 2019;168:448-459. doi:10.1016/j.envres.2018.10.008.

59 Cerri S, Mus L, Blandini F. Parkinson's Disease in Women and Men: What's the Difference? *J Parkinsons Dis*. 2019;9(3):501-515. doi:10.3233/JPD-191683.

60 Costa J, Lunet N, Santos C, Santos J, Vaz-Carneiro A. Caffeine exposure and the risk of Parkinson's disease: a systematic review and meta-analysis of observational studies. *J Alzheimers Dis*. 2010;20 Suppl 1:S221-38. doi:10.3233/JAD-2010-091525.

61 Ritz B, Ascherio A, Checkoway H, et al. Pooled analysis of tobacco use and risk of Parkinson disease. *Arch Neurol*. 2007;64(7):990-997. doi:10.1001/archneur.64.7.990.

62 Scheperjans F, Pekkonen E, Kaakkola S, Auvinen P. Linking Smoking, Coffee, Urate, and Parkinson's Disease - A Role for Gut Microbiota? *J Parkinsons Dis*. 2015;5(2):255-262. doi:10.3233/JPD-150557.

63 Tran J, Anastacio H, Bardy C. Genetic predispositions of Parkinson's disease revealed in patient-derived brain cells. *NPJ Parkinsons Dis*. 2020;6:8. doi:10.1038/s41531-020-0110-8.

64 Paisán-Ruíz C, Jain S, Evans EW, et al. Cloning of the gene containing mutations that cause PARK8-linked Parkinson's disease. *Neuron*. 2004;44(4):595-600. doi:10.1016/j.neuron.2004.10.023.

65 Polymeropoulos MH, Lavedan C, Leroy E, et al. Mutation in the alpha-synuclein gene identified in families with Parkinson's disease. *Science*. 1997;276(5321):2045-2047. doi:10.1126/science.276.5321.2045.

66 Zimprich A, Biskup S, Leitner P, et al. Mutations in LRRK2 cause autosomal-dominant parkinsonism with pleomorphic pathology. *Neuron*. 2004;44(4):601-607. doi:10.1016/j.neuron.2004.11.005.

67 Bonifati V, Rizzu P, van Baren MJ, et al. Mutations in the DJ-1 gene associated with autosomal recessive early-onset parkinsonism. *Science*. 2003;299(5604):256-259. doi:10.1126/science.1077209.

68 Kitada T, Asakawa S, Hattori N, et al. Mutations in the parkin gene cause autosomal recessive juvenile parkinsonism. *Nature*. 1998;392(6676):605-608. doi:10.1038/33416.

69 Ramirez A, Heimbach A, Gründemann J, et al. Hereditary parkinsonism with dementia is caused by mutations in ATP13A2, encoding a lysosomal type 5 P-type ATPase. *Nature genetics*. 2006;38(10):1184-1191. doi:10.1038/ng1884.

70 Valente EM, Abou-Sleiman PM, Caputo V, et al. Hereditary early-onset Parkinson's disease caused by mutations in PINK1. *Science*. 2004;304(5674):1158-1160. doi:10.1126/science.1096284.

71 Abbott A. Levodopa: the story so far. *Nature*. 2010;466(7310):S6-7. doi:10.1038/466S6a.

72 Armstrong MJ, Okun MS. Diagnosis and Treatment of Parkinson Disease: A Review. *JAMA*. 2020;323(6):548-560. doi:10.1001/jama.2019.22360.

73 Connolly BS, Lang AE. Pharmacological treatment of Parkinson disease: a review. *JAMA*. 2014;311(16):1670-1683. doi:10.1001/jama.2014.3654.

74 Elsworth JD, Roth RH. Dopamine synthesis, uptake, metabolism, and receptors: relevance to gene therapy of Parkinson's disease. *Exp Neurol*. 1997;144(1):4-9. doi:10.1006/exnr.1996.6379.

75 Cookson MR. The biochemistry of Parkinson's disease. *Annu Rev Biochem*. 2005;74:29-52. doi:10.1146/annurev.biochem.74.082803.133400.

76 Gray R, Ives N, Rick C, et al. Long-term effectiveness of dopamine agonists and monoamine oxidase B inhibitors compared with levodopa as initial treatment for Parkinson's disease (PD MED): a large, open-label, pragmatic randomised trial. *Lancet (London, England)*. 2014;384(9949):1196-1205. doi:10.1016/S0140-6736(14)60683-8.

77 Stowe RL, Ives NJ, Clarke C, et al. Dopamine agonist therapy in early Parkinson's disease. *Cochrane Database Syst Rev*. 2008;(2):CD006564. doi:10.1002/14651858.CD006564.pub2.

78 Foley P, Gerlach M, Youdim MB, Riederer P. MAO-B inhibitors: multiple roles in the therapy of neurodegenerative disorders? *Parkinsonism Relat Disord*. 2000;6(1):25-47. doi:10.1016/s1353-8020(99)00043-7.

79 Crews L, Spencer B, Desplats P, et al. Selective molecular alterations in the autophagy pathway in patients with Lewy body disease and in models of alpha-synucleinopathy. *PLoS One*. 2010;5(2):e9313. doi:10.1371/journal.pone.0009313.

80 Hirohata M, Ono K, Morinaga A, Yamada M. Non-steroidal anti-inflammatory drugs have potent anti-fibrillogenic and fibril-destabilizing effects for alpha-synuclein fibrils in vitro. *Neuropharmacology*. 2008;54(3):620-627. doi:10.1016/j.neuropharm.2007.11.010.

81 Pontone GM, Mills KA. Optimal Treatment of Depression and Anxiety in Parkinson's Disease. *Am J Geriatr Psychiatry*. 2021;29(6):530-540. doi:10.1016/j.jagp.2021.02.037.

82 Ding H, Dhima K, Lockhart KC, et al. Unrecognized vitamin D3 deficiency is common in Parkinson disease: Harvard Biomarker Study. *Neurology*. 2013;81(17):1531-1537. doi:10.1212/WNL.0b013e3182a95818.

83 Peterson AL, Murchison C, Zabetian C, et al. Memory, mood, and vitamin D in persons with Parkinson's disease. *J Parkinsons Dis*. 2013;3(4):547-555. doi:10.3233/JPD-130206.

84 Artusi CA, Lopiano L, Morgante F. Deep Brain Stimulation Selection Criteria for Parkinson's Disease: Time to Go beyond CAPSIT-PD. *J Clin Med*. 2020;9(12). doi:10.3390/jcm9123931.

85 Cernera S, Eisinger RS, Wong JK, et al. Long-term Parkinson's disease quality of life after staged DBS: STN vs GPi and first vs second lead. *NPJ Parkinsons Dis*. 2020;6:13. doi:10.1038/s41531-020-0115-3.

86 Clancy Medical Group. Parkinson's Disease: Symptoms and Early Warning Signs of PD. https://www.clancymedicalgroup.com/parkinsons-disease/. Updated April 14, 2023. Accessed November 8, 2023.

87 Crowley EK, Nolan YM, Sullivan AM. Exercise as a therapeutic intervention for motor and non-motor symptoms in Parkinson's disease: Evidence from rodent models. *Prog Neurobiol*. 2019;172:2-22. doi:10.1016/j.pneurobio.2018.11.003.

88 Amara AW, Memon AA. Effects of Exercise on Non-motor Symptoms in Parkinson's Disease. *Clin Ther*. 2018;40(1):8-15. doi:10.1016/j.clinthera.2017.11.004.

89 Bryans LA, Palmer AD, Anderson S, Schindler J, Graville DJ. The impact of Lee Silverman Voice Treatment (LSVT LOUD®) on voice, communication, and participation: Findings from a prospective, longitudinal study. *J Commun Disord*. 2021;89:106031. doi:10.1016/j.jcomdis.2020.106031.

90 Ebersbach G, Ebersbach A, Edler D, et al. Comparing exercise in Parkinson's disease--the Berlin LSVT®BIG study. *Mov Disord*. 2010;25(12):1902-1908. doi:10.1002/mds.23212.

91 Bega D, Gonzalez-Latapi P, Zadikoff C, Simuni T. A review of the clinical evidence for complementary and alternative therapies in Parkinson's disease. *Curr Treat Options Neurol*. 2014;16(10):314. doi:10.1007/s11940-014-0314-5.

92 van der Heide A, Meinders MJ, Speckens AEM, Peerbolte TF, Bloem BR, Helmich RC. Stress and Mindfulness in Parkinson's Disease: Clinical Effects and Potential Underlying Mechanisms. *Mov Disord*. 2021;36(1):64-70. doi:10.1002/mds.28345.

93 Li S, Le W. Parkinson's disease in traditional Chinese medicine. *Lancet Neurol*. 2021;20(4):262. doi:10.1016/S1474-4422(19)30224-8.

94 Lee S-H, Lim S. Clinical effectiveness of acupuncture on Parkinson disease: A PRISMA-compliant systematic review and meta-analysis. *Medicine (Baltimore)*. 2017;96(3):e5836. doi:10.1097/MD.0000000000005836.

95 An alternative medicine treatment for Parkinson's disease: results of a multicenter clinical trial. HP-200 in Parkinson's Disease Study Group. *J Altern Complement Med*. 1995;1(3):249-255. doi:10.1089/acm.1995.1.249.

96 Pujols J, Peña-Díaz S, Lázaro DF, et al. Small molecule inhibits α-synuclein aggregation, disrupts amyloid fibrils, and prevents degeneration of dopaminergic neurons. *Proc Natl Acad Sci U S A*. 2018;115(41):10481-10486. doi:10.1073/pnas.1804198115.

97 Wagner J, Ryazanov S, Leonov A, et al. Anle138b: a novel oligomer modulator for disease-modifying therapy of neurodegenerative diseases such as prion and Parkinson's disease. *Acta Neuropathol*. 2013;125(6):795-813. doi:10.1007/s00401-013-1114-9.

98 Levin J, Schmidt F, Boehm C, et al. The oligomer modulator anle138b inhibits disease progression in a Parkinson mouse model even with treatment started after disease onset. *Acta Neuropathol*. 2014;127(5):779-780. doi:10.1007/s00401-014-1265-3.

99 George JM. The synucleins. *Genome Biol*. 2002;3(1):REVIEWS3002. doi:10.1186/gb-2001-3-1-reviews3002.

100 Shibasaki Y, Baillie DA, St Clair D, Brookes AJ. High-resolution mapping of SNCA encoding alpha-synuclein, the non-A beta component of Alzheimer's disease amyloid precursor, to human chromosome 4q21.3--q22 by fluorescence in situ hybridization. *Cytogenetics and cell genetics*. 1995;71(1):54-55. doi:10.1159/000134061.

101 Chen X, Silva HA de, Pettenati MJ, et al. The human NACP/alpha-synuclein gene: chromosome assignment to 4q21.3-q22 and TaqI RFLP analysis. *Genomics*. 1995;26(2):425-427. doi:10.1016/0888-7543(95)80237-g.

102 Lavedan C. The synuclein family. *Genome Res*. 1998;8(9):871-880. doi:10.1101/gr.8.9.871.

103 Iwai A, Masliah E, Yoshimoto M, et al. The precursor protein of non-A beta component of Alzheimer's disease amyloid is a presynaptic protein of the central nervous system. *Neuron*. 1995;14(2):467-475. doi:10.1016/0896-6273(95)90302-x.

104 Uéda K, Fukushima H, Masliah E, et al. Molecular cloning of cDNA encoding an unrecognized component of amyloid in Alzheimer disease. *Proc Natl Acad Sci U S A*. 1993;90(23):11282-11286. doi:10.1073/pnas.90.23.11282.

105 Nakajo S, Tsukada K, Omata K, Nakamura Y, Nakaya K. A new brain-specific 14-kDa protein is a phosphoprotein. Its complete amino acid sequence and evidence for phosphorylation. *European journal of biochemistry*. 1993;217(3):1057-1063. doi:10.1111/j.1432-1033.1993.tb18337.x.

106 Maroteaux L, Campanelli JT, Scheller RH. Synuclein: a neuron-specific protein localized to the nucleus and presynaptic nerve terminal. *J Neurosci*. 1988;8(8):2804-2815. doi:10.1523/JNEUROSCI.08-08-02804.1988.

107 El-Agnaf OMA, Salem SA, Paleologou KE, et al. Detection of oligomeric forms of alpha-synuclein protein in human plasma as a potential biomarker for Parkinson's disease. *FASEB J*. 2006;20(3):419-425. doi:10.1096/fj.03-1449com.

108 Tokuda T, Qureshi MM, Ardah MT, et al. Detection of elevated levels of α-synuclein oligomers in CSF from patients with Parkinson disease. *Neurology*. 2010;75(20):1766-1772. doi:10.1212/WNL.0b013e3181fd613b.

109 Saborio GP, Permanne B, Soto C. Sensitive detection of pathological prion protein by cyclic amplification of protein misfolding. *Nature*. 2001;411(6839):810-813. doi:10.1038/35081095.

110 Kragh CL, Ubhi K, Wyss-Coray T, Masliah E. Autophagy in dementias. *Brain Pathol*. 2012;22(1):99-109. doi:10.1111/j.1750-3639.2011.00545.x.

111 McNaught KSP, Mytilineou C, Jnobaptiste R, et al. Impairment of the ubiquitin-proteasome system causes dopaminergic cell death and inclusion body formation in ventral mesencephalic cultures. *Journal of neurochemistry*. 2002;81(2):301-306. doi:10.1046/j.1471-4159.2002.00821.x.

112 Cuervo AM, Stefanis L, Fredenburg R, Lansbury PT, Sulzer D. Impaired degradation of mutant alpha-synuclein by chaperone-mediated autophagy. *Science*. 2004;305(5688):1292-1295. doi:10.1126/science.1101738.

113 Webb JL, Ravikumar B, Atkins J, Skepper JN, Rubinsztein DC. Alpha-Synuclein is degraded by both autophagy and the proteasome. *The Journal of Biological Chemistry*. 2003;278(27):25009-25013. doi:10.1074/jbc.M300227200.

114 Masaracchia C, Hnida M, Gerhardt E, et al. Membrane binding, internalization, and sorting of alpha-synuclein in the cell. *Acta Neuropathol Commun*. 2018;6(1):79. doi:10.1186/s40478-018-0578-1.

115 Klucken J, Shin Y, Masliah E, Hyman BT, McLean PJ. Hsp70 Reduces alpha-Synuclein Aggregation and Toxicity. *The Journal of Biological Chemistry*. 2004;279(24):25497-25502. doi:10.1074/jbc.M400255200.

116 Iwata A, Maruyama M, Akagi T, et al. Alpha-synuclein degradation by serine protease neurosin: implication for pathogenesis of synucleinopathies. *Hum Mol Genet*. 2003;12(20):2625-2635. doi:10.1093/hmg/ddg283.

117 Jang A, Lee H-J, Suk J-E, Jung J-W, Kim K-P, Lee S-J. Non-classical exocytosis of alpha-synuclein is sensitive to folding states and promoted under stress conditions. *Journal of neurochemistry*. 2010;113(5):1263-1274. doi:10.1111/j.1471-4159.2010.06695.x.

118 Alvarez-Erviti L, Seow Y, Schapira AH, et al. Lysosomal dysfunction increases exosome-mediated alpha-synuclein release and transmission. *Neurobiol Dis*. 2011;42(3):360-367. doi:10.1016/j.nbd.2011.01.029.

119 Danzer KM, Ruf WP, Putcha P, et al. Heat-shock protein 70 modulates toxic extracellular α-synuclein oligomers and rescues trans-synaptic toxicity. *FASEB J*. 2011;25(1):326-336. doi:10.1096/fj.10-164624.

120 Lee H-J, Suk J-E, Bae E-J, Lee J-H, Paik SR, Lee S-J. Assembly-dependent endocytosis and clearance of extracellular alpha-synuclein. *Int J Biochem Cell Biol*. 2008;40(9):1835-1849. doi:10.1016/j.biocel.2008.01.017.

121 Tsigelny IF, Sharikov Y, Wrasidlo W, et al. Role of α-synuclein penetration into the membrane in the mechanisms of oligomer pore formation. *FEBS J*. 2012;279(6):1000-1013. doi:10.1111/j.1742-4658.2012.08489.x.

122 Brás IC, Outeiro TF. Alpha-Synuclein: Mechanisms of Release and Pathology Progression in Synucleinopathies. *Cells*. 2021;10(2). doi:10.3390/cells10020375.

123 Choi YR, Park SJ, Park SM. Molecular events underlying the cell-to-cell transmission of α-synuclein. *FEBS J*. 2021;288(23):6593-6602. doi:10.1111/febs.15674.

124 Neupane S, Cecco E de, Aguzzi A. The Hidden Cell-to-Cell Trail of α-Synuclein Aggregates. *Journal of Molecular Biology*. 2023;435(12):167930. doi:10.1016/j.jmb.2022.167930.

125 Rustom A, Saffrich R, Markovic I, Walther P, Gerdes H-H. Nanotubular highways for intercellular organelle transport. *Science*. 2004;303(5660):1007-1010. doi:10.1126/science.1093133.

126 Danzer KM, Krebs SK, Wolff M, Birk G, Hengerer B. Seeding induced by alpha-synuclein oligomers provides evidence for spreading of alpha-synuclein pathology. *Journal of neurochemistry*. 2009;111(1):192-203. doi:10.1111/j.1471-4159.2009.06324.x.

127 Desplats P, Lee H-J, Bae E-J, et al. Inclusion formation and neuronal cell death through neuron-to-neuron transmission of alpha-synuclein. *Proc Natl Acad Sci U S A*. 2009;106(31):13010-13015. doi:10.1073/pnas.0903691106.

128 Volpicelli-Daley LA, Luk KC, Lee VM-Y. Addition of exogenous α-synuclein preformed fibrils to primary neuronal cultures to seed recruitment of endogenous α-synuclein to Lewy body and Lewy neurite-like aggregates. *Nature protocols*. 2014;9(9):2135-2146. doi:10.1038/nprot.2014.143.

129 Volpicelli-Daley LA, Luk KC, Patel TP, et al. Exogenous α-synuclein fibrils induce Lewy body pathology leading to synaptic dysfunction and neuron death. *Neuron*. 2011;72(1):57-71. doi:10.1016/j.neuron.2011.08.033.

130 Wakabayashi K, Takahashi H, Ohama E, Ikuta F. Parkinson's disease: an immunohistochemical study of Lewy body-containing neurons in the enteric nervous system. *Acta Neuropathol*. 1990;79(6):581-583. doi:10.1007/BF00294234.

131 Wakabayashi K, Takahashi H, Takeda S, Ohama E, Ikuta F. Parkinson's disease: the presence of Lewy bodies in Auerbach's and Meissner's plexuses. *Acta Neuropathol*. 1988;76(3):217-221. doi:10.1007/BF00687767.

132 Challis C, Hori A, Sampson TR, et al. Gut-seeded α-synuclein fibrils promote gut dysfunction and brain pathology specifically in aged mice. *Nat Neurosci*. 2020;23(3):327-336. doi:10.1038/s41593-020-0589-7.

133 Holmqvist S, Chutna O, Bousset L, et al. Direct evidence of Parkinson pathology spread from the gastrointestinal tract to the brain in rats. *Acta Neuropathol*. 2014;128(6):805-820. doi:10.1007/s00401-014-1343-6.

134 Weinreb PH, Zhen W, Poon AW, Conway KA, Lansbury PT. NACP, a protein implicated in Alzheimer's disease and learning, is natively unfolded. *Biochemistry*. 1996;35(43):13709-13715. doi:10.1021/bi961799n.

135 Burré J, Vivona S, Diao J, Sharma M, Brunger AT, Südhof TC. Properties of native brain α-synuclein. *Nature*. 2013;498(7453):E4-6; discussion E6-7. doi:10.1038/nature12125.

136 Fauvet B, Mbefo MK, Fares M-B, et al. α-Synuclein in central nervous system and from erythrocytes, mammalian cells, and Escherichia coli exists predominantly as disordered monomer. *Journal of Biological Chemistry*. 2012;287(19):15345-15364. doi:10.1074/jbc.M111.318949.

137 Fauvet B, Fares M-B, Samuel F, et al. Characterization of semisynthetic and naturally Nα-acetylated α-synuclein in vitro and in intact cells: implications for aggregation and cellular properties of α-synuclein. *Journal of Biological Chemistry*. 2012;287(34):28243-28262. doi:10.1074/jbc.M112.383711.

138 Dettmer U, Newman AJ, Saucken VE von, Bartels T, Selkoe D. KTKEGV repeat motifs are key mediators of normal α-synuclein tetramerization: Their mutation causes excess monomers and neurotoxicity. *Proc Natl Acad Sci U S A*. 2015;112(31):9596-9601. doi:10.1073/pnas.1505953112.

139 Bartels T, Choi JG, Selkoe DJ. α-Synuclein occurs physiologically as a helically folded tetramer that resists aggregation. *Nature*. 2011;477(7362):107-110. doi:10.1038/nature10324.

140 Iwai A, Yoshimoto M, Masliah E, Saitoh T. Non-A beta component of Alzheimer's disease amyloid (NAC) is amyloidogenic. *Biochemistry*. 1995;34(32):10139-10145. doi:10.1021/bi00032a006.

141 Giasson BI, Murray IV, Trojanowski JQ, Lee VM. A hydrophobic stretch of 12 amino acid residues in the middle of alpha-synuclein is essential for filament assembly. *The Journal of Biological Chemistry*. 2001;276(4):2380-2386. doi:10.1074/jbc.M008919200.

142 Bussell R, Eliezer D. A structural and functional role for 11-mer repeats in alpha-synuclein and other exchangeable lipid binding proteins. *Journal of Molecular Biology*. 2003;329(4):763-778. doi:10.1016/S0022-2836(03)00520-5.

143 Jain K, Ghribi O, Delhommelle J. Folding Free-Energy Landscape of α-Synuclein (35-97) Via Replica Exchange Molecular Dynamics. *J Chem Inf Model*. 2021;61(1):432-443. doi:10.1021/acs.jcim.0c01278.

144 Das T, Ramezani M, Snead D, et al. The Role of Membrane Affinity and Binding Modes in Alpha-Synuclein Regulation of Vesicle Release and Trafficking. *Biomolecules*. 2022;12(12). doi:10.3390/biom12121816.

145 Georgieva ER, Ramlall TF, Borbat PP, Freed JH, Eliezer D. Membrane-bound alpha-synuclein forms an extended helix: long-distance pulsed ESR measurements using vesicles, bicelles, and rodlike micelles. *J Am Chem Soc*. 2008;130(39):12856-12857. doi:10.1021/ja804517m.

146 Adam J. Trexler, E. Rhoades. Alpha-synuclein binds large unilamellar vesicles as an extended helix. *Biochemistry*. 2009. https://www.semanticscholar.org/paper/Alpha-synuclein-binds-large-unilamellar-vesicles-as-Trexler-Rhoades/3087269d1d59511d00ccfe3af822663ecab53e25.

147 Chandra S, Chen X, Rizo J, Jahn R, Südhof TC. A broken alpha -helix in folded alpha -Synuclein. *The Journal of Biological Chemistry*. 2003;278(17):15313-15318. doi:10.1074/jbc.M213128200.

148 Cendrowska U, Silva PJ, Ait-Bouziad N, et al. Unraveling the complexity of amyloid polymorphism using gold nanoparticles and cryo-EM. *Proc Natl Acad Sci U S A*. 2020;117(12):6866-6874. doi:10.1073/pnas.1916176117.

149 Cremades N, Chen SW, Dobson CM. Structural Characteristics of α-Synuclein Oligomers. *Int Rev Cell Mol Biol*. 2017;329:79-143. doi:10.1016/bs.ircmb.2016.08.010.

150 Shahnawaz M, Mukherjee A, Pritzkow S, et al. Discriminating α-synuclein strains in Parkinson's disease and multiple system atrophy. *Nature*. 2020;578(7794):273-277. doi:10.1038/s41586-020-1984-7.

151 Guerrero-Ferreira R, Taylor NM, Mona D, et al. Cryo-EM structure of alpha-synuclein fibrils. *eLife*. 2018;7. doi:10.7554/eLife.36402.

152 Guerrero-Ferreira R, Taylor NM, Arteni A-A, et al. Two new polymorphic structures of human full-length alpha-synuclein fibrils solved by cryo-electron microscopy. *eLife*. 2019;8. doi:10.7554/eLife.48907.

153 Li Y, Zhao C, Luo F, et al. Amyloid fibril structure of α-synuclein determined by cryo-electron microscopy. *Cell Res*. 2018;28(9):897-903. doi:10.1038/s41422-018-0075-x.

154 Li B, Ge P, Murray KA, et al. Cryo-EM of full-length α-synuclein reveals fibril polymorphs with a common structural kernel. *Nat Commun*. 2018;9(1):3609. doi:10.1038/s41467-018-05971-2.

155 Danzer KM, Haasen D, Karow AR, et al. Different species of alpha-synuclein oligomers induce calcium influx and seeding. *J Neurosci*. 2007;27(34):9220-9232. doi:10.1523/JNEUROSCI.2617-07.2007.

156 Alam P, Bousset L, Melki R, Otzen DE. α-synuclein oligomers and fibrils: a spectrum of species, a spectrum of toxicities. *Journal of neurochemistry*. 2019;150(5):522-534. doi:10.1111/jnc.14808.

157 Eliezer D, Kutluay E, Bussell R, Browne G. Conformational properties of alpha-synuclein in its free and lipid-associated states. *Journal of Molecular Biology*. 2001;307(4):1061-1073. doi:10.1006/jmbi.2001.4538.

158 Fusco G, Simone A de, Gopinath T, et al. Direct observation of the three regions in α-synuclein that determine its membrane-bound behaviour. *Nat Commun*. 2014;5:3827. doi:10.1038/ncomms4827.

159 Yoo G, Shin Y-K, Lee NK. The Role of α-Synuclein in SNARE-mediated Synaptic Vesicle Fusion. *Journal of Molecular Biology*. 2023;435(1):167775. doi:10.1016/j.jmb.2022.167775.

160 Weber T, Zemelman BV, McNew JA, et al. SNAREpins: minimal machinery for membrane fusion. *Cell*. 1998;92(6):759-772. doi:10.1016/S0092-8674(00)81404-X.

161 Jahn R, Fasshauer D. Molecular machines governing exocytosis of synaptic vesicles. *Nature*. 2012;490(7419):201-207. doi:10.1038/nature11320.

162 Söllner T, Whiteheart SW, Brunner M, et al. SNAP receptors implicated in vesicle targeting and fusion. *Nature*. 1993;362(6418):318-324. doi:10.1038/362318a0.

163 Poirier MA, Xiao W, Macosko JC, Chan C, Shin YK, Bennett MK. The synaptic SNARE complex is a parallel four-stranded helical bundle. *Nat Struct Biol*. 1998;5(9):765-769. doi:10.1038/1799.

164 Xu Y, Zhang F, Su Z, McNew JA, Shin Y-K. Hemifusion in SNARE-mediated membrane fusion. *Nat Struct Mol Biol*. 2005;12(5):417-422. doi:10.1038/nsmb921.

165 Sarchione A, Marchand A, Taymans J-M, Chartier-Harlin M-C. Alpha-Synuclein and Lipids: The Elephant in the Room? *Cells*. 2021;10(9). doi:10.3390/cells10092452.

166 Sun J, Wang L, Bao H, et al. Functional cooperation of α-synuclein and VAMP2 in synaptic vesicle recycling. *Proc Natl Acad Sci U S A*. 2019;116(23):11113-11115. doi:10.1073/pnas.1903049116.

167 Burré J, Sharma M, Tsetsenis T, Buchman V, Etherton MR, Südhof TC. Alpha-synuclein promotes SNARE-complex assembly in vivo and in vitro. *Science*. 2010;329(5999):1663-1667. doi:10.1126/science.1195227.

168 Sharma M, Burré J. α-Synuclein in synaptic function and dysfunction. *Trends in Neurosciences*. 2023;46(2):153-166. doi:10.1016/j.tins.2022.11.007.

169 Abeliovich A, Schmitz Y, Fariñas I, et al. Mice lacking alpha-synuclein display functional deficits in the nigrostriatal dopamine system. *Neuron*. 2000;25(1):239-252. doi:10.1016/s0896-6273(00)80886-7.

170 Murphy DD, Rueter SM, Trojanowski JQ, Lee VM. Synucleins are developmentally expressed, and alpha-synuclein regulates the size of the presynaptic vesicular pool in primary hippocampal neurons. *J Neurosci*. 2000;20(9):3214-3220. doi:10.1523/JNEUROSCI.20-09-03214.2000.

171 Diao J, Burré J, Vivona S, et al. Native α-synuclein induces clustering of synaptic-vesicle mimics via binding to phospholipids and synaptobrevin-2/VAMP2. *eLife*. 2013;2:e00592. doi:10.7554/eLife.00592.

172 Wang L, Das U, Scott DA, Tang Y, McLean PJ, Roy S. α-synuclein multimers cluster synaptic vesicles and attenuate recycling. *Current biology : CB*. 2014;24(19):2319-2326. doi:10.1016/j.cub.2014.08.027.

173 Varkey J, Isas JM, Mizuno N, et al. Membrane curvature induction and tubulation are common features of synucleins and apolipoproteins. *Journal of Biological Chemistry*. 2010;285(42):32486-32493. doi:10.1074/jbc.M110.139576.

174 Man WK, Tahirbegi B, Vrettas MD, et al. The docking of synaptic vesicles on the presynaptic membrane induced by α-synuclein is modulated by lipid composition. *Nat Commun*. 2021;12(1):927. doi:10.1038/s41467-021-21027-4.

175 Wang W, Perovic I, Chittuluru J, et al. A soluble α-synuclein construct forms a dynamic tetramer. *Proc Natl Acad Sci U S A*. 2011;108(43):17797-17802. doi:10.1073/pnas.1113260108.

176 Burré J, Sharma M, Südhof TC. α-Synuclein assembles into higher-order multimers upon membrane binding to promote SNARE complex formation. *Proc Natl Acad Sci U S A*. 2014;111(40):E4274-83. doi:10.1073/pnas.1416598111.

177 Ghosh D, Mehra S, Sahay S, Singh PK, Maji SK. α-synuclein aggregation and its modulation. *International journal of biological macromolecules*. 2017;100:37-54. doi:10.1016/j.ijbiomac.2016.10.021.

178 Galvagnion C, Buell AK, Meisl G, et al. Lipid vesicles trigger α-synuclein aggregation by stimulating primary nucleation. *Nat Chem Biol*. 2015;11(3):229-234. doi:10.1038/nchembio.1750.

179 Antonschmidt L, Dervişoğlu R, Sant V, et al. Insights into the molecular mechanism of amyloid filament formation: Segmental folding of α-synuclein on lipid membranes. *Sci Adv*. 2021;7(20). doi:10.1126/sciadv.abg2174.

180 Fagerqvist T, Näsström T, Ihse E, et al. Off-pathway α-synuclein oligomers seem to alter α-synuclein turnover in a cell model but lack seeding capability in vivo. *Amyloid : the international journal of experimental and clinical investigation : the official journal of the International Society of Amyloidosis*. 2013;20(4):233-244. doi:10.3109/13506129.2013.835726.

181 Gaspar R, Meisl G, Buell AK, et al. Secondary nucleation of monomers on fibril surface dominates α-synuclein aggregation and provides autocatalytic amyloid amplification. *Quarterly reviews of biophysics*. 2017;50:e6. doi:10.1017/S0033583516000172.

182 Peduzzo A, Linse S, Buell AK. The Properties of α-Synuclein Secondary Nuclei Are Dominated by the Solution Conditions Rather than the Seed Fibril Strain. *ACS Chem Neurosci*. 2020;11(6):909-918. doi:10.1021/acschemneuro.9b00594.

183 Wood SJ, Wypych J, Steavenson S, Louis JC, Citron M, Biere AL. alpha-synuclein fibrillogenesis is nucleation-dependent. Implications for the pathogenesis of Parkinson's disease. *The Journal of Biological Chemistry*. 1999;274(28):19509-19512. doi:10.1074/jbc.274.28.19509.

184 Shvadchak VV, Claessens MMAE, Subramaniam V. Fibril breaking accelerates α-synuclein fibrillization. *The journal of physical chemistry. B*. 2015;119(5):1912-1918. doi:10.1021/jp5111604.

185 Buell AK, Galvagnion C, Gaspar R, et al. Solution conditions determine the relative importance of nucleation and growth processes in α-synuclein aggregation. *Proc Natl Acad Sci U S A*. 2014;111(21):7671-7676. doi:10.1073/pnas.1315346111.

186 Naiki H, Higuchi K, Hosokawa M, Takeda T. Fluorometric determination of amyloid fibrils in vitro using the fluorescent dye, thioflavin T1. *Analytical biochemistry*. 1989;177(2):244-249. doi:10.1016/0003-2697(89)90046-8.

187 Nelson R, Eisenberg D. Recent atomic models of amyloid fibril structure. *Curr Opin Struct Biol*. 2006;16(2):260-265. doi:10.1016/j.sbi.2006.03.007.

188 Sidhu A, Vaneyck J, Blum C, Segers-Nolten I, Subramaniam V. Polymorph-specific distribution of binding sites determines thioflavin-T fluorescence intensity in α-synuclein fibrils. *Amyloid : the international journal of experimental and clinical investigation : the official journal of the International Society of Amyloidosis*. 2018;25(3):189-196. doi:10.1080/13506129.2018.1517736.

189 Bousset L, Pieri L, Ruiz-Arlandis G, et al. Structural and functional characterization of two alpha-synuclein strains. *Nat Commun*. 2013;4:2575. doi:10.1038/ncomms3575.

190 Coelho-Cerqueira E, Pinheiro AS, Follmer C. Pitfalls associated with the use of Thioflavin-T to monitor anti-fibrillogenic activity. *Bioorganic & medicinal chemistry letters*. 2014;24(14):3194-3198. doi:10.1016/j.bmcl.2014.04.072.

191 Galvagnion C. The Role of Lipids Interacting with α-Synuclein in the Pathogenesis of Parkinson's Disease. *J Parkinsons Dis*. 2017;7(3):433-450. doi:10.3233/JPD-171103.

192 Mahul-Mellier A-L, Burtscher J, Maharjan N, et al. The process of Lewy body formation, rather than simply α-synuclein fibrillization, is one of the major drivers of neurodegeneration. *Proc Natl Acad Sci U S A*. 2020;117(9):4971-4982. doi:10.1073/pnas.1913904117.

193 Taschenberger G, Garrido M, Tereshchenko Y, Bähr M, Zweckstetter M, Kügler S. Aggregation of αSynuclein promotes progressive in vivo neurotoxicity in adult rat dopaminergic neurons. *Acta Neuropathol*. 2012;123(5):671-683. doi:10.1007/s00401-011-0926-8.

194 Gorbatyuk OS, Li S, Sullivan LF, et al. The phosphorylation state of Ser-129 in human alpha-synuclein determines neurodegeneration in a rat model of Parkinson disease. *Proc Natl Acad Sci U S A*. 2008;105(2):763-768. doi:10.1073/pnas.0711053105.

195 Winner B, Jappelli R, Maji SK, et al. In vivo demonstration that alpha-synuclein oligomers are toxic. *Proc Natl Acad Sci U S A*. 2011;108(10):4194-4199. doi:10.1073/pnas.1100976108.

196 Ito N, Tsuji M, Adachi N, et al. Extracellular high molecular weight α-synuclein oligomers induce cell death by disrupting the plasma membrane. *NPJ Parkinsons Dis*. 2023;9(1):139. doi:10.1038/s41531-023-00583-0.

197 Scott DA, Tabarean I, Tang Y, Cartier A, Masliah E, Roy S. A pathologic cascade leading to synaptic dysfunction in alpha-synuclein-induced neurodegeneration. *J Neurosci*. 2010;30(24):8083-8095. doi:10.1523/JNEUROSCI.1091-10.2010.

198 Alim MA, Ma Q-L, Takeda K, et al. Demonstration of a role for alpha-synuclein as a functional microtubule-associated protein. *J Alzheimers Dis*. 2004;6(4):435-42; discussion 443-9. doi:10.3233/jad-2004-6412.

199 Kim H-Y, Cho M-K, Kumar A, et al. Structural properties of pore-forming oligomers of alpha-synuclein. *J Am Chem Soc*. 2009;131(47):17482-17489. doi:10.1021/ja9077599.

200 Hsu LJ, Sagara Y, Arroyo A, et al. alpha-synuclein promotes mitochondrial deficit and oxidative stress. *The American Journal of Pathology*. 2000;157(2):401-410. doi:10.1016/s0002-9440(10)64553-1.

201 Choi ML, Chappard A, Singh BP, et al. Pathological structural conversion of α-synuclein at the mitochondria induces neuronal toxicity. *Nat Neurosci*. 2022;25(9):1134-1148. doi:10.1038/s41593-022-01140-3.

202 Lee J-E, Sang JC, Rodrigues M, et al. Mapping Surface Hydrophobicity of α-Synuclein Oligomers at the Nanoscale. *Nano Lett*. 2018;18(12):7494-7501. doi:10.1021/acs.nanolett.8b02916.

203 Chartier-Harlin M-C, Kachergus J, Roumier C, et al. Alpha-synuclein locus duplication as a cause of familial Parkinson's disease. *Lancet (London, England)*. 2004;364(9440):1167-1169. doi:10.1016/S0140-6736(04)17103-1.

204 Singleton AB, Farrer M, Johnson J, et al. alpha-Synuclein locus triplication causes Parkinson's disease. *Science*. 2003;302(5646):841. doi:10.1126/science.1090278.

205 Maraganore DM, Andrade M de, Elbaz A, et al. Collaborative analysis of alpha-synuclein gene promoter variability and Parkinson disease. *JAMA*. 2006;296(6):661-670. doi:10.1001/jama.296.6.661.

206 Krüger R, Kuhn W, Müller T, et al. Ala30Pro mutation in the gene encoding alpha-synuclein in Parkinson's disease. *Nature genetics*. 1998;18(2):106-108. doi:10.1038/ng0298-106.

207 Zarranz JJ, Alegre J, Gómez-Esteban JC, et al. The new mutation, E46K, of alpha-synuclein causes Parkinson and Lewy body dementia. *Annals of neurology*. 2004;55(2):164-173. doi:10.1002/ana.10795.

208 Proukakis C, Dudzik CG, Brier T, et al. A novel α-synuclein missense mutation in Parkinson disease. *Neurology*. 2013;80(11):1062-1064. doi:10.1212/WNL.0b013e31828727ba.

209 Lesage S, Anheim M, Letournel F, et al. G51D α-synuclein mutation causes a novel parkinsonian-pyramidal syndrome. *Annals of neurology*. 2013;73(4):459-471. doi:10.1002/ana.23894.

210 Pasanen P, Myllykangas L, Siitonen M, et al. Novel α-synuclein mutation A53E associated with atypical multiple system atrophy and Parkinson's disease-type pathology. *Neurobiology of aging*. 2014;35(9):2180.e1-5. doi:10.1016/j.neurobiolaging.2014.03.024.

211 Yoshino H, Hirano M, Stoessl AJ, et al. Homozygous alpha-synuclein p.A53V in familial Parkinson's disease. *Neurobiology of aging*. 2017;57:248.e7-248.e12. doi:10.1016/j.neurobiolaging.2017.05.022.

212 B. Minafra, G. Buongarzone, S. Gana, M.L Valente, I. Palmieri, T. Biagini, M. Plumari, M. Avenali, R. Zangaglia, T. Mazza, C. Cereda, C. Pacchetti, E.M Valente. A novel likely pathogenic SNCA variant associated with Parkinson’s disease [abstract]. Mov Disord. 2020; 35 (suppl 1). https://www.mdsabstracts.org/abstract/a-novel-likely-pathogenic-snca-variant-associated-with-parkinsons-disease/. Updated February 24, 2024. Accessed February 24, 2024.

213 Daida K, Shimonaka S, Shiba-Fukushima K, et al. α-Synuclein V15A Variant in Familial Parkinson's Disease Exhibits a Weaker Lipid-Binding Property. *Mov Disord*. 2022;37(10):2075-2085. doi:10.1002/mds.29162.

214 Flagmeier P, Meisl G, Vendruscolo M, et al. Mutations associated with familial Parkinson's disease alter the initiation and amplification steps of α-synuclein aggregation. *Proc Natl Acad Sci U S A*. 2016;113(37):10328-10333. doi:10.1073/pnas.1604645113.

215 Mehra S, Gadhe L, Bera R, Sawner AS, Maji SK. Structural and Functional Insights into α-Synuclein Fibril Polymorphism. *Biomolecules*. 2021;11(10). doi:10.3390/biom11101419.

216 Conway KA, Lee SJ, Rochet JC, Ding TT, Williamson RE, Lansbury PT. Acceleration of oligomerization, not fibrillization, is a shared property of both alpha-synuclein mutations linked to early-onset Parkinson's disease: implications for pathogenesis and therapy. *Proc Natl Acad Sci U S A*. 2000;97(2):571-576. doi:10.1073/pnas.97.2.571.

217 Sun Y, Long H, Xia W, et al. The hereditary mutation G51D unlocks a distinct fibril strain transmissible to wild-type α-synuclein. *Nat Commun*. 2021;12(1):6252. doi:10.1038/s41467-021-26433-2.

218 Sun Y, Hou S, Zhao K, et al. Cryo-EM structure of full-length α-synuclein amyloid fibril with Parkinson's disease familial A53T mutation. *Cell Res*. 2020;30(4):360-362. doi:10.1038/s41422-020-0299-4.

219 Lima VdA, do Nascimento LA, Eliezer D, Follmer C. Role of Parkinson's Disease-Linked Mutations and N-Terminal Acetylation on the Oligomerization of α-Synuclein Induced by 3,4-Dihydroxyphenylacetaldehyde. *ACS Chem Neurosci*. 2019;10(1):690-703. doi:10.1021/acschemneuro.8b00498.

220 Ysselstein D, Joshi M, Mishra V, et al. Effects of impaired membrane interactions on α-synuclein aggregation and neurotoxicity. *Neurobiol Dis*. 2015;79:150-163. doi:10.1016/j.nbd.2015.04.007.

221 Chen H, Zhao Y-F, Chen Y-X, Li Y-M. Exploring the Roles of Post-Translational Modifications in the Pathogenesis of Parkinson's Disease Using Synthetic and Semisynthetic Modified α-Synuclein. *ACS Chem Neurosci*. 2019;10(2):910-921. doi:10.1021/acschemneuro.8b00447.

222 Baba M, Nakajo S, Tu PH, et al. Aggregation of alpha-synuclein in Lewy bodies of sporadic Parkinson's disease and dementia with Lewy bodies. *The American Journal of Pathology*. 1998;152(4):879-884.

223 Maltsev AS, Ying J, Bax A. Impact of N-terminal acetylation of α-synuclein on its random coil and lipid binding properties. *Biochemistry*. 2012;51(25):5004-5013. doi:10.1021/bi300642h.

224 Ruzafa D, Hernandez-Gomez YS, Bisello G, Broersen K, Morel B, Conejero-Lara F. The influence of N-terminal acetylation on micelle-induced conformational changes and aggregation of α-Synuclein. *PLoS One*. 2017;12(5):e0178576. doi:10.1371/journal.pone.0178576.

225 Fujiwara H, Hasegawa M, Dohmae N, et al. alpha-Synuclein is phosphorylated in synucleinopathy lesions. *Nat Cell Biol*. 2002;4(2):160-164. doi:10.1038/ncb748.

226 Anderson JP, Walker DE, Goldstein JM, et al. Phosphorylation of Ser-129 is the dominant pathological modification of alpha-synuclein in familial and sporadic Lewy body disease. *The Journal of Biological Chemistry*. 2006;281(40):29739-29752. doi:10.1074/jbc.M600933200.

227 Alfaro JF, Gong C-X, Monroe ME, et al. Tandem mass spectrometry identifies many mouse brain O-GlcNAcylated proteins including EGF domain-specific O-GlcNAc transferase targets. *Proc Natl Acad Sci U S A*. 2012;109(19):7280-7285. doi:10.1073/pnas.1200425109.

228 Dorval V, Fraser PE. Small ubiquitin-like modifier (SUMO) modification of natively unfolded proteins tau and alpha-synuclein. *The Journal of Biological Chemistry*. 2006;281(15):9919-9924. doi:10.1074/jbc.M510127200.

229 Giasson BI, Duda JE, Murray IV, et al. Oxidative damage linked to neurodegeneration by selective alpha-synuclein nitration in synucleinopathy lesions. *Science*. 2000;290(5493):985-989. doi:10.1126/science.290.5493.985.

230 Nonaka T, Iwatsubo T, Hasegawa M. Ubiquitination of alpha-synuclein. *Biochemistry*. 2005;44(1):361-368. doi:10.1021/bi0485528.

231 Sanyal A, Dutta S, Camara A, et al. Alpha-Synuclein Is a Target of Fic-Mediated Adenylylation/AMPylation: Possible Implications for Parkinson's Disease. *Journal of Molecular Biology*. 2019;431(12):2266-2282. doi:10.1016/j.jmb.2019.04.026.

232 Uversky VN, Yamin G, Souillac PO, Goers J, Glaser CB, Fink AL. Methionine oxidation inhibits fibrillation of human alpha-synuclein in vitro. *FEBS Lett*. 2002;517(1-3):239-244. doi:10.1016/s0014-5793(02)02638-8.

233 Vicente Miranda H, Szego ÉM, Oliveira LMA, et al. Glycation potentiates α-synuclein-associated neurodegeneration in synucleinopathies. *Brain*. 2017;140(5):1399-1419. doi:10.1093/brain/awx056.

234 Bell R, Vendruscolo M. Modulation of the Interactions Between α-Synuclein and Lipid Membranes by Post-translational Modifications. *Frontiers in Neurology*. 2021;12:661117. doi:10.3389/fneur.2021.661117.

235 Schmid AW, Fauvet B, Moniatte M, Lashuel HA. Alpha-synuclein post-translational modifications as potential biomarkers for Parkinson disease and other synucleinopathies. *Mol Cell Proteomics*. 2013;12(12):3543-3558. doi:10.1074/mcp.R113.032730.

236 Tuttle MD, Comellas G, Nieuwkoop AJ, et al. Solid-state NMR structure of a pathogenic fibril of full-length human α-synuclein. *Nat Struct Mol Biol*. 2016;23(5):409-415. doi:10.1038/nsmb.3194.

237 Fantini J, Yahi N. Molecular basis for the glycosphingolipid-binding specificity of α-synuclein: key role of tyrosine 39 in membrane insertion. *Journal of Molecular Biology*. 2011;408(4):654-669. doi:10.1016/j.jmb.2011.03.009.

238 Doherty CPA, Ulamec SM, Maya-Martinez R, et al. A short motif in the N-terminal region of α-synuclein is critical for both aggregation and function. *Nat Struct Mol Biol*. 2020;27(3):249-259. doi:10.1038/s41594-020-0384-x.

239 Ulamec SM, Maya-Martinez R, Byrd EJ, et al. Single residue modulators of amyloid formation in the N-terminal P1-region of α-synuclein. *Nat Commun*. 2022;13(1):4986. doi:10.1038/s41467-022-32687-1.

240 Aubrey LD, Ninkina N, Ulamec SM, et al. Substitution of Met-38 to Ile in γ-synuclein found in two patients with amyotrophic lateral sclerosis induces aggregation into amyloid. *Proc Natl Acad Sci U S A*. 2024;121(2):e2309700120. doi:10.1073/pnas.2309700120.

241 Santos J, Cuellar J, Pallarès I, et al. *The structural architecture of an α-synuclein toxic oligomer*; 2023.

242 Ulrih NP, Barry CH, Fink AL. Impact of Tyr to Ala mutations on alpha-synuclein fibrillation and structural properties. *Biochim Biophys Acta*. 2008;1782(10):581-585. doi:10.1016/j.bbadis.2008.07.004.

243 Lamberto GR, Binolfi A, Orcellet ML, et al. Structural and mechanistic basis behind the inhibitory interaction of PcTS on alpha-synuclein amyloid fibril

formation. *Proc Natl Acad Sci U S A*. 2009;106(50):21057-21062. doi:10.1073/pnas.0902603106.

244 Palomino-Hernandez O, Buratti FA, Sacco PS, Rossetti G, Carloni P, Fernandez CO. Role of Tyr-39 for the Structural Features of α-Synuclein and for the Interaction with a Strong Modulator of Its Amyloid Assembly. *Int J Mol Sci*. 2020;21(14). doi:10.3390/ijms21145061.

245 Burmann BM, Gerez JA, Matečko-Burmann I, et al. Regulation of α-synuclein by chaperones in mammalian cells. *Nature*. 2020;577(7788):127-132. doi:10.1038/s41586-019-1808-9.

246 Brahmachari S, Ge P, Lee SH, et al. Activation of tyrosine kinase c-Abl contributes to α-synuclein-induced neurodegeneration. *J Clin Invest*. 2016;126(8):2970-2988. doi:10.1172/JCI85456.

247 Mahul-Mellier A-L, Fauvet B, Gysbers A, et al. c-Abl phosphorylates α-synuclein and regulates its degradation: implication for α-synuclein clearance and contribution to the pathogenesis of Parkinson's disease. *Hum Mol Genet*. 2014;23(11):2858-2879. doi:10.1093/hmg/ddt674.

248 Brenner S. THE GENETICS OF CAENORHABDITIS ELEGANS. *Genetics*. 1974;77(1):71-94. doi:10.1093/genetics/77.1.71.

249 A Transparent window into biology: A primer on Caenorhabditis elegans. http://www.wormbook.org/chapters/www_celegansintro/celegansintro.html. Updated November 3, 2023. Accessed November 3, 2023.

250 Raizen DM, Zimmerman JE, Maycock MH, et al. Lethargus is a Caenorhabditis elegans sleep-like state. *Nature*. 2008;451(7178):569-572. doi:10.1038/nature06535.

251 Hu PJ. Dauer. *WormBook*. 2007:1-19. doi:10.1895/wormbook.1.144.1.

252 Altun ZF, Hall DH. WormAtas Hermaphrodite Handbook - Introduction. *WormAtlas*. 2006. doi:10.3908/wormatlas.1.1.

253 Culetto E, Sattelle DB. A role for Caenorhabditis elegans in understanding the function and interactions of human disease genes. *Hum Mol Genet*. 2000;9(6):869-877. doi:10.1093/hmg/9.6.869.

254 Shaye DD, Greenwald I. OrthoList: a compendium of C. elegans genes with human orthologs. *PLoS One*. 2011;6(5):e20085. doi:10.1371/journal.pone.0020085.

255 Giunti S, Andersen N, Rayes D, Rosa MJ de. Drug discovery: Insights from the invertebrate Caenorhabditis elegans. *Pharmacol Res Perspect*. 2021;9(2):e00721. doi:10.1002/prp2.721.

256 Hughes S, van Dop M, Kolsters N, van de Klashorst D, Pogosova A, Rijs AM. Using a Caenorhabditis elegans Parkinson's Disease Model to Assess Disease Progression and Therapy Efficiency. *Pharmaceuticals (Basel)*. 2022;15(5). doi:10.3390/ph15050512.

257 White JG, Southgate E, Thomson JN, Brenner S. The structure of the ventral nerve cord of Caenorhabditis elegans. *Philos Trans R Soc Lond B Biol Sci*. 1976;275(938):327-348. doi:10.1098/rstb.1976.0086.

258 White JG, Southgate E, Thomson JN, Brenner S. The structure of the nervous system of the nematode Caenorhabditis elegans. *Philos Trans R Soc Lond B Biol Sci*. 1986;314(1165):1-340. doi:10.1098/rstb.1986.0056.

259 Hobson RJ, Yook KJ, Jorgensen EM. Genetics of Neurotransmitter Release in Caenorhabditis elegans ☆. In: *Elsevier Reference Collection in Life Sciences*. [S. l.]: Elsevier; 2016-.

260 Sawin ER, Ranganathan R, Horvitz HR. C. elegans locomotory rate is modulated by the environment through a dopaminergic pathway and by experience through a serotonergic pathway. *Neuron*. 2000;26(3):619-631. doi:10.1016/s0896-6273(00)81199-x.

261 Lakso M, Vartiainen S, Moilanen A-M, et al. Dopaminergic neuronal loss and motor deficits in Caenorhabditis elegans overexpressing human alpha-synuclein. *Journal of neurochemistry*. 2003;86(1):165-172. doi:10.1046/j.1471-4159.2003.01809.x.

262 Ali SJ, Rajini PS. Elicitation of dopaminergic features of Parkinson's disease in C. elegans by monocrotophos, an organophosphorous insecticide. *CNS Neurol Disord Drug Targets*. 2012;11(8):993-1000. doi:10.2174/1871527311211080008.

263 Pu P, Le W. Dopamine neuron degeneration induced by MPP+ is independent of CED-4 pathway in Caenorhabditis elegans. *Cell Res*. 2008;18(9):978-981. doi:10.1038/cr.2008.279.

264 Nass R, Hall DH, Miller DM, Blakely RD. Neurotoxin-induced degeneration of dopamine neurons in Caenorhabditis elegans. *Proc Natl Acad Sci U S A*. 2002;99(5):3264-3269. doi:10.1073/pnas.042497999.

265 Chen Z, Cole PA. Synthetic approaches to protein phosphorylation. *Curr Opin Chem Biol*. 2015;28:115-122. doi:10.1016/j.cbpa.2015.07.001.

266 Kliche J, Garvanska DH, Simonetti L, et al. Large-scale phosphomimetic screening identifies phospho-modulated motif-based protein interactions. *Mol Syst Biol*. 2023;19(7):e11164. doi:10.15252/msb.202211164.

267 Stateva SR, Salas V, Benaim G, Menéndez M, Solís D, Villalobo A. Characterization of phospho-(tyrosine)-mimetic calmodulin mutants. *PLoS One*. 2015;10(4):e0120798. doi:10.1371/journal.pone.0120798.

268 Laemmli UK. Cleavage of structural proteins during the assembly of the head of bacteriophage T4. *Nature*. 1970;227(5259):680-685. doi:10.1038/227680a0.

269 Bertoncini CW, Jung Y-S, Fernandez CO, et al. Release of long-range tertiary interactions potentiates aggregation of natively unstructured alpha-synuclein. *Proc Natl Acad Sci U S A*. 2005;102(5):1430-1435. doi:10.1073/pnas.0407146102.

270 Cho M-K, Nodet G, Kim H-Y, et al. Structural characterization of alpha-synuclein in an aggregation prone state. *Protein Sci*. 2009;18(9):1840-1846. doi:10.1002/pro.194.

271 Ranjbar B, Gill P. Circular dichroism techniques: biomolecular and nanostructural analyses- a review. *Chem Biol Drug Des*. 2009;74(2):101-120. doi:10.1111/j.1747-0285.2009.00847.x.

272 Vranken WF, Boucher W, Stevens TJ, et al. The CCPN data model for NMR spectroscopy: development of a software pipeline. *Proteins*. 2005;59(4):687-696. doi:10.1002/prot.20449.

273 Bartels T, Ahlstrom LS, Leftin A, et al. The N-terminus of the intrinsically disordered protein α-synuclein triggers membrane binding and helix folding. *Biophys J*. 2010;99(7):2116-2124. doi:10.1016/j.bpj.2010.06.035.

274 Serrano L. Comparison between the phi distribution of the amino acids in the protein database and NMR data indicates that amino acids have various phi propensities in the random coil conformation. *Journal of Molecular Biology*. 1995;254(2):322-333. doi:10.1006/jmbi.1995.0619.

275 Altieri AS, Hinton DP, Byrd RA. Association of Biomolecular Systems via Pulsed Field Gradient NMR Self-Diffusion Measurements. *J Am Chem Soc*. 1995;117(28):7566-7567. doi:10.1021/ja00133a039.

276 Bernadó P, La García de Torre J, Pons M. Macromolecular crowding in biological systems: hydrodynamics and NMR methods. *J Mol Recognit*. 2004;17(5):397-407. doi:10.1002/jmr.694.

277 Pan H, Barany G, Woodward C. Reduced BPTI is collapsed. A pulsed field gradient NMR study of unfolded and partially folded bovine pancreatic trypsin inhibitor. *Protein Sci*. 1997;6(9):1985-1992. doi:10.1002/pro.5560060919.

278 Kumar P, Nagarajan A, Uchil PD. Analysis of Cell Viability by the MTT Assay. *Cold Spring Harb Protoc*. 2018;2018(6). doi:10.1101/pdb.prot095505.

279 Chung KK, Zhang Y, Lim KL, et al. Parkin ubiquitinates the alpha-synuclein-interacting protein, synphilin-1: implications for Lewy-body formation in Parkinson disease. *Nat Med*. 2001;7(10):1144-1150. doi:10.1038/nm1001-1144.

280 Lázaro DF, Rodrigues EF, Langohr R, et al. Systematic comparison of the effects of alpha-synuclein mutations on its oligomerization and aggregation. *PLoS Genet*. 2014;10(11):e1004741. doi:10.1371/journal.pgen.1004741.

281 Masaracchia C, König A, Valiente-Gabioud AA, et al. Molecular characterization of an aggregation-prone variant of alpha-synuclein used to model synucleinopathies. *Biochim Biophys Acta Proteins Proteom*. 2020;1868(1):140298. doi:10.1016/j.bbapap.2019.140298.

282 Towbin H, Staehelin T, Gordon J. Electrophoretic transfer of proteins from polyacrylamide gels to nitrocellulose sheets: procedure and some applications. *Proc Natl Acad Sci U S A*. 1979;76(9):4350-4354. doi:10.1073/pnas.76.9.4350.

283 Mezei LM, Storts D. *Purification of PCR products. In: PCR Technology: Current Innovations, Griffin, H.G. and Griffin, A.M., eds., CRC Press, Boca Raton, FL, 21;* 1994.

284 Zhou MY, Clark SE, Gomez-Sanchez CE. Universal cloning method by TA strategy. *Biotechniques*. 1995;19(1):34-35.

285 Mello C, Fire A. Chapter 19 DNA Transformation. In: Epstein HF, Shakes DC, eds. *Methods in Cell Biology : Cuenorhubditis elegans: Modern Biologcal Analysis of an Organism*. Vol. 48: Academic Press; 1995:451-482.

286 Shumay E, Fowler JS, Volkow ND. Genomic features of the human dopamine transporter gene and its potential epigenetic States: implications for phenotypic diversity. *PLoS One*. 2010;5(6):e11067. doi:10.1371/journal.pone.0011067.

287 Ochoa D, Jarnuczak AF, Viéitez C, et al. The functional landscape of the human phosphoproteome. *Nat Biotechnol*. 2020;38(3):365-373. doi:10.1038/s41587-019-0344-3.

288 Krause DS, van Etten RA. Tyrosine kinases as targets for cancer therapy. *N Engl J Med*. 2005;353(2):172-187. doi:10.1056/NEJMra044389.

289 Zhang J, Yang PL, Gray NS. Targeting cancer with small molecule kinase inhibitors. *Nat Rev Cancer*. 2009;9(1):28-39. doi:10.1038/nrc2559.

290 Dikiy I, Fauvet B, Jovičić A, et al. Semisynthetic and in Vitro Phosphorylation of Alpha-Synuclein at Y39 Promotes Functional Partly Helical Membrane-Bound States Resembling Those Induced by PD Mutations. *ACS Chem Biol*. 2016;11(9):2428-2437. doi:10.1021/acschembio.6b00539.

291 Pan B, Rhoades E, Petersson EJ. Chemoenzymatic Semisynthesis of Phosphorylated α-Synuclein Enables Identification of a Bidirectional Effect on Fibril Formation. *ACS Chem Biol*. 2020;15(3):640-645. doi:10.1021/acschembio.9b01038.

292 Fonseca-Ornelas L, Schmidt C, Camacho-Zarco AR, Fernandez CO, Becker S, Zweckstetter M. Small-Molecule-Induced Soluble Oligomers of α-Synuclein with Helical Structure. *Chemistry*. 2017;23(53):13010-13014. doi:10.1002/chem.201703001.

293 Kumar H, Singh J, Kumari P, Udgaonkar JB. Modulation of the extent of structural heterogeneity in α-synuclein fibrils by the small molecule thioflavin T. *Journal of Biological Chemistry*. 2017;292(41):16891-16903. doi:10.1074/jbc.M117.795617.

294 Sulatskaya AI, Sulatsky MI, Antifeeva IA, Kuznetsova IM, Turoverov KK. Structural Analogue of Thioflavin T, DMASEBT, as a Tool for Amyloid Fibrils Study. *Anal Chem*. 2019;91(4):3131-3140. doi:10.1021/acs.analchem.8b05737.

295 Yakupova EI, Bobyleva LG, Vikhlyantsev IM, Bobylev AG. Congo Red and amyloids: history and relationship. *Biosci Rep*. 2019;39(1). doi:10.1042/BSR20181415.

296 Fonseca-Ornelas L, Eisbach SE, Paulat M, et al. Small molecule-mediated stabilization of vesicle-associated helical α-synuclein inhibits pathogenic misfolding and aggregation. *Nat Commun*. 2014;5:5857. doi:10.1038/ncomms6857.

297 Zhang S, Zhu R, Pan B, et al. Post-translational modifications of soluble α-synuclein regulate the amplification of pathological α-synuclein. *Nat Neurosci*. 2023;26(2):213-225. doi:10.1038/s41593-022-01239-7.

298 Hebron ML, Lonskaya I, Moussa CE-H. Nilotinib reverses loss of dopamine neurons and improves motor behavior via autophagic degradation of α-synuclein in Parkinson's disease models. *Hum Mol Genet*. 2013;22(16):3315-3328. doi:10.1093/hmg/ddt192.

299 Fan C, Ip K, Söll D. Expanding the genetic code of Escherichia coli with phosphotyrosine. *FEBS Lett*. 2016;590(17):3040-3047. doi:10.1002/1873-3468.12333.

300 Hoppmann C, Wong A, Yang B, et al. Site-specific incorporation of phosphotyrosine using an expanded genetic code. *Nat Chem Biol*. 2017;13(8):842-844. doi:10.1038/nchembio.2406.

301 Pan B, Park JH, Ramlall T, Eliezer D, Rhoades E, Petersson EJ. Chemoenzymatic Semi-synthesis Enables Efficient Production of Isotopically Labeled α-Synuclein with Site-Specific Tyrosine Phosphorylation. *Chembiochem*. 2021;22(8):1440-1447. doi:10.1002/cbic.202000742.

302 Zhao K, Lim Y-J, Liu Z, et al. Parkinson's disease-related phosphorylation at Tyr39 rearranges α-synuclein amyloid fibril structure revealed by cryo-EM. *Proc Natl Acad Sci U S A*. 2020;117(33):20305-20315. doi:10.1073/pnas.1922741117.

303 Kwon S-H, Kim S, Park AY, et al. A Novel, Selective c-Abl Inhibitor, Compound 5, Prevents Neurodegeneration in Parkinson's Disease. *J Med Chem*. 2021;64(20):15091-15110. doi:10.1021/acs.jmedchem.1c01022.

304 Moujalled D, Strasser A, Liddell JR. Molecular mechanisms of cell death in neurological diseases. *Cell Death Differ*. 2021;28(7):2029-2044. doi:10.1038/s41418-021-00814-y.

305 Lin K-J, Chen S-D, Lin K-L, et al. Iron Brain Menace: The Involvement of Ferroptosis in Parkinson Disease. *Cells*. 2022;11(23). doi:10.3390/cells11233829.

306 Mahoney-Sánchez L, Bouchaoui H, Ayton S, Devos D, Duce JA, Devedjian J-C. Ferroptosis and its potential role in the physiopathology of Parkinson's Disease. *Prog Neurobiol*. 2021;196:101890. doi:10.1016/j.pneurobio.2020.101890.

7 Appendix

7.1 Plasmid Maps

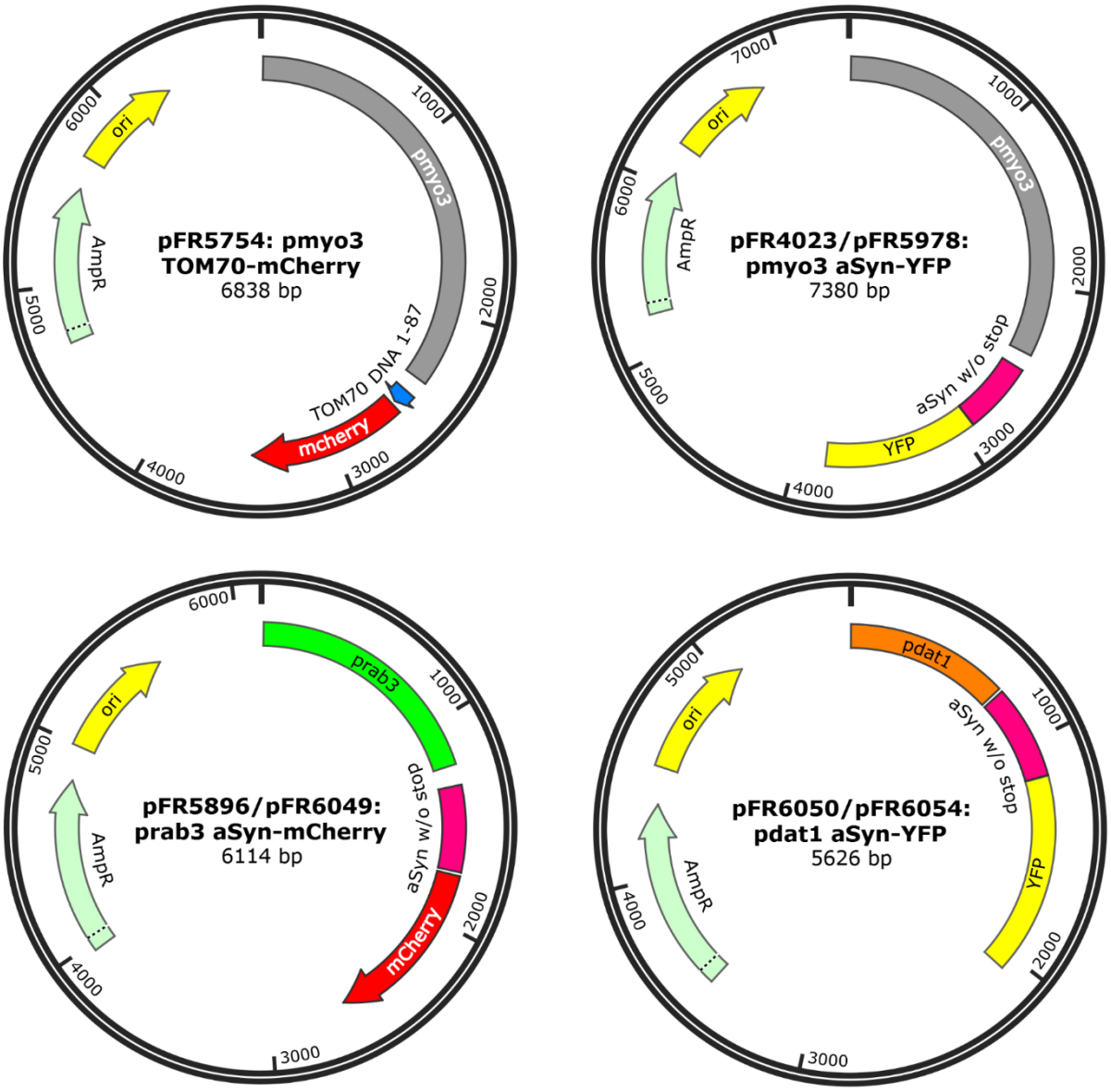

Supplementary Figure 1: Plasmid maps of pFR5754, pFR4023/5978, pFR5896/6049 and pFR6050/6054.

7.2 NMR Pulse Programs and Acquisition Parameters

1D ^{1}H-NMR:

Details:

Temperature: 15 °C
Spectral width: 12 ppm
Complex points: 8192
Acquisition time: 0.568 sec
Relaxation time delay: 1 sec
Number of scans: 256

Pulse program: zgesgp

```
;zgesgp
;avance-version (12/01/11)
;1D sequence
;water suppression using excitation sculpting with gradients
;T.-L. Hwang & A.J. Shaka, J. Magn. Reson.,
;   Series A 112 275-279 (1995)
;$CLASS=HighRes
;$DIM=1D
;$TYPE=
;$SUBTYPE=
;$COMMENT=
prosol relations=<triple>
#include <Avance.incl>
#include <Grad.incl>
#include <Delay.incl>
"p2=p1*2"
"d12=20u"
"TAU=de+p1*2/3.1416+50u"
"acqt0=0"
baseopt_echo
```

```
1 ze
2 30m
  d12 pl1:f1 BLKGRAD
  d1
  p1 ph1
  50u UNBLKGRAD
  p16:gp1
  d16 pl0:f1
  (p12:sp1 ph2:r):f1
  4u
  d12 pl1:f1
  p2 ph3
  4u
  p16:gp1
  d16
  TAU
  p16:gp2
  d16 pl0:f1
  (p12:sp1 ph4:r):f1
  4u
  d12 pl1:f1
  p2 ph5
  4u
  p16:gp2
  d16
  go=2 ph31
  30m mc #0 to 2 F0(zd)
  4u BLKGRAD
exit
ph1=0
ph2=0 1
ph3=2 3
ph4=0 0 1 1
ph5=2 2 3 3
```

ph31=0 2 2 0
;pl0 : 0W
;pl1 : f1 channel - power level for pulse (default)
;sp1 : f1 channel - shaped pulse 180 degree
;p1 : f1 channel - 90 degree high power pulse
;p2 : f1 channel - 180 degree high power pulse
;p12: f1 channel - 180 degree shaped pulse (Squa100.1000) [2 msec]
;p16: homospoil/gradient pulse
;d1 : relaxation delay; 1-5 * T1
;d12: delay for power switching [20 usec]
;d16: delay for homospoil/gradient recovery
;ns: 8 * n, total number of scans: NS * TD0
;ds: 4

;use gradient ratio: gp 1 : gp 2
; 31 : 11
;for z-only gradients:
;gpz1: 31%
;gpz2: 11%
;use gradient files:
;gpnam1: SMSQ10.100
;gpnam2: SMSQ10.100
;$Id: zgesgp,v 1.9 2012/01/31 17:49:32 ber Exp $

2D HSQC:

Details:

Temperature: 15 °C
Spectral width: 12 ppm (direct dimension ^{1}H), 22 ppm (indirect dimension ^{15}N)
Complex points: 2048 (^{1}H), 256 (^{15}N)
Acquisition time: 0.142 sec
Relaxation time delay: 1 sec
Number of scans: 512

Pulse program: hsqcfpf3gpphwg

```
;hsqcfpf3gpphwg
;avance-version (12/01/11)
;HSQC
;2D H-1/X correlation via double inept transfer
;phase sensitive
;with decoupling during acquisition
;using f3 - channel
;using flip-back pulse
;water suppression using watergate sequence
;similar to fhsqc
;(use parameterset HSQCFPF3GPPHWG)
;G. Bodenhausen & D.J. Ruben, Chem. Phys. Lett. 69, 185 (1980)
;M. Piotto, V. Saudek & V. Sklenar, J. Biomol. NMR 2, 661 - 666 (1992)
;V. Sklenar, M. Piotto, R. Leppik & V. Saudek, J. Magn. Reson.,
;   Series A 102, 241 -245 (1993)
;S. Mori, C. Abeygunawardana, M. O'Neil-Johnson & P.C.M. van Zijl,
;   J. Magn. Reson. B 108, 94-98 (1995)
;$CLASS=HighRes
;$DIM=2D
;$TYPE=
;$SUBTYPE=
;$COMMENT=

prosol relations=<triple>
#include <Avance.incl>
#include <Delay.incl>
#include <Grad.incl>
"p2=p1*2"
"p22=p21*2"
"d11=30m"
"d12=20u"
```

```
"d26=1s/(cnst4*4)"
"d0=3u"
"in0=inf1/2"
"DELTA1=d26-p16-d16"
"DELTA2=d26-p16-d16-p11-12u"
#   ifdef LABEL_CN
"DELTA=d0*2+larger(p2,p8)"
#   else
"DELTA=d0*2+p2"
#   endif /*LABEL_CN*/
1 ze
  d11 pl16:f3
2 d1 do:f3
3 d12 pl1:f1 pl3:f3
  50u UNBLKGRAD
  (p1 ph1)
  p16:gp3
  d16
  DELTA1
  (center (p2 ph2) (p22 ph6):f3 )
  DELTA1
  p16:gp3
  d16
  (p1 ph2)

  4u pl0:f1
  (p11:sp1 ph8:r):f1
  4u
  p16:gp4
  d16 pl1:f1
  (p21 ph3):f3
  d0
#   ifdef LABEL_CN
  (center (p2 ph5) (p8:sp13 ph1):f2 )
```

```
#   else
  (p2 ph5)
#   endif /*LABEL_CN*/
  d0
  (p22 ph4):f3
  DELTA
  (p21 ph4):f3
  4u
  p16:gp4
  d16 pl0:f1
  (p11:sp1 ph7:r):f1
  4u
  4u pl1:f1
  (p1 ph1)
  4u
  p16:gp5
  d16
  DELTA2 pl0:f1
  (p11:sp1 ph7:r):f1
  4u
  4u pl1:f1
  (center (p2 ph1) (p22 ph1):f3 )
  4u pl0:f1
  (p11:sp1 ph7:r):f1
  4u
  p16:gp5
  d16
  DELTA2 pl16:f3
  4u BLKGRAD
  go=2 ph31 cpd3:f3
  d1 do:f3 mc #0 to 2 F1PH(calph(ph3, +90) & calph(ph6, +90), caldel(d0, +in0))
exit
ph1=0
ph2=1
```

```
ph3=0 2
ph4=0 0 0 0 2 2 2 2
ph5=0 0 2 2
ph6=0
ph7=2
ph8=0
ph31=0 2 0 2 2 0 2 0
;pl0 : 0W
;pl1 : f1 channel - power level for pulse (default)
;pl3 : f3 channel - power level for pulse (default)
;pl16: f3 channel - power level for CPD/BB decoupling
;sp1: f1 channel - shaped pulse  90 degree
;sp13: f2 channel - shaped pulse 180 degree (adiabatic)
;p1 : f1 channel -  90 degree high power pulse
;p2 : f1 channel - 180 degree high power pulse
;p8 : f2 channel - 180 degree shaped pulse for inversion (adiabatic)
;p11: f1 channel -  90 degree shaped pulse
;p16: homospoil/gradient pulse
;p21: f3 channel -  90 degree high power pulse
;p22: f3 channel - 180 degree high power pulse
;d0 : incremented delay (2D)                    [3 usec]
;d1 : relaxation delay; 1-5 * T1
;d11: delay for disk I/O                        [30 msec]
;d12: delay for power switching                 [20 usec]
;d16: delay for homospoil/gradient recovery
;d26 : 1/(4J)YH
;cnst4: = J(YH)
;inf1: 1/SW(X) = 2 * DW(X)
;in0: 1/(2 * SW(X)) = DW(X)
;nd0: 2
;ns: 4 * n
;ds: 16
;td1: number of experiments
;FnMODE: States-TPPI, TPPI, States or QSEQ
```

;cpd3: decoupling according to sequence defined by cpdprg3
;pcpd3: f3 channel - 90 degree pulse for decoupling sequence
;use gradient ratio: gp 3 : gp 4 : gp 5
; 50 : 80 : 30
;for z-only gradients:
;gpz3: 50%
;gpz4: 80%
;gpz5: 30%
;use gradient files:
;gpnam3: SMSQ10.100
;gpnam4: SMSQ10.100
;gpnam5: SMSQ10.100
;preprocessor-flags-start
;LABEL_CN: for C-13 and N-15 labeled samples start experiment with
; option -DLABEL_CN (eda: ZGOPTNS)
;preprocessor-flags-end
;$Id: hsqcfpf3gpphwg,v 1.12 2012/01/31 17:49:26 ber Exp $

^{15}N R1 rate measurements

Details:

Temperature: 15 °C
Spectral width: 12 ppm (direct dimension ^{1}H), 22 ppm (indirect dimension ^{15}N)
Complex points: 2048 (^{1}H), 256 (^{15}N)
Acquisition time: 0.142 sec
Relaxation time delay: 1.3 sec
Number of scans: 512

Pulse program: mb15nt1wtg_3d_4_10

; mb15nt1wtg_3d_4_10
; 633 1090 00 00 0210
; ----------
; 2D-15N-T1 with watergate as pseudo-3D

```
; T1 delays have to be n * 10m > 0m
; with IBURP option -Diburp n * 40
; with single-FID interleaving
; with temperature compensation
; F1 : number of 2D experiments
; F2 : 15N
;ds: use at least 4 dummy scans
;ns: !!!!! use 4*n scans only !!!!!
; -----------------
; Peter Schmieder
; Monika Beerbaum
; Martin Ballaschk, 10.10.2013
;_____________________________________
prosol relations=<triple>
#include <Avance.incl>
#include <Grad.incl>
#include <Delay.incl>
define list<delay> vd_list=<$VDLIST>
define delay vd_max
"in0 = inf2/2"
"p2 = 2.0*p1"
"p6 = 2.0*p5"
"d0 = 3u"
"d11 = 30m"
"d12 = 20u"
"d13 = 3u"
# ifdef iburp
 "d14 = 20m - p22/2 - d12"
 "d15 = d14 - 50u - p61 - d61"
# else
 "d14 = 0.5 * (5m - p2)"
 "d15 = d14 - 50u - p61 - d61"
# endif /*iburp*/
"TAU1 = 2.25m"
```

```
"TAU2 = TAU1 - p61 - d61 - 1.69*d3"
"TAU3 = (d3 - p6)/2"
"DELTA1 = 2.75m"
"DELTA2 = DELTA1 - p2 - 2.0*d0"
"l3 = td1"
"l14 = 1"
aqseq 312
1 ze
  "vd_max = 0"
3 d12
;---------- search for t1 max
  if "vd_list > vd_max"
     {
     d12
     "vd_max = vd_list"
     }
  3m vd_list.inc
  lo to 3 times l3
  3m vd_list.res
2 d11 do:f3
;---------- temp compensation for equal heating for each t1 point
# ifdef iburp
  "l2 = (vd_max - vd_list[t1loop])/40m"
4 d14
  d12
  (p22:sp22 ph2):f1
  d12
  d14
  lo to 4 times l2

# else
  "l2 = (vd_max - vd_list[t1loop])/10m"
  5 d14
  (p2 ph2):f1
```

```
  d14
  d14
  (p2 ph3):f1
  d14
  lo to 5 times l2
# endif /*iburp*/
; ---------- temperature compensation end
  d1
  d12 pl1:f1
  d12 pl3:f3
  p5:f3 ph1
  50u UNBLKGRAD
  p61:gp22
  d61
  p1 ph1
  TAU1
  (center (p2 ph1):f1 (p6 ph1):f3)
  TAU1
  p1 ph4
  d13
  d12 pl61:f1
  (p18:sp18 ph27:r):f1
  45u
  p61:gp22
  d61
  5u BLKGRAD
  d12 pl1:f1
  p5:f3 ph5
  DELTA1
  (center (p2 ph1):f1 (p6 ph1):f3)
  DELTA1
  p5:f3 ph6
  ;------------ start relaxation
# ifdef iburp
```

```
    "l14 = (vd_list[t1loop] - 40m)/40m"
  6 d14
    d12 pl61:f1
    (p22:sp22 ph1):f1
    d12
    d14 pl1:f1
    lo to 6 times l14
    d14
    d12 pl61:f1
    (p22:sp22 ph1):f1
    d12
    50u UNBLKGRAD
    p61:gp22
    d61
    d15
# else
 "l14 = (vd_list[t1loop] - 10m)/10m"
   d14
   (p2 ph2):f1
   d14
 7 d14
   (p2 ph3):f1
   d14
   d14
   (p2 ph2):f1
   d14
   lo to 7 times l14
   d14
   (p2 ph3):f1
   50u UNBLKGRAD
   p61:gp22
   d61
   d15
# endif /*iburp*/
```

```
;------------ end relaxation
  d12 pl1:f1
  p5:f3 ph7
  d0
  DELTA2
  (p2 ph8):f1
  d0
  p6:f3 ph9
  DELTA1
  p5:f3 ph10
  50u
  p61:gp23
  d61
  d12 pl61:f1
  (p18:sp18 ph28:r):f1
  d13
  d12 pl1:f1
  p1 ph1
  50u
  p61:gp21
  d61
  TAU2
  p1*0.231 ph2
  d3
  p1*0.692 ph2
  d3
  p1*1.4621 ph2
  TAU3
  p6:f3 ph1
  TAU3
  p1*1.4621 ph3
  d3
  p1*0.692 ph3
  d3
```

```
  p1*0.231 ph3
  45u
  p61:gp21
  d61
  5u BLKGRAD
  TAU2 pl16:f3
  go=2 ph31 cpd3:f3
  d11 do:f3 mc #0 to 2
        F1QF()
        F2PH(calph(ph7, +90), caldel(d0, +in0))
exit
ph1 = 0
ph2 = 1
ph3 = 3
ph4 = 1
ph5  = 0 2
ph6  = 1
ph7  = 1 1 3 3
ph8  = 0
ph9  = 0 0 0 0 1 1 1 1 2 2 2 2 3 3 3 3
ph10 = 0
ph27 = 2
ph28 = 0
ph31 = 0 2 2 0 2 0 0 2
; PARAMETER
;p1 :90deg  high power pulse f1 (pl1)
;p2 :180deg high power pulse f1 (pl1)
;p5 :90deg  high power pulse f3 (pl3)
;p6 :180deg high power pulse f3 (pl3)
;p18 :water flip back pulse f1 (sp18) [1msec]
;p22 :180deg off res. IBURP on HN f1 (sp22)
;p61 :gradient pulse   [1 msec]
;pcpd3 :90 deg 15N decoupling pulse at pl16
;pl1 :high power for protons f1
```

;pl3 :high power for 15N f3
;pl16 :power for 15N cpd-decoupling
;gpz21 :power for watergate gradient [30%]
;gpz22 :power for 1. crusher gradient [35%]
;gpz23 :power for 2. crusher gradient [40%]
;gpnam21 :shape for gradient p61 [SINE.100]
;gpnam22 :shape for gradient p61 [SINE.100]
;gpnam23 :shape for gradient p61 [SINE.100]
;d0 :incremented delay (15N)
;d1 :relaxation delay [1.3 sec]
;d3 :watergate delay (210u*600MHz/SpectFreq)
;d11 :delay for disk I/O [30 msec]
;d12 :delay for power switching [20 usec]
;d13 :short delay [3 usec]
;d61 :gradient recovery delay [500 usec]
;TAU1 :1/(4J) XH
;DELTA1 :1/(4J) XH
;cpdprg3 :decoupling sequence in f3 [waltz16]
;in0:increment for 15N
;l14 :T1 loop
;vd :choose delay list from /exp/stan/nmr/lists/vd/
;__________parameters for shaped pulses__________
;sp24 :power for Bip pulse p24
;spnam24 :shape for p24 [Bip720,50,20.1]
;spoffs24 :offset for p24 [0]
;sp22 :power for sel. pulse p22
;spnam22 :shape for sel. pulse p22 [Iburp2.1000]
;spoffs22 :offset for sel. pulse p22 (o2p to HN)
;__________options__________

;zgoptns :-Diburp for selective IBURP2 pulses instead of hard ones

^{15}N R2 rate measurements

Details:

Temperature: 15 °C

Spectral width: 12 ppm (direct dimension ^{1}H), 22 ppm (indirect dimension ^{15}N)

Complex points: 2048 (^{1}H), 256 (^{15}N)

Acquisition time: 0.142 sec

Relaxation time delay: 1.3 sec

Number of scans: 512

Pulse program: mb15nt2wtg_3d_3

```
; mb15nt2wtg_3d_3
; -----------------
; 2D-15N-T2 with watergate as pseudo-3D
; T2 delays have to be multiples of 8m
; with single-FID interleaving
; with temperature compensation
; with option for BIP pulses on protons -Dbip
; F1 : number of 2D experiments
; F2 : 15N
;ds: use at least 4 dummy scans
;ns: !!!!! use 4*n scans only !!!!!
; -----------------
; Peter Schmieder
; Monika Beerbaum
; Martin Ballaschk, 14.08.2013
; Editada por AB para que funcione en el 600 de Rosario
;_____________________________________
prosol relations=<triple>
#include <Avance.incl>
#include <Grad.incl>
#include <Delay.incl>
prosol relations=<fmp_2011_basic>
define list<delay> vd_list=<$VDLIST>
```

```
define delay vd_max
"in0 = inf2/2"
"p6 = 2.0*p5"
"d0 = 3u"
"d1 = 1.3s"
"d11 = 30m"
"d12 = 20u"
"d13 = 3u"
"DELTA1 = 2.75m"
"d15 = 1m - p6"
"d14 = 0.5*d15"
#  ifdef bip
"d16 = (d15 - p24)/2"
"DELTA2 = DELTA1 - p24 - 2.0*d0"
#  else
"p2 = 2.0*p1"
"d16 = (d15 - p2)/2"
"DELTA2 = DELTA1 - p2 - 2.0*d0"
#  endif /*bip*/
"TAU1 = 2.25m"
"TAU2 = TAU1 - p61 - d61 - 1.69*d3"
"TAU3 = (d3 - p6)/2"
"l3 = td1"
"l14 = 1"
aqseq 312
1 ze
  "vd_max = 0"
3 d12
;--------------------------- search for t1 max
  if "vd_list > vd_max"
     {
     20u
     "vd_max = vd_list"
     }
```

```
  3m vd_list.inc
  lo to 3 times l3
  3m vd_list.res
2 d11 do:f3
;--------------------------- temp compensation for equal heating time for each t1 point
  "l2 = (vd_max - vd_list[t1loop]) / 8m"
4 d14
  (p6 ph1):f3
  d15
  (p6 ph1):f3
#  ifdef bip
  (d15) (d16 p24:sp24 ph2)
#  else
  (d15) (d16 p2 ph2)
#  endif /*bip*/
  (p6 ph1):f3
  d15
  (p6 ph1):f3
  d15
  (p6 ph1):f3
  d15
  (p6 ph1):f3
#  ifdef bip
  (d15) (d16 p24:sp24 ph3)
#  else
  (d15) (d16 p2 ph3)
#  endif /*bip*/
  (p6 ph1):f3
  d15
  (p6 ph1):f3
  d14
  lo to 4 times l2
;------------ end of temperature compensation
  d1
```

```
  d12 pl3:f3
  p5:f3 ph1
  50u UNBLKGRAD
  p61:gp22
  d61
;--------------------------- first INEPT
  p1 ph1
  TAU1
#  ifdef bip
  (center (p24:sp24 ph1):f1 (p6 ph1):f3)
#  else
  (center (p2 ph1):f1 (p6 ph1):f3)
#  endif /*bip*/
  TAU1 pl1:f1
  p1 ph4
  d13
  d12 pl61:f1
  (p18:sp18 ph27:r):f1
;--------------------------- end of first INEPT
  45u
  p61:gp22
  d61
  5u BLKGRAD
  d12 pl1:f1
  p5:f3 ph5
  DELTA1
#  ifdef bip
  (center (p24:sp24 ph1):f1 (p6 ph1):f3)
#  else
  (center (p2 ph1):f1 (p6 ph1):f3)
#  endif /*bip*/
  DELTA1
;------------ start relaxation loop
  "l14 = vd_list[t1loop] / 8m"
```

```
5 d14
  (p6 ph1):f3
  d15
  (p6 ph1):f3
#  ifdef bip
  (d15) (d16 p24:sp24 ph2)
#  else
  (d15) (d16 p2 ph2)
#  endif /*bip*/
  (p6 ph1):f3
  d15
  (p6 ph1):f3
  d15
  (p6 ph1):f3
  d15
  (p6 ph1):f3
#  ifdef bip
  (d15) (d16 p24:sp24 ph3)
#  else
  (d15) (d16 p2 ph3)
#  endif /*bip*/
  (p6 ph1):f3
  d15
  (p6 ph1):f3
  d14
  lo to 5 times l14
;------------ end relaxation loop
  p5:f3 ph6
  50u UNBLKGRAD
  p61:gp22
  d61
;---------------------------
  p5:f3 ph7
  d0
```

```
  DELTA2
#  ifdef bip
  (p24:sp24 ph8):f1
#  else
  p2 ph8
#  endif /*bip*/
  d0
  p6:f3 ph9
  DELTA1
  p5:f3 ph10
  p61:gp23
  d61
  d12 pl61:f1
  (p18:sp18 ph28:r):f1
  d13
  d12 pl1:f1
  p1 ph1
  50u
  p61:gp21
  d61
  TAU2
  p1*0.231 ph2
  d3
  p1*0.692 ph2
  d3
  p1*1.4621 ph2
  TAU3
  p6:f3 ph1
  TAU3
  p1*1.4621 ph3
  d3
  p1*0.692 ph3
  d3
  p1*0.231 ph3
```

```
  45u
  p61:gp21
  d61
  5u BLKGRAD
  TAU2 pl16:f3
  go=2 ph31 cpd3:f3
  d11 do:f3 mc #0 to 2
        F1QF()
        F2PH(calph(ph7, +90), caldel(d0, +in0))
exit
ph1 = 0
ph2 = 1
ph3 = 3
ph4 = 1
ph5 = 0 2
ph6 = 1
ph7 = 1 1 3 3
ph8 = 0
ph9 = 0 0 0 0 1 1 1 1 2 2 2 2 3 3 3 3
ph10 = 0
ph27 = 2
ph28 = 0
ph31 = 0 2 2 0 2 0 0 2
; PARAMETER
;__________Pulses__________
;p1 :90deg high power pulse f1 (pl1)
;p2 :180deg high power pulse f1 (pl1)
;p5 :90deg high power pulse f3 (pl3)
;p6 :180deg high power pulse f3 (pl3)
;p61 :gradient pulse   [1 msec]
;_________power level for hard pulses_________
;pl1 :high power for protons f1
;pl3 :high power for 15N f3
;__________parameters for shaped pulses_________
```

;sp24 :power for Bip pulse p24
;spnam24 :shape for p24 [Bip720,50,20.1]
;spoffs24 :offset for p24 [0]
;__________Gradients_________
;gpz21 :power for watergate gradient [30%]
;gpz22 :power for 1. crusher gradient [35%]
;gpz23 :power for 2. crusher gradient [40%]
;gpnam21 :shape for gradient p61 [SINE.100]
;gpnam22 :shape for gradient p61 [SINE.100]
;gpnam23 :shape for gradient p61 [SINE.100]
;__________decoupling__________
;pcpd3 :90 deg 15N decoupling pulse (pl16)
;cpdprg3 :decoupling sequence in f3 [waltz16]
;pl16 :power for 15N cpd-decoupling
;_________delays__________
;d0 :incremented delay (15N)
;d1 :relaxation delay [1.3 sec]
;d3 :watergate delay (210u*600MHz/SpectFreq)
;d11 :delay for disk I/O [30 msec]
;d12 :delay for power switching [20 usec]
;d13 :short delay [3 usec]
;d61 :gradient recovery delay [500 usec]
;TAU1 :1/(4J) XH
;DELTA1 :1/(4J) XH
;__________constants__________
;vd :choose delay list from /exp/stan/nmr/lists/vd/
;l14 :T2 loop
;l14 determines the length of the T2 delay. One loop corresponds
;to 8msec + 8*p6.
;__________increments__________
;in0:increment for 15N
;__________options__________
;zgoptns :-Dbip for bip pulses instead of hard ones

$^{3}J_{HN\text{-}H\alpha}$ coupling constant

Details:

Temperature: 15 °C

Spectral width: 8 ppm (direct dimension ^{1}H), 22 ppm (indirect dimension ^{15}N)

Complex points: 4096 (^{1}H), 512 (^{15}N)

Acquisition time: 0.427 sec

Relaxation time delay: 1 sec

Number of scans: 1024

Pulse program: trosyetf3gpsi

```
;trosyetf3gpsi
;avance-version (12/01/11)
;2D H-1/X correlation via TROSY
;   using sensitivity improvement
;phase sensitive using Echo/Antiecho gradient selection
;using f3 - channel
;(use parameterset TROSYETF3GPSI)
;M. Czisch & R. Boelens, J. Magn. Reson. 134, 158-160 (1998)
;K. Pervushin, G. Wider & K. Wuethrich, J. Biomol. NMR 12,
;   345-348 (1998)
;A. Meissner, T. Schulte-Herbrueggen, J. Briand & O.W. Sorensen, Mol. Phys. 96,
;   1137-1142 (1998)
;J. Weigelt, J. Am. Chem. Soc. 120, 10778-10779 (1998)
;M. Rance, J.P. Loria & A.G. Palmer III, J. Magn. Reson. 136, 91-101 (1999)
;G. Zhu, X.M. Kong & K.H. Sze, J. Biomol. NMR 13, 77-81 (1999)
;$CLASS=HighRes
;$DIM=2D
;$TYPE=
;$SUBTYPE=
;$COMMENT=
#include <Avance.incl>
#include <Grad.incl>
#include <Delay.incl>
```

```
"p2=p1*2"
"p22=p21*2"
"d11=30m"
"d26=1s/(cnst4*4)"
"d0=6u"
"in0=inf1/2"
"DELTA1=d26-p16-d16-4u"
"DELTA2=d26-p1-p16-d16-4u"
"DELTA3=p19+d16+8u"
#   ifdef LABEL_CN
"DELTA=d0*2+p14+p21*4/3.1416+8u"
#   else
"DELTA=d0*2+p21*4/3.1416+6u"
#   endif /*LABEL_CN*/
"l0=1"
1 ze
2 d11
3 d1 pl1:f1
  50u UNBLKGRAD
  (p1 ph1)
  4u
  p16:gp1
  d16
  DELTA1
  (center (p2 ph2) (p22 ph1):f3 )
  4u
  DELTA1
  p16:gp1
  d16
  (p1 ph3)
  if "l0 %2 == 1"
    {
    (p21 ph4):f3
    }
```

```
  else
    {
    (p21 ph5):f3
    }
#   ifdef LABEL_CN
  d0 gron0
  2u groff
  (p14:sp3 ph1):f2
  d0 gron0*-1
  2u groff
#   else
  d0 gron0
  d0 gron0*-1
  2u groff
#   endif /*LABEL_CN*/
  4u
  p19:gp2*EA
  d16
  (p22 ph1):f3
  DELTA
  p19:gp2*-1*EA
  d16
  (p1 ph6)
  4u
  p16:gp3
  d16
  DELTA2 pl1:f1
  (center (p2 ph1) (p22 ph1):f3 )
  4u
  DELTA1
  p16:gp3
  d16
  (center (p1 ph1) (p21 ph2):f3
  4u
```

```
 p16:gp4
 d16
 DELTA1
 (center (p2 ph1) (p22 ph1):f3 )
 DELTA1
 p16:gp4
 d16
 4u
 (p21 ph7):f3
 DELTA3
 (p2 ph1)
 4u
 p19:gp5
 d16
 4u BLKGRAD
 go=2 ph31
 d11 mc #0 to 2
   F1EA(calgrad(EA) & calph(ph6, +180) & calph(ph7, +180) & calclc(l0, 1), caldel(d0, +in0) & calph(ph4, +180) & calph(ph5, +180) & calph(ph31, +180))
exit
ph1=0
ph2=1
ph3=3
ph4=1 3 2 0
ph5=3 1 2 0
ph6=1
ph7=0
ph31=0 2 3 1
;pl1 : f1 channel - power level for pulse (default)
;pl3 : f3 channel - power level for pulse (default)
;sp3: f2 channel - shaped pulse 180 degree (adiabatic)
;p1 : f1 channel -  90 degree high power pulse
;p2 : f1 channel - 180 degree high power pulse
;p14: f2 channel - 180 degree shaped pulse for inversion (adiabatic)
```

```
;p16: homospoil/gradient pulse                    [1 msec]
;p19: gradient pulse 2                          [500 usec]
;p21: f3 channel -  90 degree high power pulse
;p22: f3 channel - 180 degree high power pulse
;d0 : incremented delay (2D)                     [6 usec]
;d1 : relaxation delay; 1-5 * T1
;d11: delay for disk I/O                        [30 msec]
;d16: delay for homospoil/gradient recovery
;d26 : 1/(4J)YH
;cnst4: = J(YH)
;inf1: 1/SW(X) = 2 * DW(X)
;in0: 1/(2 * SW(X)) = DW(X)
;nd0: 2
;ns: 4 * n
;ds: 16
;td1: number of experiments
;FnMODE: echo-antiecho
;use gradient ratio:    gp 0 : gp 1 : gp 2 : gp 3 : gp 4 : gp 5
;                        3 :   30 :   80 :   45 :   50 : 16.2
;for z-only gradients:
;gpz0: 3%
;gpz1: 30%
;gpz2: 80%
;gpz3: 45%
;gpz4: 50%
;gpz5: 16.2%
;use gradient files:
;gpnam1: SMSQ10.100
;gpnam2: SMSQ10.50
;gpnam3: SMSQ10.100
;gpnam4: SMSQ10.100
;gpnam5: SMSQ10.50
                                ;preprocessor-flags-start
;LABEL_CN: for C-13 and N-15 labeled samples start experiment with
```

; option -DLABEL_CN (eda: ZGOPTNS)
;preprocessor-flags-end
;$Id: trosyetf3gpsi,v 1.10 2012/01/31 17:49:31 ber Exp $

Hydrodynamic radius

Details:

Temperature: 15 °C
Spectral width: 12 ppm
Complex points: 8192
Acquisition time: 0.562 sec
Relaxation time delay: 3 sec
Number of scans: 512

Pulse program: ledbpgppr2s

```
;ledbpgppr2s
;avance-version (12/01/11)
;2D sequence for diffusion measurement using stimulated
;   echo and LED
;using bipolar gradient pulses for diffusion
;using 2 spoil gradients
;with presaturation during relaxation delay
;D. Wu, A. Chen & C.S. Johnson Jr.,
;   J. Magn. Reson. A 115, 260-264 (1995).
;$CLASS=HighRes
;$DIM=2D
;$TYPE=
;$SUBTYPE=
;$COMMENT=
#include <Avance.incl>
#include <Grad.incl>
#include <Delay.incl>
define list<gradient> diff=<Difframp>
```

```
"p2=p1*2"
"d11=30m"
"d12=20u"
"DELTA1=d20-p1*2-p2-p30*2-d16*2-p19-d16-d12-4u"
"DELTA2=d21-p19-d16-d12-8u"
"acqt0=-p1*2/3.1416"
1 ze
2 d11
3 d12 pl9:f1
  d1 cw:f1 ph29
  50u do:f1 UNBLKGRAD
  d12 pl1:f1
  p1 ph1
  p30:gp6*diff
  d16
  p2 ph1
  p30:gp6*-1*diff
  d16
  p1 ph2
  p19:gp7
  d16 pl9:f1
  DELTA1 cw:f1 ph29
  4u do:f1
  d12 pl1:f1
  p1 ph3
  p30:gp6*diff
  d16
  p2 ph1
  p30:gp6*-1*diff
  d16
  p1 ph4
  p19:gp8
  d16 pl9:f1
  DELTA2 cw:f1 ph29
```

```
  4u do:f1
  d12 pl1:f1
  4u BLKGRAD
  p1 ph5
  go=2 ph31
  d11 mc #0 to 2 F1QF(calgrad(diff))
exit
ph1= 0
ph2= 0 0 2 2
ph3= 0 0 0 0 2 2 2 2  1 1 1 1 3 3 3 3
ph4= 0 2 0 2 2 0 2 0  1 3 1 3 3 1 3 1
ph5= 0 0 0 0 2 2 2 2  1 1 1 1 3 3 3 3
ph29=0
ph31=0 2 2 0 2 0 0 2  3 1 1 3 1 3 3 1
;pl1 : f1 channel - power level for pulse (default)
;pl9 : f1 channel - power level for presaturation
;p1  : f1 channel -  90 degree high power pulse
;p2  : f1 channel - 180 degree high power pulse
;p19: gradient pulse 2 (spoil gradient)
;p30: gradient pulse (little DELTA * 0.5)
;d1  : relaxation delay; 1-5 * T1
;d11: delay for disk I/O                  [30 msec]
;d12: delay for power switching                [20 usec]
;d16: delay for gradient recovery
;d20: diffusion time (big DELTA)
;d21: eddy current delay (Te)                 [5 ms]
;ns: 8 * n
;ds: 4 * m
;td1: number of experiments
;FnMODE: QF
;       use xf2 and DOSY processing
;use gradient ratio:    gp 6 : gp 7   : gp 8
;                     100  : -17.13 : -13.17
;for z-only gradients:
```

;gpz6: 100%
;gpz7: -17.13% (spoil)
;gpz8: -13.17% (spoil)
;use gradient files:
;gpnam6: SMSQ10.100
;gpnam7: SMSQ10.100
;gpnam8: SMSQ10.100
;use AU-program dosy to calculate gradient ramp-file Difframp
;$Id: ledbpgppr2s,v 1.4 2012/01/31 17:49:27 ber Exp $

7.3 Delay Times of Relaxation Rate Measurements

Table 21: List of delay times in ^{15}N NMR relaxation rate measurements R_1 and R_2.

R_1 delay times [sec]		R_2 delay times [sec]	
0.050	1.600	0.184	0.264
1.100	0.800	0.064	0.360
0.150	0.400	0.480	0.064
0.600	1.100	0.024	0.264
0.800	0.150	0.640	0.570
0.250	1.300	0.120	0.800

Acknowledgments

I would like to thank my first supervisor, Prof. Dr Christian Griesinger for his supervision and guidance throughout this project and the possibility to join the binational doctoral program. In this context, I also thank my second supervisor, Prof. Dr. Claudio Fernández, who ensured that I had an extraordinary research experience during my stay in Argentina, which I enjoyed very much. Next, I thank my thesis committee member Prof. Dr. Nils Brose, for his cooperation and helpful comments during the meetings. Thanks as well to the further members of my Examination Board, Prof. Dr. Kai Tittmann, Prof. Dr. Eduardo Ceccarelli and Prof. Dr. Nicolás Rey, for taking the time to evaluate my work.

Next, I thank Prof. Dr. Stefan Eimer. Thank you for adopting me much longer than intended during the Corona pandemic, supporting, advising, and teaching me the experimental field of *C. elegans*, as well as providing me with the equipment I needed to conduct my studies. Following, my thanks to Prof. Dr. Tiago Outeiro, where I conducted the experiments of cellular inclusions in H4 cells.

I would like to thank as well Prof. Dr. Christian Griesinger and Prof. Dr. Claudio Fernández and all the people on both hemispheres involved for establishing and organizing the international German-Argentinian PhD cooperation project.

For the German side, my further thanks go to the research group of Prof. Dr. Christian Griesinger, for their support and cooperation. Special thanks here to Petra and Dirk for the administrative help! Also, many thanks to my colleagues in Frankfurt at Prof. Dr. Stefan Eimer’s research group, Barbara, Sebastian, Julius, Regine, and Ludo. Thanks for welcoming me, for many lovely moments and all the help I received from you throughout my long stay.

On the Argentinian side of my PhD project, I would like to thank the entire working group of Prof. Dr. Claudio Fernández, especially Laura and Amalia for all the administrative help and kindness I received. Furthermore, my big thanks to my (ex-) colleagues and friends, for receiving me with open arms and hearts, supporting me professionally as much as personally and making my time in Rosario a wonderful experience: Fran, Mila y Arturo, Jesi, Esteban, Gisel, Pheli, Thainah, Laura y Teresa, gracias por sus amistades, ya nos vemos pronto!

Without the help and support of Leo, Annette and Joaquin, this PhD work would not have been possible: From the bottom of my heart many thanks for your support no matter the distance, in any imaginable way and in every situation. Also, I huge thank you to the rest of my family (special thanks to Yani for always entertaining me!) and my friends for supporting and always believing in me, for the joy and happiness you bring to my life. Thanks for the many shared smiles and laughs, which were always helping me throughout my PhD time.